

OPTICAL GEOMETRY CALIBRATION METHOD FOR COMPUTED TOMOGRAPHY
AND APPLICATIONS OF COMPACT MICROBEAM RADIATION THERAPY

Pavel Chtcheprov

A dissertation submitted to the faculty of the University of North Carolina at Chapel Hill
and North Carolina State University in partial fulfillment of the requirements for the
degree of Doctor of Philosophy in the joint Department of Biomedical Engineering.

Chapel Hill
2016

Approved by:

David Lalush

Otto Zhou

Jianping Lu

Yueh Lee

Hugon Karwowski

© 2016
Pavel Chtcheprov
ALL RIGHTS RESERVED

ABSTRACT

Pavel Chtcheprov: Optical Geometry Calibration Method for Free Form Digital Tomosynthesis
(Under the direction of Jianping Lu and Otto Zhou)

Digital tomosynthesis is a type of limited angle tomography that allows for 3D information reconstructed from a set of X-ray projection images taken at various angles using an X-ray tube, a mechanical arm to rotate the tube, and a digital detector. Tomosynthesis reconstruction requires the knowledge of the precise location of the detector with respect to each X-ray source.

Current clinical tomosynthesis methods use a physically coupled source and detector so the geometry is always known and is always the same. This makes it impractical for mobile or field operations. We demonstrated a free form tomosynthesis and free form computed tomography (CT) with a decoupled source and detector setup that uses a novel optical method for accurate and real-time geometry calibration.

We accomplish this by using a camera to track the motion of the source relative to the detector, which is necessary for 3D reconstruction. A checkerboard pattern is positioned on or next to the detector using an extension arm in such a way that the pattern will not move relative to the detector. A camera is mounted on the source in a way that the pattern is visible during imaging and will not move relative to the source. The image of the pattern captured by the camera is then used to determine the relative camera/pattern position and orientation by analyzing the pattern distortion. This allows for accurate, real time geometry calibration of the X-ray source relative to the detector. This method opens

the doors for inexpensive upgrades to existing 2D imaging systems and an even more exciting application of a mobile, hand-held CT imaging system to be used in a variety of medical and military applications.

ACKNOWLEDGEMENTS

I would like to express my sincere gratitude to my advisors, Dr. Jianping Lu and Dr. Otto Zhou, for their support and motivation on all of my projects. Their insight and drive for innovation inspired and pushed me to new intellectual limits. I would like to thank Dr. Yueh Lee for introducing me to the Applied Nanotechnology Lab and for the vast clinical research applications that he brought forth, including the animal protocols for our experiments. I would like to thank Dr. David Lalush for his imaging expertise and his experience in CT reconstruction algorithms, without which this research would have no practical applications. And I would like to thank Dr. Hugon Karwowski, for not only being a great electronics teacher, but also a steadfast mentor who has pushed me to think of myself and my future in new ways.

I would also like to thank all of my lab mates who provided professional and emotional support over the past five years — Dental Team: Gongting Wu, Dr. Jing Shan, Dr. Enrique Platin, Allison Hartman, and Jabari Calliste. Apollo II Team: Dr. Sha Chang, Christy Inscoe, Lei Zhang, Dr. Mike Hadsell, and Phil Laganis. Gated MRT Team: Christy Inscoe, Lei Zhang, Dr. Laurel Burk, and Dr. Yueh Lee. FIGMRT Team: Christy Inscoe, Lei Zhang, Dr. Laurel Burk, and Dr. Hong Yuan, and Dr. Yueh Lee. I would also like to thank the Physics Instrument Shop for their continued expertise with construction and manufacturing projects, and a special thanks to Christy for her critical role in almost every project as well as her guidance as a scientist and engineer.

Also, I would like to thank my wife, Kelly, for her continued support during my time as a graduate student and her design efforts in making my work look visually appealing and not just scientifically correct – something I often overlook. I would like to thank her for proofreading my manuscripts and telling me when my descriptions assume the reader is as immersed in the project as I am. I would also like to thank my parents for pushing me to this moment, especially my dad who has been a constant source of inspiration from the time I was in my crib, watching him derive equations on his stacks and stack of notebooks.

The fluorescence MRT work was supported by the National Cancer Institute (NCI) funded Carolina Center for Cancer Nanotechnology Excellence (U54-CA151652). The gated MRT work was supported by the National Cancer Institute (NCI) funded Carolina Center for Cancer Nanotechnology Excellence (U54CA119343). I would also like to thank Jon Frank from UNC BRIC for his help with animal handling.

TABLE OF CONTENTS

ABSTRACT	iii
ACKNOWLEDGEMENTS	v
TABLE OF CONTENTS.....	vii
LIST OF FIGURES	xi
LIST OF ABBREVIATIONS	xvii
Chapter 1: Introduction.....	1
1.1 Tomosynthesis	1
1.2 Computed Tomography	4
Chapter 2: Geometry calibration method based on pattern recognition.....	7
2.1 Current Clinical Geometry Calibration Methods	7
2.2 Pattern Detection.....	8
2.3 Optical Geometry Calibration Method.....	9
2.4 Stationary Detector	11
2.5 Moving Detector.....	13
Chapter 3: Free Form Tomosynthesis.....	24
3.1 Motivation	24
3.2 Application	25
3.3 Accuracy	28

3.4 Blank Image Library	33
3.5 Reconstruction	34
3.6 Matlab Implementation.....	35
CHAPTER 4: Intraoral Tomosynthesis.....	41
4.1 Motivation	41
4.2 Application	42
4.4 Future Development	45
Chapter 5: Free Form Computed Tomography.....	46
5.1 Motivation	46
5.2 Imaging	46
5.3 Matlab Implementation.....	49
5.4 Experimental Validation	53
Chapter 6: Conclusion and Discussion.....	58
Appendix 1: Introduction To Microbeam Radiation Therapy.....	61
1.1 Glioblastoma Multiforme.....	61
1.2 Radiation Therapy	63
1.3 Treatment Planning	67
Appendix 2: Background on Field Emission	70
2.1 Carbon Nanotube Field Emission	70
2.2 Carbon Nanotube Field Emission X-ray Tubes	72
2.3 Microbeam Radiation Therapy	75

2.4 Compact Image Guided MRT System for Small Animal Treatment.....	78
2.5 Desktop MRT System	79
2.6 Fluorescence Imaging	80
2.6.1 Abstract	80
2.6.2 Motivation	81
2.6.3 X-ray Fluorescence.....	83
2.6.4 Methods	84
2.6.5 Results.....	87
2.6.5 Conclusions	91
2.6.6 Discussion	92
2.7 Physiologically Gated Microbeam Radiation	97
2.7.1 Abstract	97
2.7.2 Motivation	98
2.7.3 Physiological Motion Monitoring.....	99
2.7.4 Mechanical phantom.....	100
2.7.5 Mouse Model and Handling.....	101
2.7.6 Respiratory Gated Irradiation.....	101
2.7.7 Irradiation Protocols	103
2.7.8 Histology	104
2.7.9 Results.....	105
2.7.10 Conclusions	110

2.8 Microbeam Interaction Simulations.....	111
Appendix 3: Second Generation Desktop MRT (Apollo II)	115
3.1 Motivation	115
3.2 Specifications	115
3.3 Design	116
3.3.1 Tube.....	116
3.3.2 Anode.....	118
3.3.3 Cathode Assembly.....	119
3.3.4 Collimator	119
3.3.5 Enclosure.....	121
3.4 Current Status.....	124
REFERENCES	125

LIST OF FIGURES

Figure 1. Two FDA approved digital breast tomosynthesis systems: GE SenoClaire and Hologic Selenia Dimensions.....	1
Figure 2. Hologic Selenia Dimensions tomosynthesis system showing the rotating gantry holding the source.	2
Figure 3. Image sets taken from our lab’s custom-made stationary source array tomosynthesis systems. Left: Comparison of 2D mammo to a 3D tomo of breast tissue and the increase visiblity of a lesion inside the tissue. Right: A) photo of tooth phantom B) 2D radioagraph of phantom C-F) Slices of a tomo set showing various carries that are not noticeable in B. Note the three roots in C and D that are hidden in B.....	3
Figure 4. GE CT machine from http://www3.gehealthcare.in/en/products/categories/computed-tomography	4
Figure 5. Shepp–Logan phantom (left) and its sinogram (right). Adapted from https://tomroelandts.com/articles/tomography-part-3-reconstruction	5
Figure 6. Bead phantom method of geometry calibration.	7
Figure 7. Camera calibration images using a checkerboard pattern in different orientation.	8
Figure 8. Processed checkerboard pattern image with the black square intersections highlighted along with the coordinate system axes.....	9
Figure 9. Setup modeled in Solidworks showing the camera and source attachment with the pattern and detector assembly.....	10
Figure 10. Camera/source motion about an object and camera views of the pattern at each position	10
Figure 11. Source, Camera, Detector, and Pattern setup.	11
Figure 12. Two views of source to camera vector lines plotted in CC with the average vector in red.....	13
Figure 13. Sample large angle tomo setup diagram.....	14
Figure 14. Camera centric and pattern centric views of three images taken at each detector position.	15
Figure 15. Large angle tomosynthesis diagram.	16
Figure 16. Rotation matrix between detectors illustration	18

Figure 17. Error propagation simulation showing the absolute position error (in mm) accumulating with each position change.	23
Figure 18. Portable, handheld X-ray security imaging devices by NOVO Digital Radiography http://www.novo-dr.com/	25
Figure 19. Flow chart of free form imaging process.	26
Figure 20. Setup using the Carestream DRX Revolution mobile imaging unit. Left: Camera mounting bracket and safety tape holding loose USB Right: Detector with optical pattern placement and beads (attached post imaging to relate pattern to detector).	28
Figure 21. Percent of the field of view taken by the pattern board vs accuracy.	29
Figure 22. Two camera accuracy in the X-Y plane.	30
Figure 23. Speed graph during horizontal motion tracking on a 2.5mm/s translation stage showing the average calculated speed.	30
Figure 24. 3D representation of the camera and source positions (numbered dots) relative to the detector. The source and camera were positioned by hand about the detector and are not meant to follow a perfect arc.	31
Figure 25. Slices 7, 20, and 63 using the geometry phantom source position data (top) compared to the optically calculated source positions (bottom) showing the wire and different beads in focus.	32
Figure 26. Horizontal and vertical profiles of the optically reconstructed bar in the phantom images 635 μm	32
Figure 27. Five slices through a foot from free tomo acquisition (source was manually moved to 11 positions across an $\sim 15^\circ$ arc)	34
Figure 28. Sets of 3 images from 2 depths of reconstruction tomo sets of a hand. First image in each set was taken by the stationary chest tomo, second was on the free tomo setup using the geometry phantom to calculate the source position and the third was using the optical calibration geometry.	34
Figure 29. Webcam acquisition GUI.	38
Figure 30. Screenshot of the Camera Calibrator App in Matlab loaded with an image set.	39
Figure 31. Output of the showExtrinsicsDATA_SET_NAME_CALIB.m file. The “error” from the predicted value to the “actual” value of the geocal phantom, the calibration pixel error, the vectors averages to show the CS vector, and the camera and source positions plotted relative to the optical pattern.	39

Figure 32. Oral tomosynthesis setup using a custom made holder with the checkerboard pattern and with the optical camera attached on the X-ray housing.	43
Figure 33. Illustration of bead phantom calibration problem with a small detector relative to the source to detector distance. The detector pixel size of 33 μ m creates an uncertainty shown on the left that results in a much larger 1.6mm source uncertainty shown on the right.	44
Figure 34. Camera attached to dental X-ray unit and imaging a dental phantom with the custom made detector and pattern holder.	44
Figure 35. Flowchart showing the imaging cycle of the free form tomo imaging.	47
Figure 36. A) Free form CT imaging setup with the object rigidly attached to not move during the process to a low attenuating rod (meter stick). B) Imaging begins at the left side. C) Reaching the limit of this detector position. D) Source is stationary, the detector is moved to preserve the coordinate system. E) Imaging continues to the right-most side with the detector flat. F) Source is stationary, the detector is moved once again and the imaging can continue to the right side.	48
Figure 37. Reconstructed patterns and camera coordinate systems of a desktop proof of concept to show the program working. The rainbow colored rectangle is the starting pattern position.	53
Figure 38. Reconstructed camera and source positions on a CT data set. The dark blue lines are the z-axes of the camera (pointing directly out perpendicular to the lens) and the asterisks are the calculated source positions.	54
Figure 39. Side and top projection views of the security phantom.	55
Figure 40. Top: Projection image of the circuit board showing no depth information regarding the serial pins on the left. Bottom: Photo of the serial pins.	56
Figure 41. Slices 3 and 17 (at 0.2mm slice thickness) focusing on the top and bottom pins of the serial connection. The slice separation is 2.8mm (at the 0.2mm resolution) indicating the same separation between the top and bottom rows. The datasheet on the right shows the actual distance to be 2.84mm.	56
Figure 42. Line profile of the chip pins showing the expected increase in contrast in the tomo slice due to the removal of attenuating layers above and below in the projection image.	57

Figure 43. X-ray Scanning Robot from the First Responders Group in DC. http://www.firstresponder.gov/TechnologyImages/X-Ray%20Scanning%20Rover/x%20ray%20rover.jpg	60
Figure 44. Schematic of a CNT field emission X-ray source.	74
Figure 45 Spacial distribution of X-rays around a thin target. F. Khan, "Total body irradiation," The physics of radiation therapy.3rd ed.Philadelphia: Lippincott Williams & Wilkins, 455-463 (2003).....	75
Figure 46. MRT beam visualization using a crosshatched irradiation pattern.....	76
Figure 47. a) Isolated view of the cathode assembly showing the 5 cathodes producing a focal line on the anode. b) Side cutaway view of the MRT tube showing the electron beam from the cathodes hitting the anode and producing the fan beam which is then collimated	80
Figure 48. X-ray fluorescence illustration	83
Figure 49. X-ray fluorescence setup with the Amptek spectrum analyzer, the slit collimator, MRT beam positioned directly through the collimator slit, and the sample.	85
Figure 50. Illustration of the MRT XRF imaging system. The subject is slowly scanned through the MRT beam and the fluorescent signal from the iodine in that slice is recorded and processed. The output is an iodine concentration vs position graph corresponding to the tumor location.	87
Figure 51. Iodine fluorescence spectrum showing the k alpha peak at 28.6 keV	88
Figure 52. Fluorescent signal vs position of 0.2 mm/step, 20 s/step cylindrical phantom.....	89
Figure 53. Mouse in holder with Gafchromic X-ray sensitive film showing the starting radiation beam location	89
Figure 54. Fluorescent signal vs position graph overlaid on a sagittal projection X-ray. 1 minute perfusion; 1 mm/step, 20 s/step, 80mm total scan distance	90
Figure 55. Fluorescent signal vs position graph overlaid on a CT sagittal projection with color marked organs. 10 minute perfusion; 1mm/step, 20 s/step, 90 mm total scan distance.....	91
Figure 56. Schematic of phantom using servo motor arm simulating mouse abdominal motion during breathing. The arm is always in contact with the foam pad and the pressure sensor and oscillates in the direction shown.	100

Figure 57. BioVet© differential pressure measurement, correlated to chest displacement, compared to the phantom angular displacement.	101
Figure 58. X-ray exposure pulse diagram. The top is the BioVet© output of the respiratory motion from the pressure sensor attached to the mouse. The green line is the threshold set by the operator at low as possible but still having the ‘motionless’ state below it. The second pulse sequence shows the delay pulses that start the irradiation on a high-to-low trigger. The last sequence shows the cathode pulses that generate the X-rays. The cathodes are negatively pulsed at 500 μ s pulse widths with an 8% duty cycle.....	103
Figure 59. Diagram of histology section plane	104
Figure 60. Single beam dose curves for three 5 minute irradiations at 160 kVp.....	106
Figure 61. Three beam dose curves for three 5 minute/line irradiations at 160 kVp.....	107
Figure 62. Mouse in the mouse bed post-treatment with MRT beam lines shown on EBT2 Gafchromic© dosimetry film taped to bed.	108
Figure 63. γ -H2Ax staining of a liver cross section showing gated and non-gated lines. The stained points show DNA double strand breaks which is proportional to the dose delivered.	109
Figure 64. Plot profile of the γ -H2Ax stain in Figure 9.....	109
Figure 65. Beam profiles at 3 radii: 1.25mm, 1.77m, and 3.54mm. At the 1.25 radius: PVDR 4.2, 1.77mm radius: PVDR 7.3, 3.54mm radius: PVDR 16.7	112
Figure 66. Other simulated line geometries	113
Figure 67. PVDR vs Beam Spacing graph with a point at 900 μ m showing a PVDR of 14.13	114
Figure 68. Cross section of Apollo II showing the high voltage feedthrough, anode, and brazed oil cooling feedthrough. Below the anode is the X-ray window and under it is the rotating, variable beam width, three beam collimator.	117
Figure 69. Photo of the Apollo II Tube housing without any electrical connections.....	117
Figure 70. Anode operation showing the three electron beams hitting the 3 rows on the anode and being collimated into three microbeams along with the active oil cooling system	118

Figure 71. Anode with attached oil tubes seen through the side ports of the chamber.....	118
Figure 72. Cathode assembly timing diagram comparison between Apollo I and II	119
Figure 73. Top and side view photos of the cathode assembly.....	119
Figure 74. Adjustable multi-slit collimator design.....	121
Figure 75. Solidworks model of the enclosure.	123
Figure 76. Photos of the construction of the enclosure starting with the 2"x2" steel frame, the walls, and the winches that lift them.....	124

LIST OF ABBREVIATIONS

BIL – Blank Image Library

BNL – Brookhaven National Labs

CNT – Carbon Nanotube

GBM – Glioblastom multiforme

CT – Computed Tomography

ESRF – European Synchrotron Radiation Facility

FWHM – Full Width at Half Maximum

HVL – Half Value Layer

MRT – Microbeam Radiation Therapy

PVDR – Peak to Valley Dose Ratio

ROI – Region of Interest

RGA – Residual Gas Analyzer

RT – Radiation Therapy

SSD – Source to Surface Distance

SDBT – Stationary Digital Breast Tomosynthesis

SDCT – Stationary Digital Chest Tomosynthesis

TMZ – Temozolomide

CHAPTER 1: INTRODUCTION

1.1 Tomosynthesis

Digital tomosynthesis is a type of limited angle tomography that allows for 3D information reconstructed from a set of X-ray projection images taken at various angles. Tomosynthesis allows a way to filter out the unwanted structure overlap and focus on a specific slice in the object¹. The technology has been applied clinically for breast cancer screening and diagnosis², imaging of lung diseases³, and musculoskeletal imaging.



Figure 1. Two FDA approved digital breast tomosynthesis systems: GE SenoClaire and Hologic Selenia Dimensions.

Modern tomosynthesis tubes use a traditional X-ray tube, a mechanical arm to move the tube across an angular span, a digital detector, and a reconstruction algorithm that provides depth dependent X-ray images³. Digital tomosynthesis methods range from step and shoot methods that move and stop at each angle to obtain a projection, continuous motion that takes images at each angle with the tube stopping, and the more recent stationary tomosynthesis that uses a distributed source array to fire X-rays in succession.^{4 5}

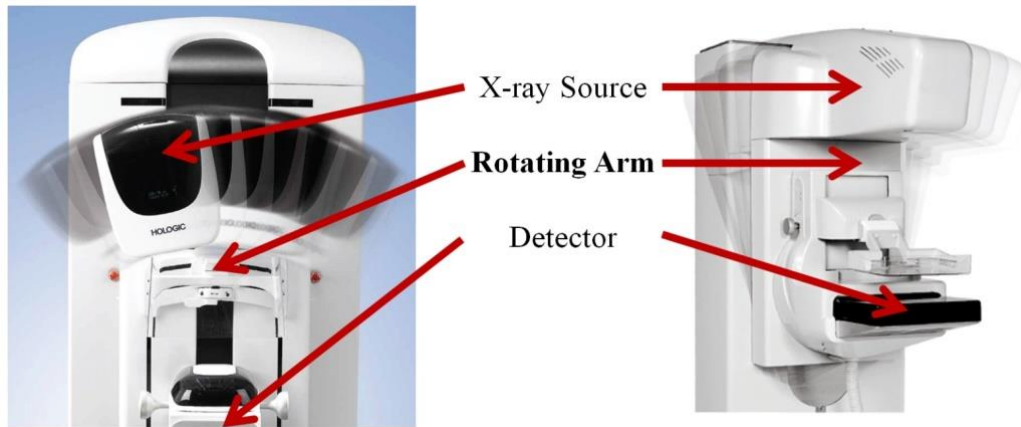


Figure 2. Hologic Selenia Dimensions tomosynthesis system showing the rotating gantry holding the source.

The below two images show tomosynthesis reconstruction slices from our stationary source array breast and chest 3D imaging systems. Figure 3 left shows the comparison between a 2D radiograph on the left and a reconstructed slice on the right. The mass in the circled region is completely obstructed by tissue above and below it in the mammogram but comes into clear view in the tomo reconstruction. Figure 3 right shows dental images. A is a photo of tooth phantom used in the imaging. B show the 2D radioagraph of phantom and C-F are the slices of a tomo set showing various carries that are not noticeable in B. An easy thing to note are the three roots in C and D that are indistinguishable in B.

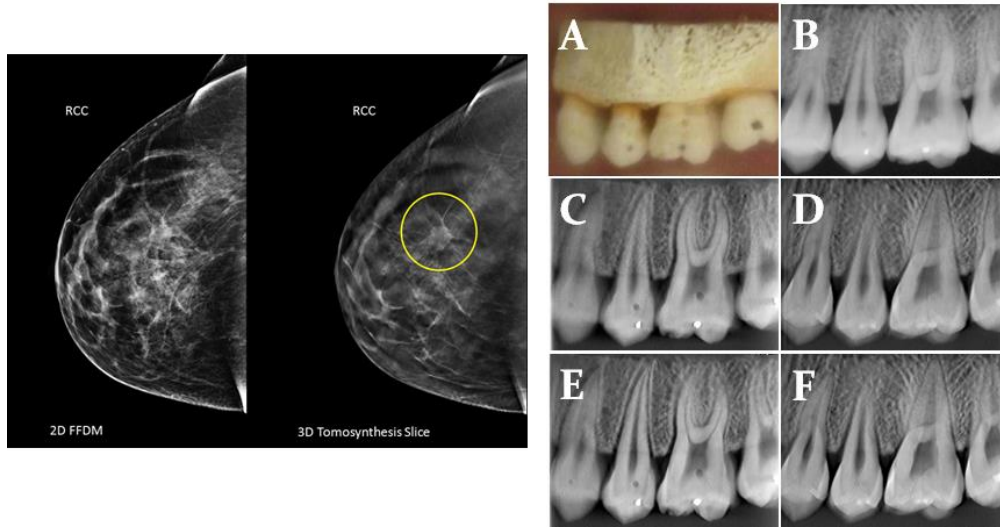


Figure 3. Image sets taken from our lab's custom-made stationary source array tomosynthesis systems. Left: Comparison of 2D mammo to a 3D tomo of breast tissue and the increase visibility of a lesion inside the tissue. Right: A) photo of tooth phantom B) 2D radioagraph of phantom C-F) Slices of a tomo set showing various carries that are not noticeable in B. Note the three roots in C and D that are hidden in B.

X-ray tomosynthesis reconstruction requires the knowledge of the precise locations of the X-ray source and the X-ray detector with respect to the object being imaged for each projection view taken. In the current commercial tomosynthesis scanners this is accomplished by moving the X-ray source in a fixed and repeatable trajectory and in precise and predetermined angular steps, using a rigid and mechanically stable gantry. Geometry calibration is performed periodically through imaging a phantom typically composed of multiple X-ray attenuating objects.⁶

1.2 Computed Tomography

Computed tomography (CT) is another type of 3D X-ray imaging system. Unlike tomosynthesis that keeps one plane in focus and thus suffers the results of blurring from out of plane features, CT completely eliminated artifacts from overlaying tissues⁷. The traditional way of taking a CT is to hold the source opposite a detector or series of detectors and to rotate the body, or the detector/source combination, about a stationary axis using a gantry. This produces a series of 2D projection images, which each horizontal 1D line being a projection of a 2D axial cross-section of the object at the imaging projection angle. A typical clinical CT is shown in Figure 4.



Figure 4. GE CT machine from <http://www3.gehealthcare.in/en/products/categories/computed-tomography>.

Seven generations of CT were developed in an effort to improve performance and image quality. These range from different source collimations – fan beams and cone beams and the no longer produced pencil beams and different detector geometries – from single, multiple, to detector rings.

Two categories of reconstruction methods exist for CT – analytical and iterative. An example of an analytic reconstruction is the filtered backprojection (FBP) method that is also used in tomosynthesis reconstruction. FBP has an advantage for being computationally efficient and numerical stable⁷

There are a variety of FBP methods developed for each type of CT geometry, but the general idea is summing all of the projection images at each angle over the entire angular span. A projection image is the summation of attenuations along the X-ray beam, which is the line integral of the object at a particular slice, in the case of a fan beam. The entire set of these projections is the Radon transform of the object, again at the particular slice. . If we denote the object in space as a function $f(x, y)$, the integral denoting the projection

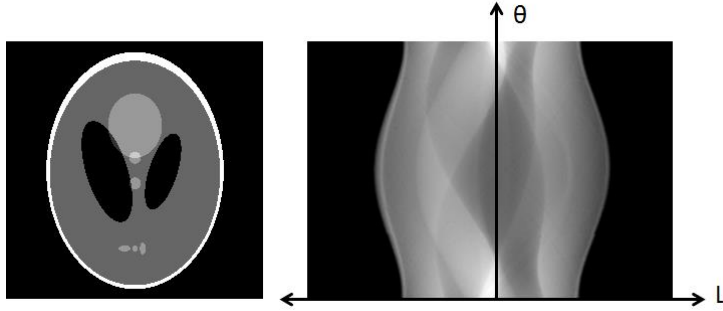


Figure 5. Shepp-Logan phantom (left) and its sinogram (right). Adapted from <https://tomroelandts.com/articles/tomography-part-3-reconstruction>.

image is:

$$g(l, \theta) = \int_{-\infty}^{\infty} f(x(s), y(s)) ds \text{ where}$$

$$x(s) = l \cos \theta - s \sin \theta \text{ and } y(s) = l \sin \theta + s \cos \theta. \text{ This is effectively}$$

taking a normal integral along a rotated plane – like the projection

images⁷.

A visualization of the Radon transform is known as a sonogram, with the projections plotted as a function of the angle of acquisition. The projection images tell us the attenuation over the X-ray beam path but not where along the path the attenuations were caused. To create an image, we can assign every point along the beam path the $g(l, \theta)$ value. This “smears” the projection image across the imaging space and produces what is known as a backprojection image:

$$b(x, y) = g(x \cos \theta + y \sin \theta, \theta)$$

Summing all of these smears over all of the rotation angles produces the backprojection summation image: $f_b(x, y) = \int_0^\pi b(x, y) d\theta$. After this, a ramp filter acting as a high pass filter removes the blurring of the image caused by the summations of discrete images. This

described method is not the preferred technique of reconstruction but the backprojection concept is used in a lot of clinical CTs now. The difference is the filtering, which is applied to the sinogram as either a multiplied frequency filter or as a convolution (known as a convolution backprojection) which is at times a more efficient operation.

CHAPTER 2: GEOMETRY CALIBRATION METHOD BASED ON PATTERN RECOGNITION

2.1 Current Clinical Geometry Calibration Methods

A common geometry calibration method used for clinical imaging systems involves the use of a bead phantom - a three dimensional block with metal beads in precisely known positions in two or more planes normal to the vertical direction. The phantom is placed on the detector in essentially any position and an X-ray projection image is taken. By comparing the two dimensional projection to the known three dimensional bead positions, the source position relative to the detector can be calculated using a linear projection method, as shown in Figure 6. The accuracy of this method is dependent on the accuracy of the bead positions, usually determined by a high resolution CT, the distance between the bead planes, and the ratio of the phantom height to the source-detector distance.

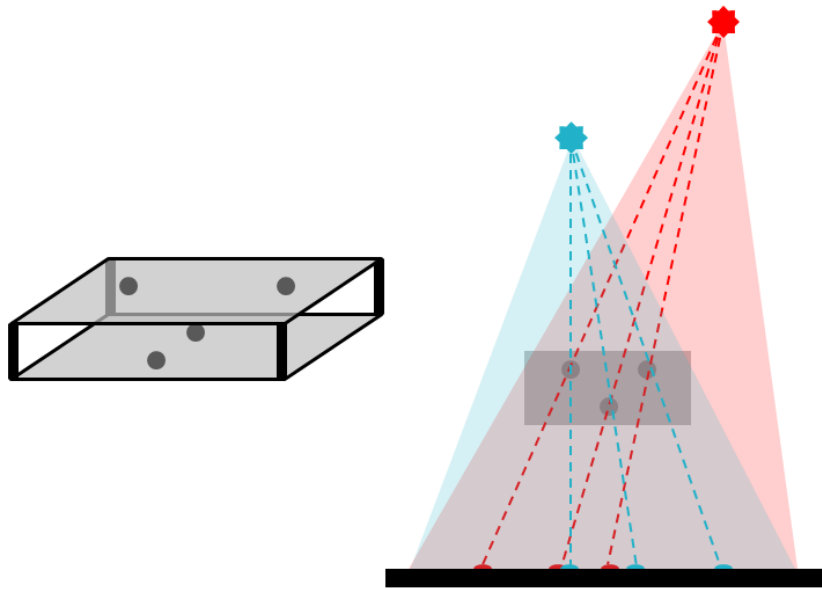


Figure 6. Bead phantom method of geometry calibration.

2.2 Pattern Detection

Pattern detection is a broad area of study in computer science. We focus specifically on optical pattern detection and further specify using the checkerboard pattern, which is popular with camera calibration techniques. There are a few calibration toolboxes out there, notably the OpenCV one by Jean-Yves Bouguet from Caltech (docs.opencv.org/2.4/doc/tutorials/calib3d/camera_calibration/camera_calibration.html) and

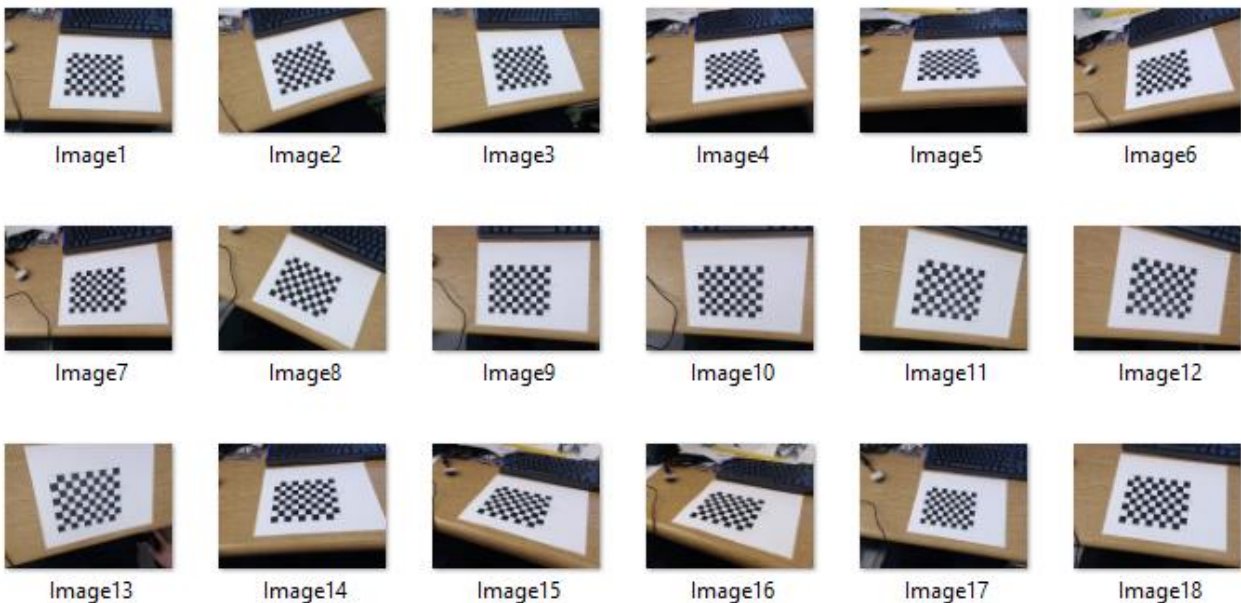


Figure 7. Camera calibration images using a checkerboard pattern in different orientations to provide accurate calibration

the newer one from Matlab, included with their computer vision package. Camera calibration is necessary to measure and correct for the camera's intrinsic, extrinsic, and lens-distortion parameters. This is accomplished by using a checkerboard pattern of known dimensions and taking a large set of images of it in different orientations. The algorithm creates the “perfect” pattern of known dimensions and using various rotation and skewing methods tries to fit the image to the modified ideal pattern. This can determine the skew, radial and tangential distortion of the lens, the principal point, and also the position of the

pattern relative to the focal point of the camera. This last bit of information is what we can use to do optical position tracking.

By providing an image set with a pattern, not only can one calibrate the camera to produce undistorted images, which though a useful feature in other research, does not provide us with any useful information, but one can use the calibration data to get the rotation and translation matrix data of the camera in the pattern coordinate system to < 0.2 pixels. Depending on the location of the pattern and your camera resolution, this can equate to sub-millimeter accuracy.

The image to the left in Figure 8 shows a processed checkerboard pattern image

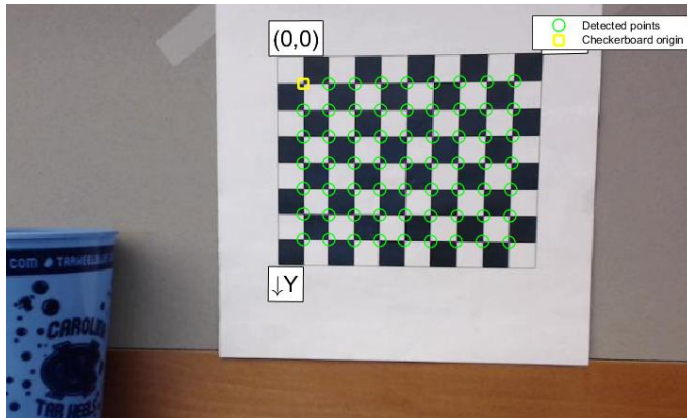


Figure 8. Processed checkerboard pattern image with the black square intersections highlighted along with the coordinate system axes.

with an overlay of detected points and coordinate axes. It looks for the X intersection between the squares and creates a grid that it later matched to the ideal and known grid dimensions. The coordinate system is also applied in the pattern space and shown here.

2.3 Optical Geometry Calibration Method

Here we present a method to perform three dimensional imaging using a decoupled source and detector without a rigid gantry or a predetermined source-detector trajectory. It uses an optical pattern recognition based method to accurately determine the imaging geometries of each projection images, in real time, for tomosynthesis reconstruction. The method can potentially allow tomosynthesis imaging to be performed in certain cases using a convention 2D imaging system with flexible and variable imaging geometry.

In a free form set-up, where the detector can be in any position relative to the source and moves from image to image, the relative positions of the source with respect to the detector need to be determined for each projection image. There are several ways to accomplish this using X-rays alone: placing the phantom on the detector alongside the object being imaged, putting the phantom, or markers, on the object and taking two images per position – one for calibration and one for the image set. The first cannot work if the object is as large as or larger than the detector and the second adds additional radiation.

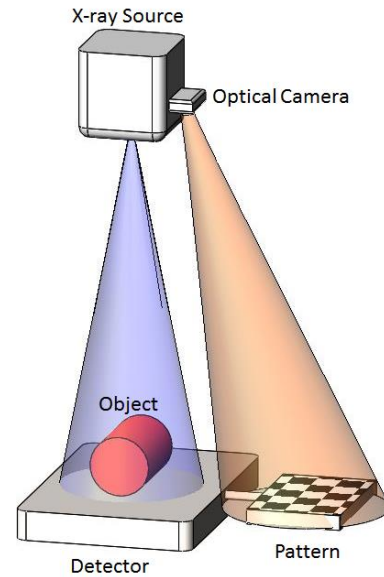


Figure 9. Setup modeled in Solidworks showing the camera and source attachment with the pattern and detector assembly.

Another option is to have a pattern of known size that is attached to the detector and tracked. The tracking allows for an accurate position of the pattern and the knowledge of the pattern's position relative to the detector allows for the calculation of the position of

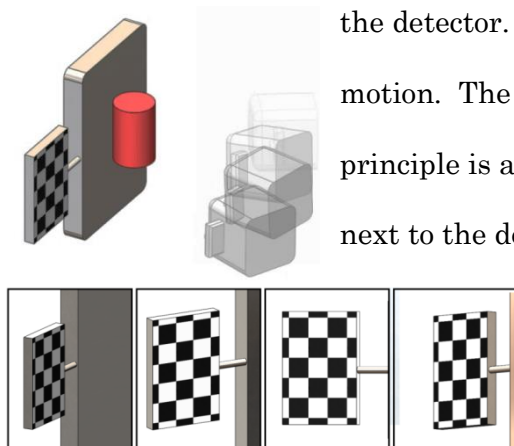


Figure 10. Camera/source motion about an object and camera views of the pattern at each position

the detector. We accomplish this by using a camera to track the motion. The location is based on relative position change. The principle is as follows: a checkerboard pattern is positioned on or next to the detector using an extension arm in such a way that the

pattern will not move relative to the detector. A camera is mounted on the source in a way that the pattern is visible during imaging and will not move relative to the source, shown in Figure 9.

The camera is then used to determine the source positions based on the orientation of the camera to the pattern. Figure 10 shows a sweeping source motion about an object and provides the camera view for each. The pattern rotation and position allows for an absolute position calculation to be performed. Checkerboard pattern recognition has been widely used in camera calibration and feature extraction and we use the same pattern for both in our procedure.

2.4 Stationary Detector

In the reconstruction, there are three coordinate systems: the camera (CC) that has the origin at the focal spot with the Z-axis being the vertical axis perpendicular to the lens pointing away from the camera, the detector (DC) that has the origin in the middle, with the positive X and Y axes being to the right and down respectively when looking at it from the top, and the pattern (PC) where the origin is the top left corner intersection of the 4 squares with the X and Y axes in the same direction as with the detector. This assumes that the detector is stationary during the entire imaging process and creates the “world coordinate system” in which all of the above objects reside.

Using the computer vision library, the camera’s intrinsic parameters (lens distortion, tangential skew, zoom) are obtained using a series of calibration images taken of the pattern in various positions/rotation. After this initial camera calibration is performed (unrelated to anything in the free form tomo system), the X-ray to camera calibration can

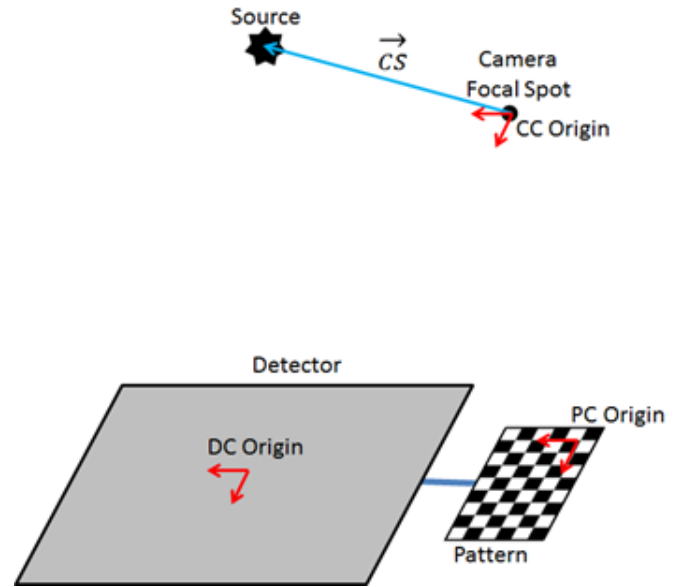


Figure 11. Source, Camera, Detector, and Pattern setup.

begin. The source/camera system is moved about the detector/pattern system, making certain neither component in each system is moved relative to each other, and an X-ray and corresponding optical image of the pattern is taken at each position. Using the intrinsic parameters from the initial calibration, the camera's translation and rotation vectors can be obtained, which relate points in the camera coordinate system (X_{CC}) with points in the pattern coordinate system (X_{PC}) using the matrix transform:

$$X_{CC} = RX_{PC} + t \quad (1)$$

From this, the camera position in the PC coordinate system can be obtained:

$$X_{PC} = -R^{-1}t \quad (2)$$

Next, DC needs to be related to PC. As the two are connected, their position can be determined in a number of ways. We assume that the two planes are parallel and their transform is a linear one, with M_x, M_y, M_z being the linear offsets between DC and PC. This is true for our system where we control our pattern positioning. The transform can be applied to a randomly rotated/translated pattern to detector plane as well.

$$X_{DC} = X_{PC} - \begin{bmatrix} M_x \\ M_y \\ M_z \end{bmatrix} \quad (3)$$

The final relation is the source position to the camera focal spot, after which the source position to the detector can be obtained from the above transforms. To do that, the calibration phantom is used to first get the source in the DC coordinate system. This is done using a standard geometry calibration phantom and ray tracing.

The calibration is completed by accurately getting the \vec{CS} vector. From the geometry phantom, we get the position of the source in the DC frame, which, using (3), we can get in the PC frame. Using (1), we can put it all back into the camera coordinate system. Plotting

all of the vectors from the origin (camera focal spot) to the source should theoretically all give the same vector, but due to measurement errors, gives slightly different results, shown plotted in Figure 12. Taking the average of those gives us the \vec{CS} vector, shown in red.

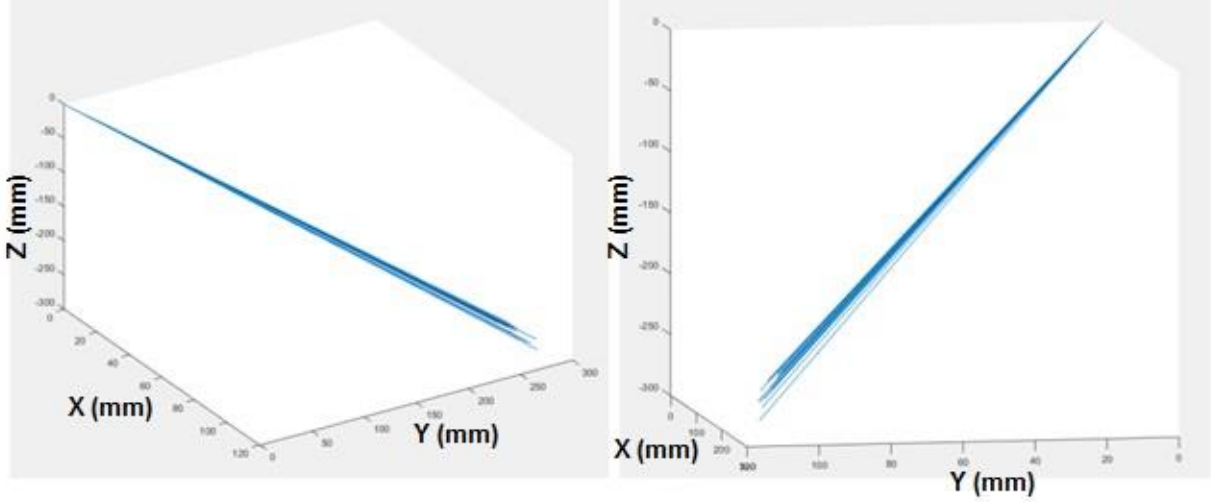


Figure 12. Two views of source to camera vector lines plotted in CC with the average vector in red.

This completes the calibration procedure. From then, any new X-ray and corresponding optical image can be processed to determine the position of the source to the detector. Using the \vec{CS} vector and (1), the source in DC can be found by:

$$Source_{DC} = R^{-1}(CS - t) - M \quad (4)$$

2.5 Moving Detector

The angular coverage is limited in stationary detector tomosynthesis. This reduces the image resolution in the z direction and is a major concern in any tomosynthesis system. To resolve this, the detector must move about the object which is to remain fixed, much like in a CT. Allowing larger angular coverage would allow for better object resolution and to perform novel imaging geometries to further enhance the image quality.

Currently, the algorithm accounts for a stationary detector/object and looks at the camera projections relative to the detector. We can take an array of images at one detector position, move the detector about the body, and repeat the process and end up with multiple sets of projection images at multiple detector positions, but without a central coordinate system. A sample problem would be as follows: three projection images are taken for each detector position and the detector is rotated by 90° about the body, like the diagram in Figure 13.

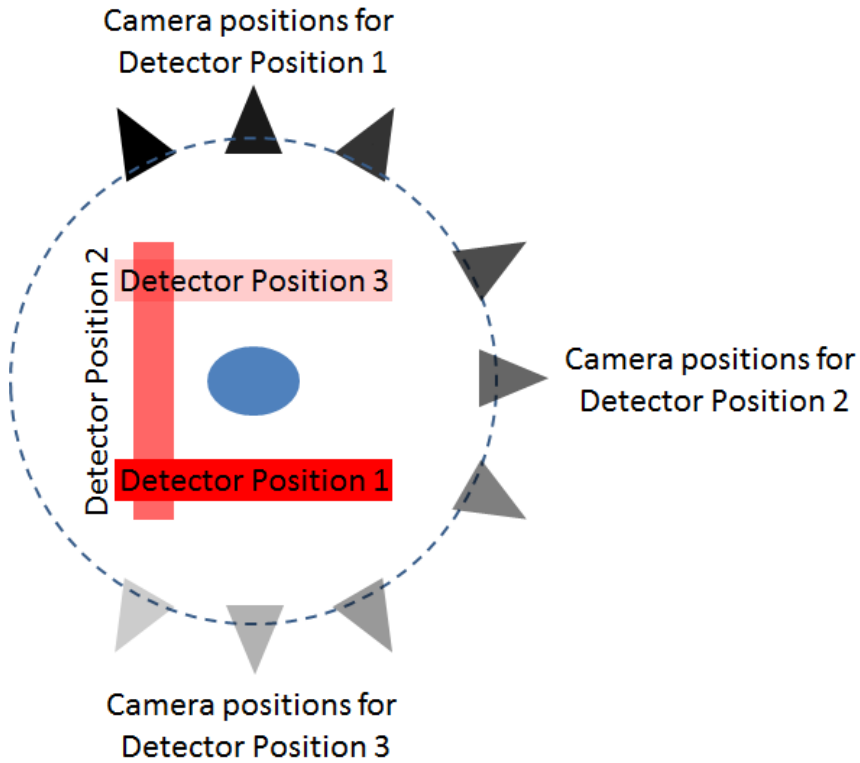


Figure 13. Sample large angle tomo setup diagram.

To begin to solve this problem of placing a moving source and detector into one coordinate system, let's remove the X-ray projections for now and talk only about the optical camera images and how to put all of the camera positions into the same coordinate system. From the initial calibration, we obtain the positions (rotation and translation matrices) of

each of the cameras relative to the detector (pattern in this sample case). This effectively gives the pattern and camera centric views, shown in Figure 14. The goal is to position the views of the detector positions 2 and 3 to reconstruct the original setup in Figure 13.

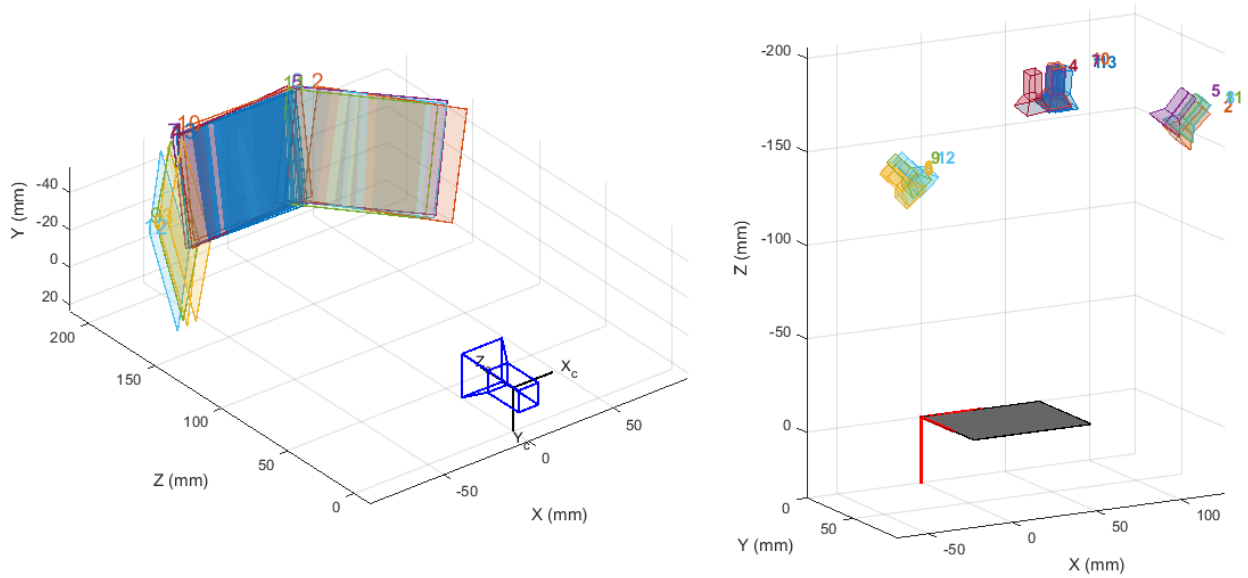


Figure 14. Camera centric and pattern centric views of three images taken at each detector position.

To accomplish this, there needs to be a link between the detector positions. Up until now, we have worked with the pattern centric setup and obtained positions of the cameras relative to the one detector. The key in linking the detector positions is switching the coordinate views and moving to a camera centric system during the detector move. This involves keeping the camera stationary and taking an image before the move and after the move, and then transferring the coordinate system origin back to the detector, only in its second position. This process is repeated for as many detector translations as necessary.

Let's further simplify the process and graphically explain the basic steps in Figure 15. The camera is at position C1 and the detector is at D1. An image is taken. The camera

is moved to C2 while the detector is fixed and another image is taken. So far, the process is the same as before. Now we want to move the detector to D2. The camera is kept fixed at C2, the detector is moved to D2, and another image is taken (image 3) from C2. The camera can then be moved (while the detector is again kept stationary in its new position at D2) to C4 and an image is taken. It is moved to C5 and another image is taken. We decide to move the detector again. The camera is held stationary at C4, the detector is moved to D3, and image 6 is taken. Now the camera is free to move about the detector as before.

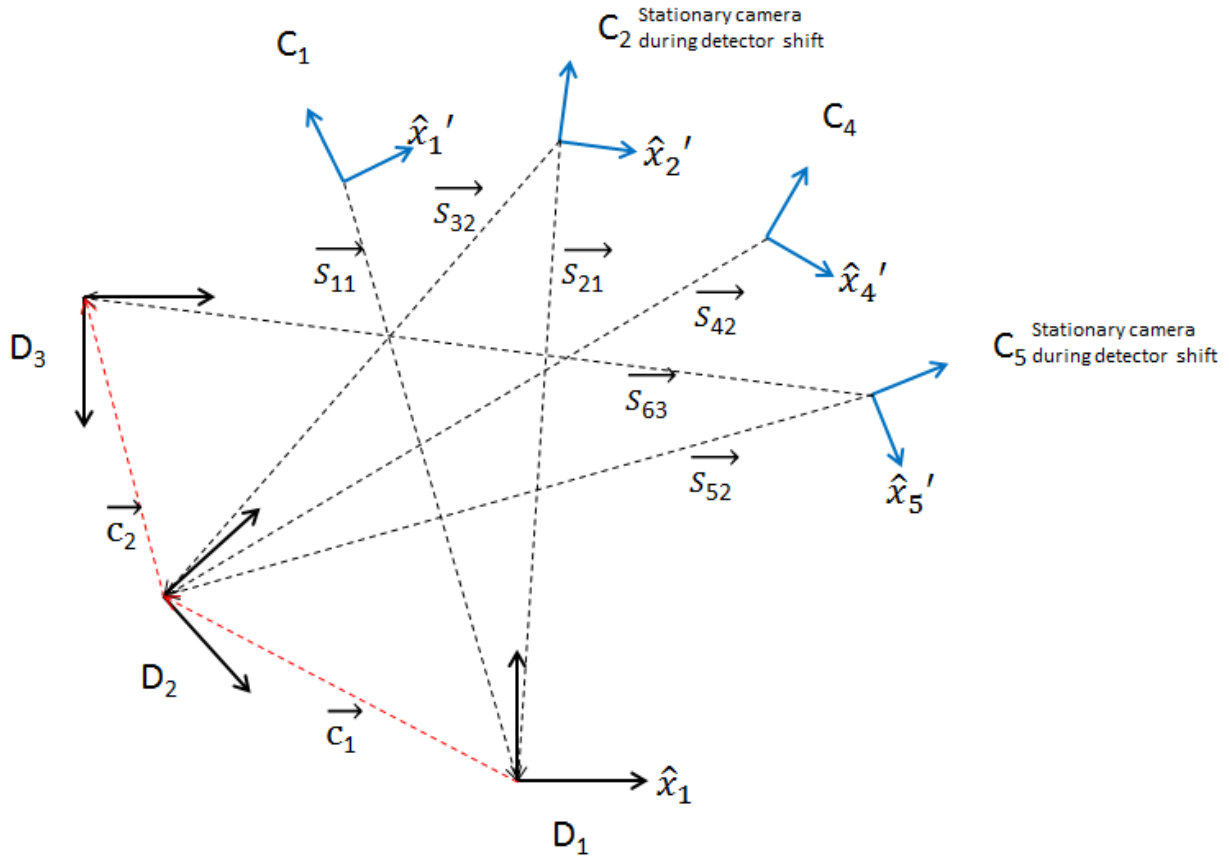


Figure 15. Large angle tomosynthesis diagram.

Now we can discuss the reconstruction procedure. Every camera image produces a rotation and translation vector to its respective detector in the detector coordinate system.

There are 3 coordinate system families that are in play (Camera Coordinate - \hat{x}_n' , Detector Coordinate - \hat{x}_n , and the world coordinate system that the body lives in) in Figure 15.

Vector \vec{S}_{ab} represents the vector from a camera to its pattern origin, where a is the camera position (image #) and b is the coordinate system the image is associated with. Every \vec{S}_{ab} has an associated rotation matrix R_{ab} and translation vector t_{ab} .

The coordinate transform from the camera coordinate system to detector is:

$$X_{CC} = RX_{PC} + t \quad (5)$$

which is the position of the camera in image “a” in the D_b coordinate system. \vec{S}_{21} and \vec{S}_{32} relate D_1 and D_2 because they are taken while the camera was stationary in the world coordinates. From this point, D_1 is set at the origin of the world coordinates.

To find the locations of other points in D_2 , such as $S_{4,2}$, and transform them into D_1 (dubbed $S_{4,1}$), we can follow the procedure: In \hat{x}_2'

$$\vec{S}_{42\hat{x}_2} = R_{32}(\vec{S}_{42}) + t_{32} \quad (6)$$

where

$$\vec{S}_{42} = -R_{42}^{-1}t_{42} \quad (7)$$

in \hat{x}_2 described above. Transforming back into \hat{x}_1 :

$$\vec{S}_{42\hat{x}_1} \text{ also known as } \vec{S}_{41} = R_{21}^{-1}(\vec{S}_{42\hat{x}_2}) - t_{21} = \vec{S}_{41} = R_{21}^{-1}(R_{32}(\vec{S}_{42}) + t_{32}) - t_{21} \quad (8)$$

This is a recursive transform that must be taken at each new detector position. To do so, a list of all of the image numbers that precede a detector transition is necessary: steps=[a,b,c,d,...]. In the above diagram, steps is equal to [2,5].

To find the position of the camera of image α which is in the coordinate system of Detector β , the following recursive function is used:

$$\vec{S}_{\alpha,\beta-1} = R_{\gamma,\beta}^{-1}(R_{\gamma+1,\beta+1} * S_{\alpha,\beta} + t_{\gamma+1,\beta+1} - t_{\gamma,\beta}) \quad (9)$$

Where γ is the maximum position number in steps that is less than α and β is its index position in 'steps' (which coincides with the D coordinate system). This is repeated until $\beta=1$ (in Detector 1 coordinate system, ie the world coordinates)

Now we take a look at the rotation matrices:

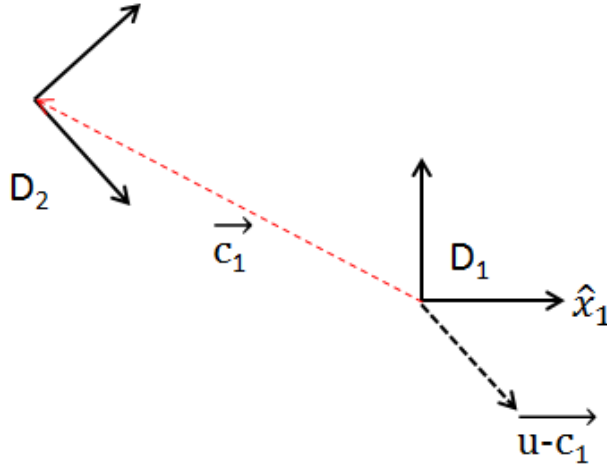


Figure 16. Rotation matrix between detectors illustration

Let $\vec{u} = \langle 1, 0, 0 \rangle$ the x axis in any coordinate system as illustrated above. \vec{u} in \hat{x}_2 can be written as

$$W\vec{u} + c_1 \text{ in } \hat{x}_1 \quad (10)$$

Following our previous transform

$$R_{21}^{-1}(R_{32}(\vec{u}) + t_{32}) - t_{21} = W\vec{u} + c_1 \quad (11)$$

$$R_{21}^{-1}R_{32}(\vec{u}) + R_{21}^{-1}t_{32} - R_{21}^{-1}t_{21} = W\vec{u} + c_1 \quad (12)$$

$$W = R_{21}^{-1} R_{32} \quad (13)$$

$$c_1 = R_{21}^{-1} t_{32} - R_{21}^{-1} t_{21} \quad (14)$$

So to get the rotation matrix, for example, of R_{41} , we would use: $R_{41}=R_{42}*W_2$. We apply the same recursive technique as before for multiple detector transforms:

$$W_{\beta+1} = W_{\beta} * R_{\gamma+1, \beta+1}^{-1} R_{\alpha, \beta} \quad (15)$$

$$W_2 = R_{32}^{-1} R_{21} \quad (16)$$

The next step is taking a look at the error propagation of this recursive function. Every camera position error relative to the detector is independent of the previous positions but every absolute position calculation from a camera position taken relative to a moved detector will have an increased error that propagated from the detector motion. From the recursive position formula 9, the maximum error will be on the last detector's image set, so limiting the detector positions reduces the error.

From a single camera projection, the uncertainty is:

$$s = \sqrt{\left(\frac{\partial S}{\partial x}\right)^2 s_x^2 + \left(\frac{\partial S}{\partial y}\right)^2 s_y^2 + \left(\frac{\partial S}{\partial z}\right)^2 s_z^2 + \left(\frac{\partial S}{\partial \theta}\right)^2 s_{\theta}^2 + \left(\frac{\partial S}{\partial \varphi}\right)^2 s_{\varphi}^2 + \left(\frac{\partial S}{\partial \psi}\right)^2 s_{\psi}^2} \quad (17)$$

where θ , φ , and ψ are the Euler angles of the rotation matrix. The rotation matrix can be represented as a combination of the three coordinate axis rotations:

$$R = R_z(\varphi) R_y(\theta) R_x(\psi) \quad (18)$$

$$R_x(\psi) = \begin{bmatrix} 1 & 0 & 0 \\ 0 & \cos\psi & -\sin\psi \\ 0 & \sin\psi & \cos\psi \end{bmatrix} \quad (19)$$

$$R_y(\theta) = \begin{bmatrix} \cos\theta & 0 & \sin\theta \\ 0 & 1 & 0 \\ -\sin\theta & 0 & \cos\theta \end{bmatrix} \quad (20)$$

$$R_z(\varphi) = \begin{bmatrix} \cos\varphi & -\sin\varphi & 0 \\ \sin\varphi & \cos\varphi & 0 \\ 0 & 0 & 1 \end{bmatrix} \quad (21)$$

$$R = \begin{bmatrix} \cos\theta \cos\varphi & \sin\psi \sin\theta \cos\varphi - \sin\varphi \cos\psi & \cos\psi \sin\theta \cos\varphi + \sin\varphi \sin\psi \\ \cos\theta \sin\varphi & \sin\psi \sin\theta \sin\varphi + \cos\varphi \cos\psi & \cos\psi \sin\theta \sin\varphi - \cos\varphi \sin\psi \\ -\sin\theta & \sin\psi \cos\theta & \cos\psi \cos\theta \end{bmatrix} \quad (22)$$

By expanding 17, the uncertainty becomes:

$$s = \sqrt{\begin{aligned} &\left(R \begin{pmatrix} 1 \\ 0 \\ 0 \end{pmatrix}\right)^2 s_x^2 + \left(R \begin{pmatrix} 0 \\ 1 \\ 0 \end{pmatrix}\right)^2 s_y^2 + \left(R \begin{pmatrix} 0 \\ 0 \\ 1 \end{pmatrix}\right)^2 s_z^2 + \\ &\left(\frac{dR}{d\theta} t\right)^2 s_\theta^2 + \left(\frac{dR}{d\varphi} t\right)^2 s_\varphi^2 + \left(\frac{dR}{d\psi} t\right)^2 s_\psi^2 \end{aligned}} \quad (23)$$

$$\frac{\partial R}{\partial \theta} = \begin{bmatrix} -\sin\theta \cos\varphi & \sin\psi \cos\theta \cos\varphi & \cos\psi \cos\theta \cos\varphi \\ -\sin\theta \sin\varphi & \sin\psi \cos\theta \sin\varphi & \cos\psi \cos\theta \sin\varphi \\ -\cos\theta & -\sin\psi \sin\theta & -\cos\psi \sin\theta \end{bmatrix} \quad (24)$$

$$\frac{\partial R}{\partial \varphi} = \begin{bmatrix} -\cos\theta \sin\varphi & -\sin\psi \sin\theta \sin\varphi - \cos\varphi \cos\psi & -\cos\psi \sin\theta \sin\varphi + \cos\varphi \sin\psi \\ \cos\theta \cos\varphi & \sin\psi \sin\theta \cos\varphi - \sin\varphi \cos\psi & \cos\psi \sin\theta \cos\varphi + \sin\varphi \sin\psi \\ 0 & 0 & 0 \end{bmatrix} \quad (25)$$

$$\frac{\partial R}{\partial \psi} = \begin{bmatrix} 0 & \cos\psi \sin\theta \cos\varphi + \sin\varphi \sin\psi & -\sin\psi \sin\theta \cos\varphi + \sin\varphi \cos\psi \\ 0 & \cos\psi \sin\theta \sin\varphi - \cos\varphi \sin\psi & -\sin\psi \sin\theta \sin\varphi - \cos\varphi \cos\psi \\ 0 & \cos\psi \cos\theta & -\sin\psi \cos\theta \end{bmatrix} \quad (26)$$

$$s = \sqrt{\begin{aligned} & \left[\begin{array}{c} (\cos\theta \cos\varphi)^2 s_x^2 \\ (\cos\theta \sin\varphi)^2 s_x^2 \\ (\sin\theta)^2 s_x^2 \end{array} \right] + \left[\begin{array}{c} (\sin\psi \sin\theta \cos\varphi - \sin\varphi \cos\psi)^2 s_y^2 \\ (\sin\psi \sin\theta \sin\varphi + \cos\varphi \cos\psi)^2 s_y^2 \\ (\sin\psi \cos\theta)^2 s_y^2 \end{array} \right] + \left[\begin{array}{c} (\cos\psi \sin\theta \cos\varphi + \sin\varphi \sin\psi)^2 \\ (\cos\psi \sin\theta \sin\varphi - \cos\varphi \sin\psi)^2 \\ (\cos\psi \cos\theta)^2 \end{array} \right] + \\ & \left(\begin{bmatrix} -\sin\theta \cos\varphi & \sin\psi \cos\theta \cos\varphi & \cos\psi \cos\theta \cos\varphi \\ -\sin\theta \sin\varphi & \sin\psi \cos\theta \sin\varphi & \cos\psi \cos\theta \sin\varphi \\ -\cos\theta & -\sin\psi \sin\theta & -\cos\psi \sin\theta \end{bmatrix} t \right)^2 s_\theta^2 + \\ & \left(\begin{bmatrix} -\cos\theta \sin\varphi & -\sin\psi \sin\theta \sin\varphi - \cos\varphi \cos\psi & -\cos\psi \sin\theta \sin\varphi + \cos\varphi \sin\psi \\ \cos\theta \cos\varphi & \sin\psi \sin\theta \cos\varphi - \sin\varphi \cos\psi & \cos\psi \sin\theta \cos\varphi + \sin\varphi \sin\psi \\ 0 & 0 & 0 \end{bmatrix} t \right)^2 s_\varphi^2 + \\ & \left(\begin{bmatrix} 0 & \cos\psi \sin\theta \cos\varphi + \sin\varphi \sin\psi & -\sin\psi \sin\theta \cos\varphi + \sin\varphi \cos\psi \\ 0 & \cos\psi \sin\theta \sin\varphi - \cos\varphi \sin\psi & -\sin\psi \sin\theta \sin\varphi - \cos\varphi \cos\psi \\ 0 & \cos\psi \cos\theta & -\sin\psi \cos\theta \end{bmatrix} t \right)^2 s_\psi^2 \end{aligned}} \quad (27)$$

If the camera is directly above the pattern and its axes align with the pattern's coordinate axes:

$$t = \begin{bmatrix} 0 \\ 0 \\ 800 \end{bmatrix} \quad \theta = 0^\circ \quad \varphi = 0^\circ \quad \psi = 0^\circ \quad (28)$$

$$s_x = 0.2\text{mm} \quad s_y = 0.2\text{mm} \quad s_z = 0.6\text{mm} \quad (29)$$

$$s_\theta = 0.1^\circ \quad s_\varphi = 0.1^\circ \quad s_\psi = 0.1^\circ \quad (30)$$

Gives an uncertainty vector:

$$s = \begin{bmatrix} 1.41 \\ 1.41 \\ 0.600 \end{bmatrix} \quad (31)$$

Entering the following realistic parameters:

$$t = \begin{bmatrix} 50 \\ 50 \\ 800 \end{bmatrix} \quad \theta = 15^\circ \quad \varphi = 5^\circ \quad \psi = 5^\circ \quad (32)$$

$$s_x = 0.2\text{mm} \quad s_y = 0.2\text{mm} \quad s_z = 0.6\text{mm} \quad (33)$$

$$s_\theta = 0.1^\circ \quad s_\varphi = 0.1^\circ \quad s_\psi = 0.1^\circ \quad (34)$$

Gives an uncertainty vector:

$$s = \begin{bmatrix} 1.40 \\ 1.38 \\ 0.670 \end{bmatrix} \quad (35)$$

Trying a closer distance at $t_z = 500\text{mm}$ logically drops the uncertainty to:

$$s = \begin{bmatrix} 0.906 \\ 0.886 \\ 0.615 \end{bmatrix} \quad (36)$$

The above is the uncertainty for a single position detector. Adding a second detector position complicates the position vector, obtained from (9) to:

$$\vec{S}_{\alpha,1} = R_{\gamma,1}^{-1}(R_{\gamma+1,2} * S_{\alpha,2} + t_{\gamma+1,2} - t_{\gamma 1}) \quad (37)$$

Following equation 17, the uncertainty now becomes:

$$s = \sqrt{\begin{aligned} & \left(\frac{\partial S}{\partial x_{t_{\gamma,1}}} \right)^2 s_{x_{t_{\gamma,1}}}^2 + \left(\frac{\partial S}{\partial y_{t_{\gamma,1}}} \right)^2 s_{y_{t_{\gamma,1}}}^2 + \left(\frac{\partial S}{\partial z_{t_{\gamma,1}}} \right)^2 s_{z_{t_{\gamma,1}}}^2 + \\ & \left(\frac{\partial S}{\partial x_{t_{\gamma+1,2}}} \right)^2 s_{x_{t_{\gamma+1,2}}}^2 + \left(\frac{\partial S}{\partial y_{t_{\gamma+1,2}}} \right)^2 s_{y_{t_{\gamma+1,2}}}^2 + \left(\frac{\partial S}{\partial z_{t_{\gamma+1,2}}} \right)^2 s_{z_{t_{\gamma+1,2}}}^2 + \\ & \left(\frac{dS}{d\theta_{R_{\gamma,1}}} \right)^2 s_{\theta_{R_{\gamma,1}}}^2 + \left(\frac{dS}{d\phi_{R_{\gamma,1}}} \right)^2 s_{\phi_{R_{\gamma,1}}}^2 + \left(\frac{dS}{d\psi_{R_{\gamma,1}}} \right)^2 s_{\psi_{R_{\gamma,1}}}^2 + \\ & \left(\frac{dS}{d\theta_{R_{\gamma+1,2}}} \right)^2 s_{\theta_{R_{\gamma+1,2}}}^2 + \left(\frac{dS}{d\phi_{R_{\gamma+1,2}}} \right)^2 s_{\phi_{R_{\gamma+1,2}}}^2 + \left(\frac{dS}{d\psi_{R_{\gamma+1,2}}} \right)^2 s_{\psi_{R_{\gamma+1,2}}}^2 + \\ & \left(\frac{\partial S_{\alpha 2}}{\partial x} \right)^2 s_x^2 + \left(\frac{\partial S_{\alpha 2}}{\partial y} \right)^2 s_y^2 + \left(\frac{\partial S_{\alpha 2}}{\partial z} \right)^2 s_z^2 + \left(\frac{\partial S_{\alpha 2}}{\partial \theta} \right)^2 s_{\theta}^2 + \left(\frac{\partial S_{\alpha 2}}{\partial \phi} \right)^2 s_{\phi}^2 + \left(\frac{\partial S_{\alpha 2}}{\partial \psi} \right)^2 s_{\psi}^2 \end{aligned}} \quad (38)$$

From equation 38, it can be seen that the error increases with each additional detector position. Looking at equation 17, adding an additional detector position adds two more translation vectors and two rotation matrices. To show an example of this, Figure 17 is a graph of the error accumulation of a CT data set (described in Chapter 5). The set has 4 detector shifts which are seen with the jumps in the plot. The difference was calculated by taking the measurements obtained from the rotation and translation data and

subtracting from the data obtained by introducing an error to the values: 0.0002 to the rotation matrix and 0.05 to the X and Y and 0.13 to the Z in the translation vector (the approximate errors from the calibration output data).

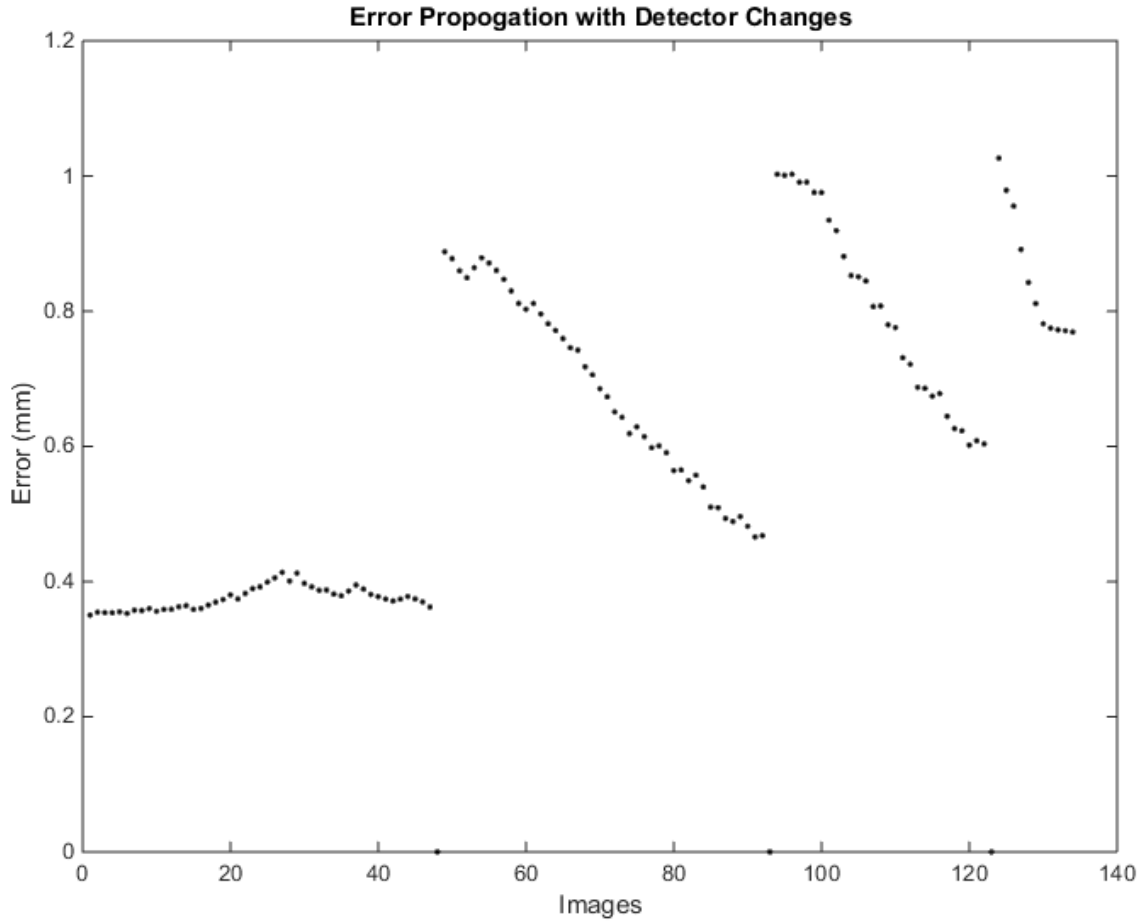


Figure 17. Error propagation simulation showing the absolute position error (in mm) accumulating with each position change.

CHAPTER 3: FREE FORM TOMOSYNTHESIS

3.1 Motivation

We will now take a look at three implementations of the optical geometry calibration method, starting with a general free form tomosynthesis. As stated before, current clinical tomo systems all have either a fixed gantry for motion or are operating under conditions that prevent the source and the detector from moving relative to each other. While the process works reasonably well for systems stationed in dedicated spaces, it becomes cumbersome and often impractical for mobile and field operations. The heavy mechanical gantry needed for mechanical stability takes space and makes it difficult to design mobile tomosynthesis scanners that can be useful in situations where the patient cannot be easily transferred, such as those with neck trauma or severe burns. Finally, the fixed trajectory limits the imaging to a linear arc acquisition due to practical engineering constraints, which may not be the most efficient projection image set.

Using our method, we can perform tomosynthesis imaging using a decoupled source and detector without a rigid gantry or a predetermined source-detector trajectory. This can potentially allow tomosynthesis imaging to be performed in certain cases using a conventional 2D imaging system with flexible and variable imaging geometry. There are several hand-held imaging devices on the market already, such as the NOVO system pictured in Figure 18. These provide quick 2D projection images of potentially dangerous containers out in the field. Adding a 3D imaging component would increase the visibility and allow for segmentation of the articles inside.



Figure 18. Portable, handheld X-ray security imaging devices by NOVO Digital Radiography
<http://www.novo-dr.com/>.

There are methods that have been developed to accommodate imaging with a non-fixed detector. Gauntt et al. uses a motor control method of tube alignment⁸. The tube head has a six degree of freedom motor system that performs minor adjustments to the tube position after approximate alignment by the technician. The alignment software looks at a protruding cross shape with LEDs and its shape from the camera point of view determines the necessary adjustments to be directly above the center of the detector⁸. Other methods include using light patterns to position the detector in a predetermined orientation^{9,10}

These all, however, attempt to position the detector to a specific orientation relative to the source. The calibration method will not only determine the source locations for reconstruction, but will also detect any motion during imaging and potentially still be able to reconstruct the images as every position for each image is known.

3.2 Application

For the optical imaging, a Logitech HD Pro Webcam C920 camera was used and was calibrated using the computer vision toolbox in Matlab that provides all the intrinsic

parameters to be used during the optical reconstruction. The resolution was set to 1920 x 1080 with auto-focus turned off. Knowledge of the relative position of the camera relative to the source focal spot is necessary to perform the geometry calculation. For this one-time measurement, a standard metal bead calibration phantom that is suited to determine the absolute position of the source(s) to the detector for stationary tomosynthesis is used. The phantom is placed on the detector/pattern assembly and a few calibration X-ray and optical images are taken at different orientations. This provides the absolute source focal spot positions relative to the detector and the absolute optical focus spot position relative to the pattern. Since the position of the pattern relative to the detector is known, the position of the source can be determined relative to the optical focal spot. Once the camera/source system is calibrated, the phantom is no longer needed as the position of the pattern to the camera can be used to determine the position of the source to the detector. The method is summarized in the flowchart in Figure 19.

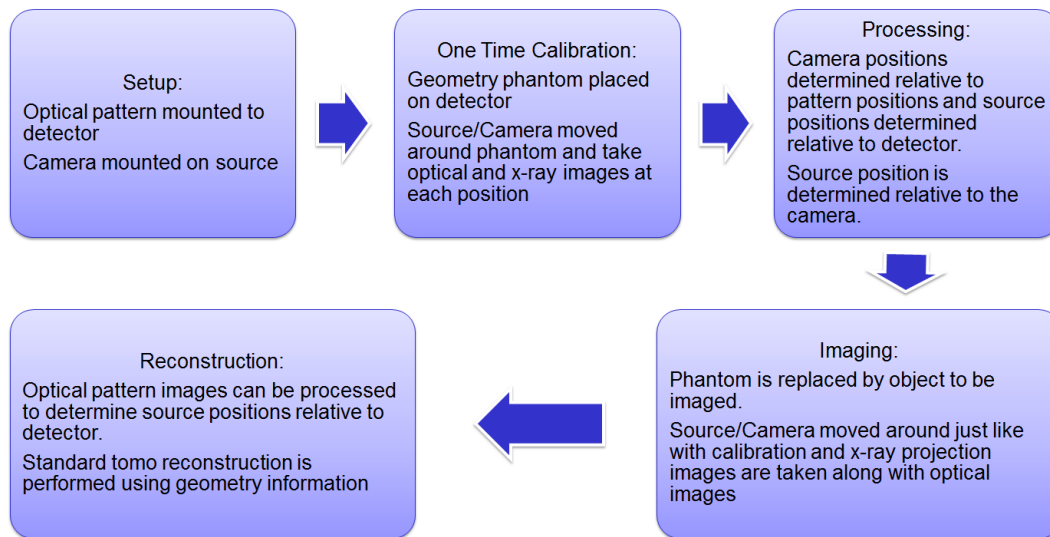


Figure 19. Flow chart of free form imaging process.

The camera was mounted onto the source head using a strap as shown in the setup image below. A key point to note is the duct tape holding the loose end of the camera. In

case the camera USB is ever pulled, which happens considering the source head's range of motion, the pulling will hit the tape and not the actual camera, making sure the source and camera are always stationary relative to each other. This is a very important setup tip any time the camera is mounted on.

The optical pattern is taped onto the detector in the case of the DRX imaging system but can also be attached off the detector with a connecting holder as seen later with the intraoral system. The optical pattern is made so about 20% of the FOV is the pattern during the imaging. In the case below, the pattern was 9x6 (make sure that the pattern is not symmetric to allow for rotation of the detector without confusion with 19mm squares. The (0,0,0) point is shown in Figure 20 which is always at the top left corner when the two black squares are at the top right and left. This is what the pattern recognition software detects. After the imaging session, two beads are placed at the origin and at the far right cross of the pattern to relate the pattern position to the detector. An X-ray is taken of the beads which puts the pattern origin and its x-axis into the detector coordinate space.



Figure 20. Setup using the Carestream DRX Revolution mobile imaging unit. Left: Camera mounting bracket and safety tape holding loose USB Right: Detector with optical pattern placement and beads (attached post imaging to relate pattern to detector).

3.3 Accuracy

We tested the accuracy of the optical tracking by using a precision translation stage and moving the camera setup a known distance in three dimensions and then comparing those distance to the ones calculated by the system. This gave us a minimum error threshold assuming perfection conditions. The conditions that affected the accuracy were also tested, including the distance from the pattern and the camera resolution.

We then tested the accuracy of the relative positioning by using the calibration phantom as the absolute reference. The Logitech HD Pro Webcam C920 was attached to an X-ray unit and the phantom was optically and X-ray imaged as the camera/X-ray unit was moved around it. The motion detected by the camera was compared to the motion obtained from the X-ray projection geometry calculation. Both of the position sets obtained from the

X-ray geometry phantom and the optical geometry were used to reconstruct the calibration phantom. The comparison can be seen in Figure 25.

Feasibility testing was performed on a foot and hand phantom with the geometry calibration phantom next to each to compare reconstructions using the absolute geometry from the phantom and that obtained using the optical imaging method. The geometry phantom was rigidly attached to the detector alongside the hand and foot.

The parameters contributing to accuracy that were investigated were the camera resolution and the distance from the pattern. The optimal resolution for the camera was found to be 1920x1080. Anything higher did not result in better accuracy and resulted in slower acquisition

time. The distance from the pattern played a major role but was also correlated with the pattern size so the better parameter to look at was the percentage of the image that was the pattern, which took into account both the distance and the pattern size. Unsurprisingly, it was found that the larger the pattern in the image, the smaller the error, as shown in Figure 21, so it was aimed to keep the pattern filling about 20% of the image during imaging. Two cameras were used to reduce the error, as seen in Figure 22. The error test in the X-Y plane showed the average error of less than 10 μ m using both cameras, with a maximum error of 400 μ m.

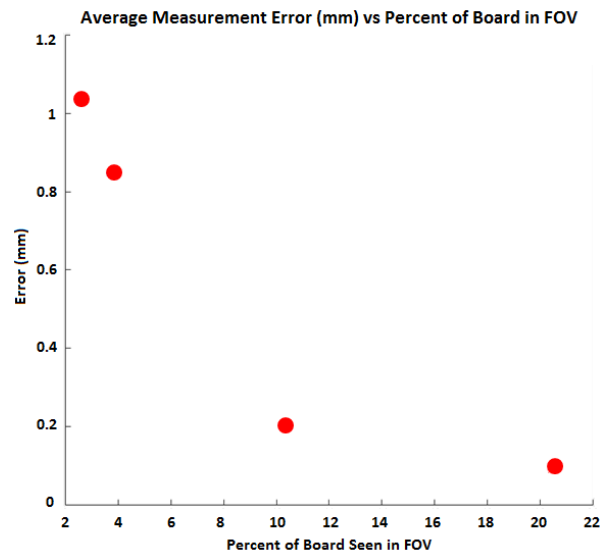


Figure 21. Percent of the field of view taken by the pattern board vs accuracy.

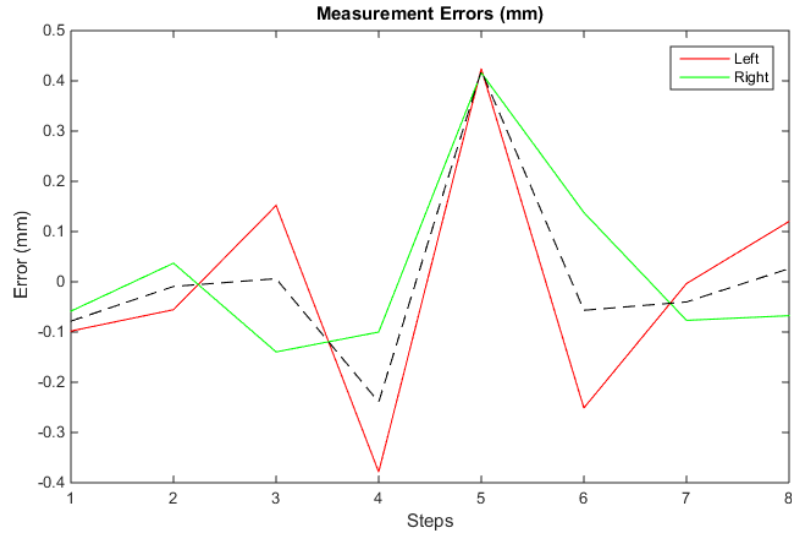


Figure 22. Two camera accuracy in the X-Y plane.

We also tested motion tracking accuracy using a continuous motion translation stages moving at 2.5mm/s. The camera frame rate was set to 1 fps and 20 images were taken and their geometry calculated. The plot of the average speed per step is recorded in Figure 23.

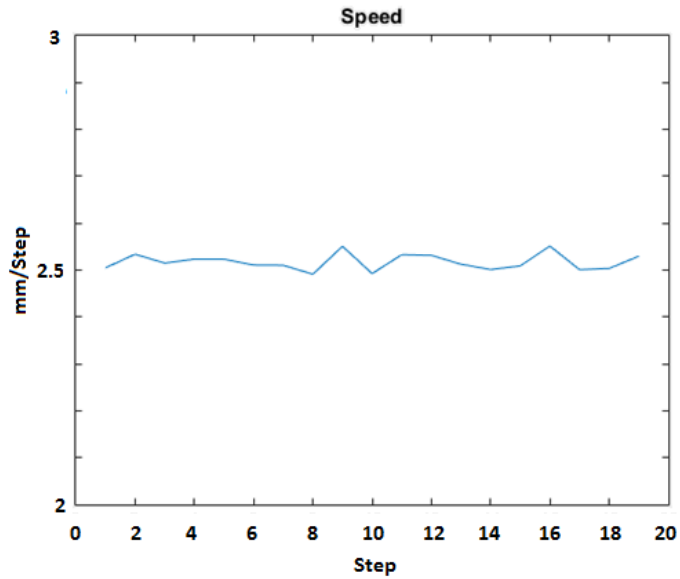


Figure 23. Speed graph during horizontal motion tracking on a 2.5mm/s translation stage showing the average calculated speed.

Figure 25 shows various slices of the geometry calibration phantom reconstructions using source position data obtained from X-ray projections (top) and from the optical geometry calculations. Figure 26 shows the horizontal and vertical plot profiles of the wire from both reconstructions. The horizontal slice has a thickness of $604\mu\text{m}$ vs the actual $635\mu\text{m}$ – a 4.9% error for both reconstructions. The vertical profile thicknesses were $566\mu\text{m}$ and $547\mu\text{m}$ for the calibration phantom and optical respectively – 10.8% and 13.9% errors from the actual width and a 3.4% error between the two methods.

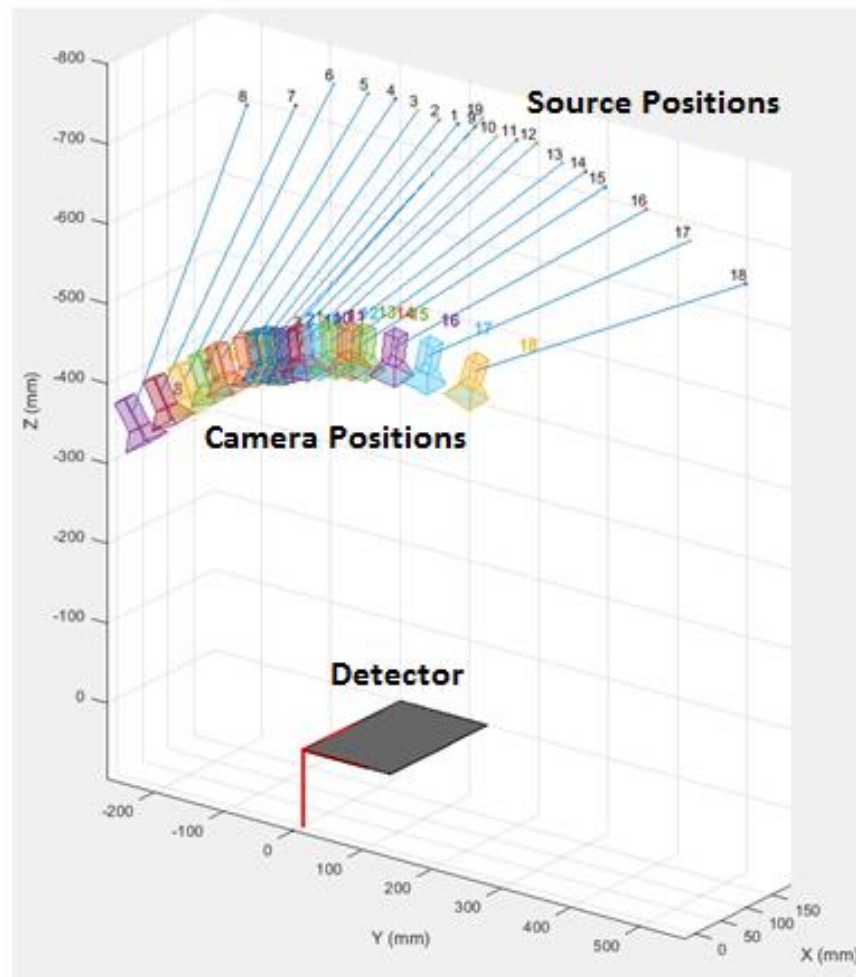


Figure 24. 3D representation of the camera and source positions (numbered dots) relative to the detector. The source and camera were positioned by hand about the detector and are not meant to follow a perfect arc.

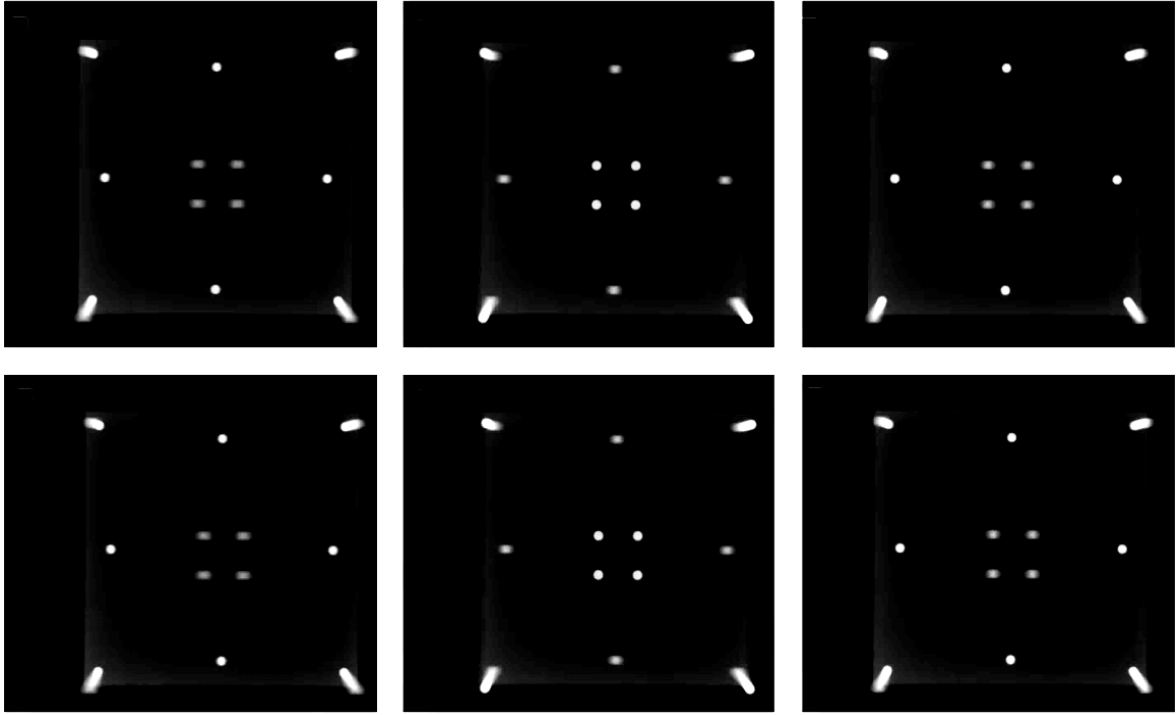


Figure 25. Slices 7, 20, and 63 using the geometry phantom source position data (top) compared to the optically calculated source positions (bottom) showing the wire and different beads in focus.

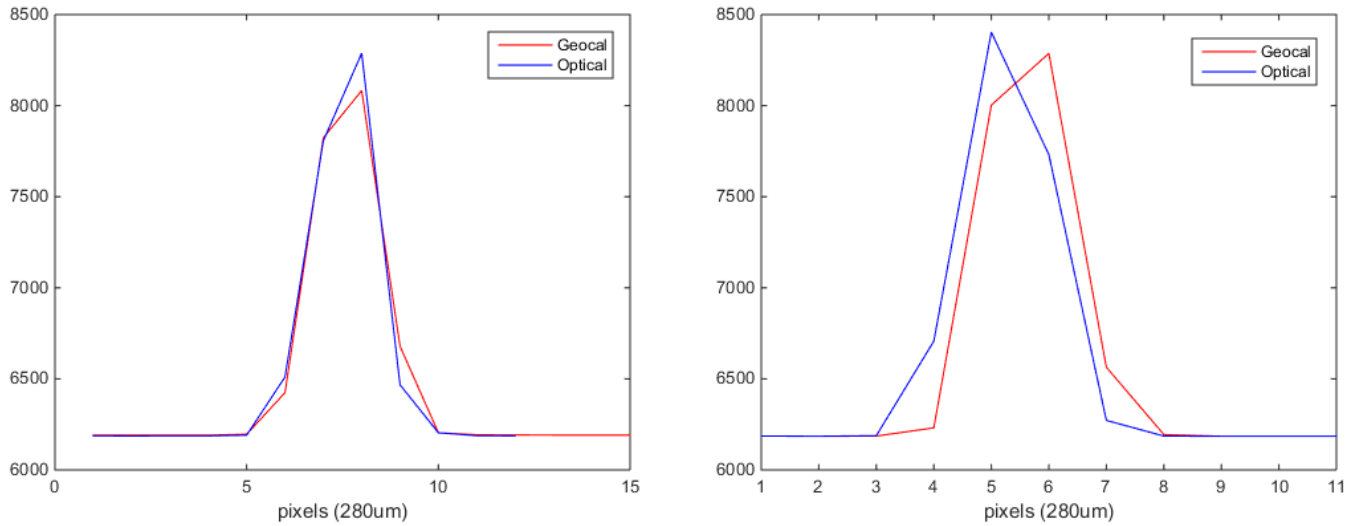


Figure 26. Horizontal and vertical profiles of the optically reconstructed bar in the phantom images
635 μm

3.4 Blank Image Library

To appropriately reconstruct, the projection images need to be corrected according to the formula:

$$\text{Corrected Image} = \frac{\text{Raw} - \text{Dark}}{\text{Blank} - \text{Dark}}$$

The dark image is an image taken with no X-ray to reduce the detector noise inherent to it. The blank image is taken at the same detector and source position as the raw but without the object. The raw image is the original image of the object obtained from the detector with no processing. This correction removes the non-uniform X-ray field caused by the source's heel effect and detector orientation. In the standard case of a repeatable trajectory, this is a simple task. In the case of a manually positioned source and detector, one cannot take exact blanks before the object.

To solve this, we have a Blank Image Library (BIL). This is a large dataset of blank images taken at a variety of detector projection angles and source to detector distances. The size is dependent on the possible angle and distance ranges of the tomo sets. After a tomo set, a program picks the closest blank image to correct with by the position of the source to the detector. Using this and making the library very large, the blank correction problem can be solved. Even though the BIL seems to be independent of the camera, it is still highly coupled with the source to camera position. Blank images are dependent on the source orientation as well as position. Though the source is modeled as an individual point, it still has its own coordinate system due to the heel effect of the X-ray source which is direction dependent.

3.5 Reconstruction

The images were reconstructed using commercial filtered back projection software that allows for any source geometry to be input. Hand and foot phantoms were imaged through a manually positioned source, following the pattern seen above. Figure 7 shows the comparison between our stationary tomosynthesis device (left) and the reconstructions from the manual tomo (using a calibration phantom for source positioning in the middle and using our optically determined geometry on the right).



Figure 27. Five slices through a foot from free tomo acquisition (source was manually moved to 11 positions across an $\sim 15^\circ$ arc)

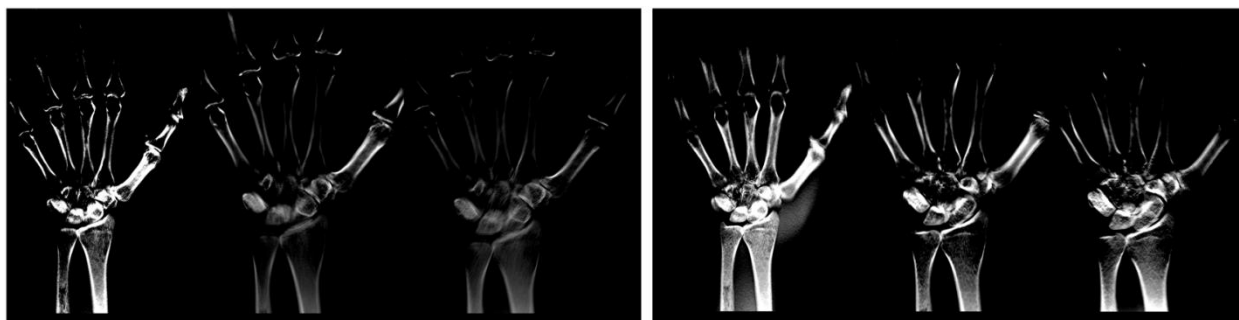


Figure 28. Sets of 3 images from 2 depths of reconstruction tomo sets of a hand. First image in each set was taken by the stationary chest tomo, second was on the free tomo setup using the geometry phantom to calculate the source position and the third was using the optical calibration geometry

3.6 Matlab Implementation

To perform the free tomo acquisition, processing, and reconstruction on RTT, several key programs and files are needed:

- webcam.m: Found installed with the appropriate webcam drivers on the Applied Nanotechnology group laptop (C:\Users\User\Documents\MATLAB). If installing on another system, the line: `handles.vid = videoinput('winvideo',2,'RGB24_1920x1080');` should be changed to the appropriate input channel, usually 1 if no other camera drivers are installed (such as a laptop webcam). This opens a GUI that allows the operator to take the images, check to make sure they are of good quality with a zoom ROI feature, retake if necessary, and save into the appropriate folder. Make sure to add the “\” at the end of the folder name. The images are saved numerically. Take an image and save it before every X-ray projection. A screenshot of the GUI is shown in Figure 29.
- geometry.m: File that finds the source to detector geometry using the bead phantom. To speed up the acquisition, the calibration is performed using a subset of the actual data set. The bead geometry phantom is secured to the detector for all or part of the data collection for this reason and also to use as a comparison. Use the images with a good view of the bead phantom to get the geometry to use in the calibration procedure. Returns `geo.mat` matrix that contains the course data. Check to make sure the values are not (0,0,0). If they are, that means not all of the points were found. Edit the thresholds on line: `imfindcircles(image(1:range,1:2560),[10 25], 'ObjectPolarity','dark','Sensitivity',0.8,'EdgeThreshold',0.03);` OR edits the range parameters ‘p’ added there to help separate the geocal from the actual object. Images 1-10 the geocal is in

a certain range but in 11, the object enters that range so from 11-something else, edit the new range to not include the object. Repeat as necessary.

- cameraCalibration DATA SET NAME.m: Partially auto-generated by cameraCalibrator app. Can be used as a reference to create new ones for each image set. The initial calibration file can be generated from the Camera Calibrator App in Matlab. A screenshot of it is shown below in Figure 30. I recommend creating a new file for each set to keep track of them easier and if necessary modify to fit new conditions, such as: cameraCalibration_1_1_2015_XPhantom.m. This file is the calibration script for the camera to the source and should, later on, be only used once, but since the camera is added for every new experiment and removed, the calibration must be run for every new data set. Use at least 20 images to get a good calibration – both of the camera intrinsic parameters and the geometry. The file consists of: imageFileNames – an array of the optical images ONLY used for the recon – not the entire set. $offX=183.48-355.84/2$; $offY=24.05-427.01/2$; are the pattern offsets relative to the detector found using the beads as described and illustrated in Figure 20. `[poss, poss2, trans, source]=showExtrinsicsDATA_SET_NAME_CALIB (cameraParams, rawX, rawY, rawZ, offX, offY, 'PatternCentric');` calls the calibration file. rawX/Y/Z are arrays of the source positions obtained from geo.met. The file calculates avgX/Y/Z which is the so called CS vector described in the math position in Chapter 2. This is the vector from the camera to the source in the camera coordinate system. Further transformation from CC to DC puts in back into the detector space. The rest of the files plots the data, the vectors, and shows the predicted vs “actual” values from the geo phantom. It is worth checking to make sure the error is low and there are no outliers ruining the calibration data.

- showExtrinsicsDATA SET NAME CALIB.m: File that calibrates the camera and detector. Takes in the parameters described above and returns: poss – camera position coordinates, poss2 – camera rotation matrix, trans – camera translation matrix, and source – the source positions relative to the detector. The output is shown in Figure 31.
- processDATA SET NAME.m: File similar to cameraCalibration.m with the imageFileNames array but without the calibration aspect. The file lists the offsets and the calculated avgX/Y/Z (or assumes that they are loaded into memory from the previous calibration calls. Calls [poss,poss2,trans,source]=
showExtrinsics_DATA_SET_NAME(cameraParams, 'PatternCentric'); to get the source positions for the tomo scan.
- showExtrinsics DATA SET NAME.m: Much like the extrinsics file above but in this case takes the CS vector input and outputs the calculated source positions.
- tags.m: File that writes the dicom headers needed for RTT and adds the source position data. If not run from my computer, be sure to change the location of dicomdict('set','C:\Users\PavelC\Documents\MATLAB\dicom-dict.txt'); This file should be in the same folder as the X-ray images. Some older versions of the file may have for i=1:27 that counts the files in the folder. Change to the appropriate number of X-rays. The line info_new.UNC_Source_Position = [procX(i),procY(i), procZ(i)]; is what adds the source positions in to each header. Make sure the source positions are in the procX/Y/Z arrays. Assuming the code from the previous file is correct this should not be an issue.
- DitkaSettings.txt: This MUST be in the folder of the X-ray images that are loaded into RTT. Any folder with recon images will have this file. Do not change anything

about this file, just be sure it's included. If you ever get an error from RTT, the first thing to do is check if this file is present.

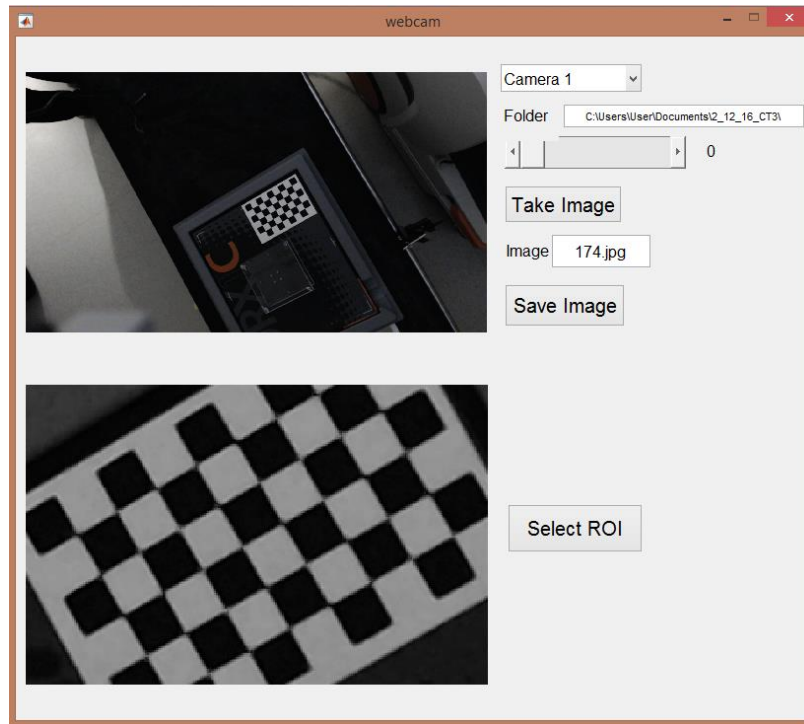


Figure 29. Webcam acquisition GUI

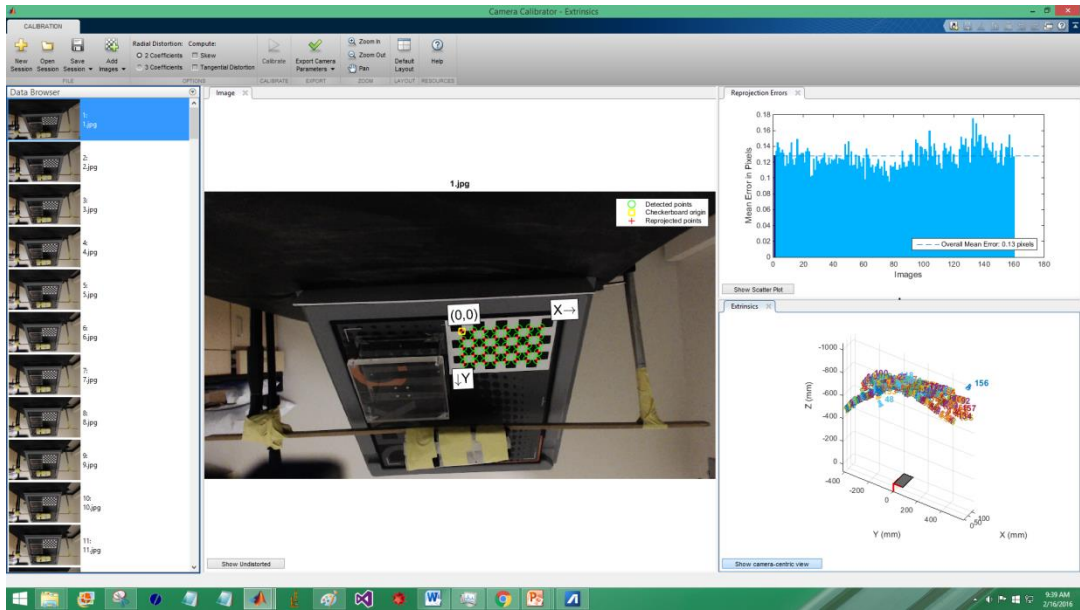


Figure 30. Screenshot of the Camera Calibrator App in Matlab loaded with a tomosynthesis image set.

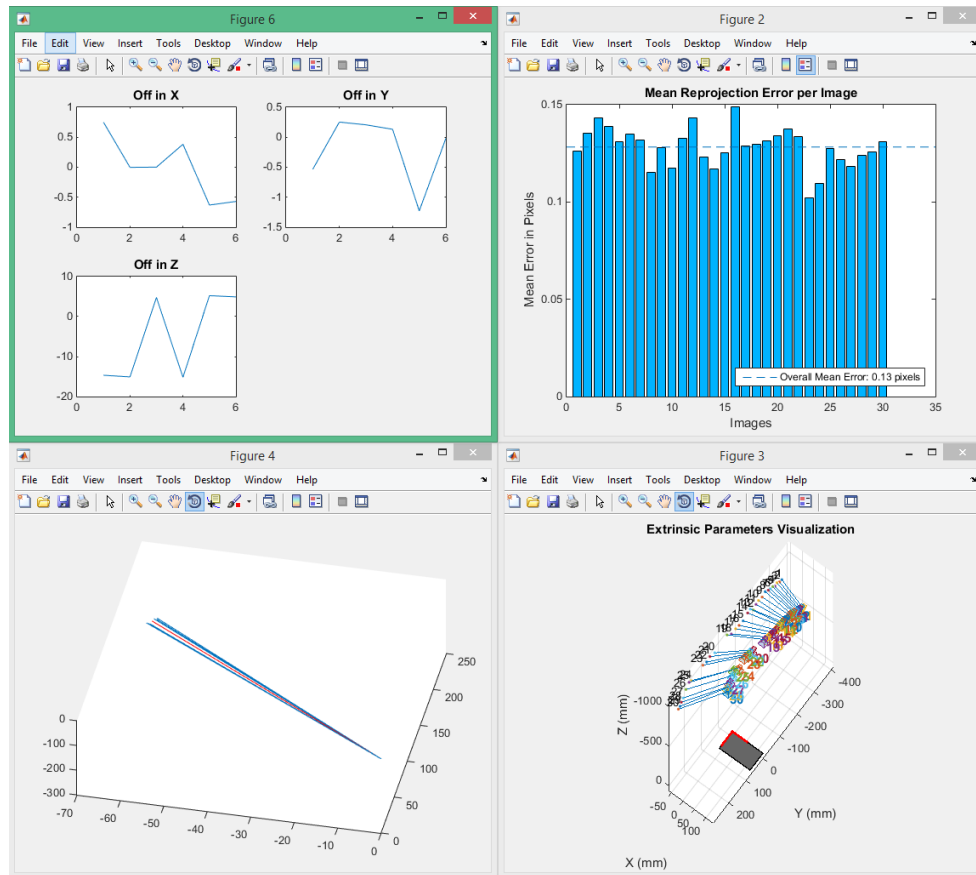


Figure 31. Output of the showExtrinsicsDATA_SET_NAME_CALIB.m file. The “error” from the predicted value to the “actual” value of the geocal phantom, the calibration pixel error, the vectors

averages to show the CS vector, and the camera and source positions plotted relative to the optical pattern.

CHAPTER 4: INTRAORAL TOMOSYNTHESIS

4.1 Motivation

As in many areas of medicine, X-ray imaging is an incredibly useful tool in diagnosis. In dentistry, the addition of panoramic imaging and cone beam CT (CBCT) has improved the visualization of the maxillofacial regions though has not been shown to improve the detection of caries due to its low spatial resolution and image artifacts resulting from beam hardening from the teeth. This is problematic as it results in both false negatives and positives¹¹.

The most commonly used intraoral imaging method for the detection of proximal caries lesions is the bitewing. Though a common procedure, its diagnostic accuracy is surprisingly low. The median sensitivity and specificity for radiographic occlusal caries detection is 27% and 95%, respectively. For proximal caries, the median values were only 49% and 88%¹¹. The need for a high accuracy and low dose intraoral imaging system remains.

A collaboration between the School of Dentistry and Xintek Inc is in the process of developing a spatially distributed source array for 3D intraoral imaging. Initial studies show improved detection of dental pathology such as caries, root fractures, and alveolar defects and fewer image angulation errors as compared to standard intraoral imaging. The system also provides high resolution dental and alveolar anatomy with a dose similar to the standard bitewing.

Unlike traditional tomosynthesis imaging systems described above that have a hard connecting source and detector that the free form tomo system decouples, the intraoral system is unique in that the detector is not even visible and is inside the patient's mouth. This makes image positioning and geometry calibration incredibly difficult. The goal is to use the optical geometry calibration method for use with intraoral imaging – both as a manual free form tomo and using spatially distributed sources for a stationary intraoral tomosynthesis.

4.2 Application

To use the method, the optical pattern must be visible to the webcam and thus be outside the patient's mouth. An option is to use the standard O-ring detector/bitewing holder as the pattern holder. In order to keep the system consistent with current dental imaging systems, a modified version of the O-ring holder was designed and is shown in Figure 32. A SuniRay 2 intraoral detector was used for the holder and the camera was similarly attached to the source head and the pattern to the detector. In the oral case, the pattern is off the detector plane as the detector is inside the mouth which, theoretically does not change the algorithm theory but practically adds additional concerns of motion between the two.

The next large concern is calibration. . The pattern position can be calibrated to the detector using the same bead principle used in the previous tomo case. A bead is placed at the origin of the pattern and a larger and high attenuating bead is placed on the intraoral detector. This is then placed on a larger detector along with a geometry phantom and imaged. The two beads can be reconstructed to give a relative position between them. The bead on the intraoral detector is then imaged on itself and given an absolute position in the

intraoral detector space. From that, the origin of the optical pattern can be determined relative to the intraoral detector.

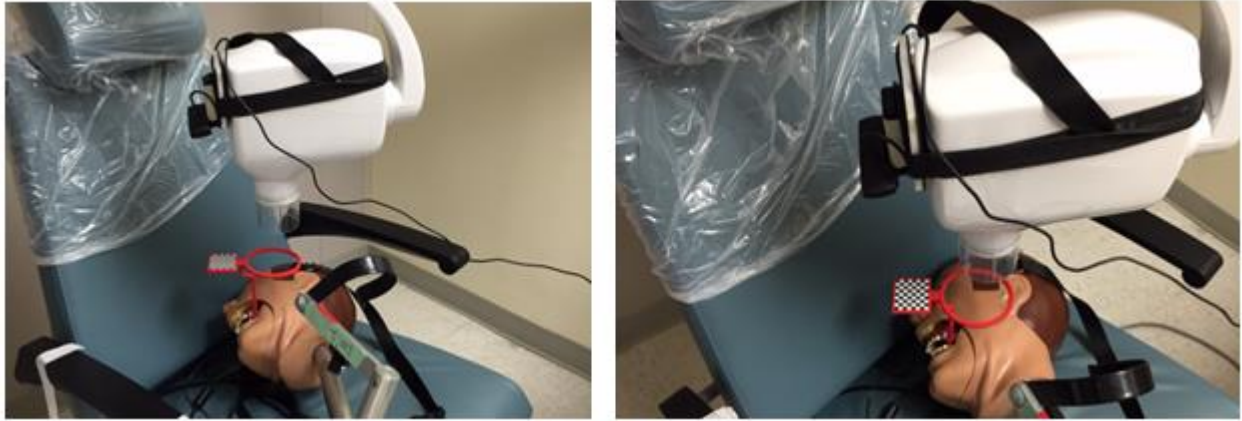


Figure 32. Oral tomosynthesis setup using a custom made holder with the checkerboard pattern and with the optical camera attached on the X-ray housing.

As the detector is so small, the standard bead phantom cannot be used as a calibration method. The reason is illustrated below. The detector has a pixel size of $33\mu\text{m}$ and a reasonable phantom thickness is about 12mm. Setting that as the minimum error and disregarding everything else, an SID of 600mm results in the source error of 1.6mm in X and Y. The error in Z that is usually an order of magnitude higher from previous FF tomo tests would then be about 16mm. This is not including any other errors in imaging including positioning, bending of the rod connecting the optical pattern to the detector, and other traditional imaging errors such as motion.

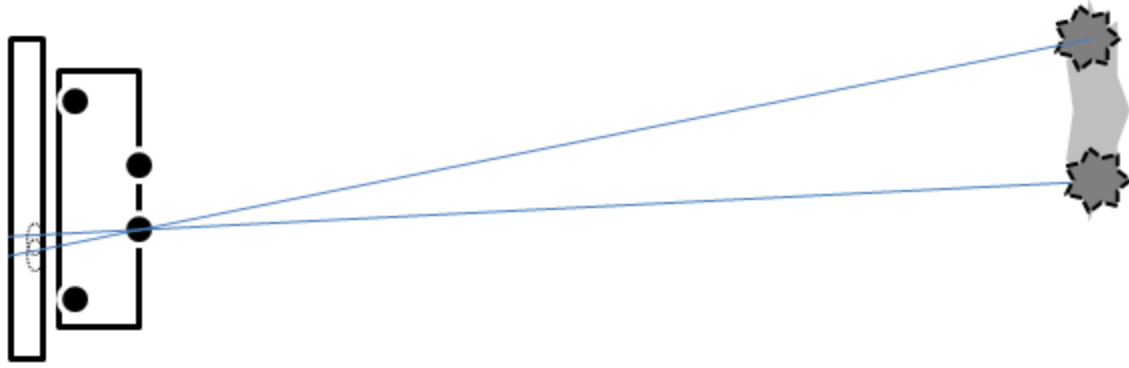


Figure 33. Illustration of bead phantom calibration problem with a small detector relative to the source to detector distance. The detector pixel size of $33\mu\text{m}$ creates an uncertainty shown on the left that results in a much larger 1.6mm source uncertainty shown on the right.

Since the source to camera calibration is independent of the detector and pattern, the ideal way to accomplish this would be to calibrate on a large detector using a larger geometry phantom. Then, assuming the camera is fastened permanently or is not moved prior to intraoral imaging, the setup can be used for that and any other detector or imaging system.



Figure 34. Camera attached to dental X-ray unit and imaging a dental phantom with the custom made detector and pattern holder.

4.4 Future Development

We unfortunately did not have a large detector that we could trigger to accomplish this calibration but the initial testing has been performed with a small phantom with low resolution. The method of manual free form intraoral tomosynthesis has been shown to be feasible and easy due to the maneuverability of the dental X-ray arm. The SuniRay 2 and other small intraoral detectors can be outfitted with the pattern detector holder for future experimentation in the different geometries and angular coverages of intraoral imaging to create new and never-before-seen oral 3D reconstructions.

CHAPTER 5: FREE FORM COMPUTED TOMOGRAPHY

5.1 Motivation

There is currently no convenient way to obtain CT images of an object remotely in the field. CT provides valuable three dimensional images of the internal structure of an object, removing overlapping, and providing better diagnosis comparing to 2D transmission image. Unlike a CT, where the positions of the detector and the source are known in the world coordinate system that the body is in, our current method only lives in one detector coordinate system. To obtain more than about a 45° angular coverage, the detector must be moved. The goal is to move the detector about the body in the same fashion as a CT and take image projections for each detector position and be able to ‘stitch’ them all back into one coordinate system. An additional logical and useful step from this would be remote CT acquisition. A remotely controlled CT scanner that can image an object without being physically transported to the object by the operator would be highly desirable in situations of imaging dangerous or hard to reach objects.

5.2 Imaging

The process can be summarized in the flowchart below. The procedure for each detector position is the same as for the free form tomosynthesis method. The only addition is the extra image taken during the transition when the source is stationary and the detector moves. There is no clinical need to take an X-ray projection image during this step and it most likely will not even be on target and provide any valuable data, but for phantom imaging it is helpful to nevertheless still take that extra image for consistency reasons. The image sets are over 100 images, some in the 130s, so having the same number of optical

images as X-rays makes the reconstruction process a lot easier when each of the images matches up.

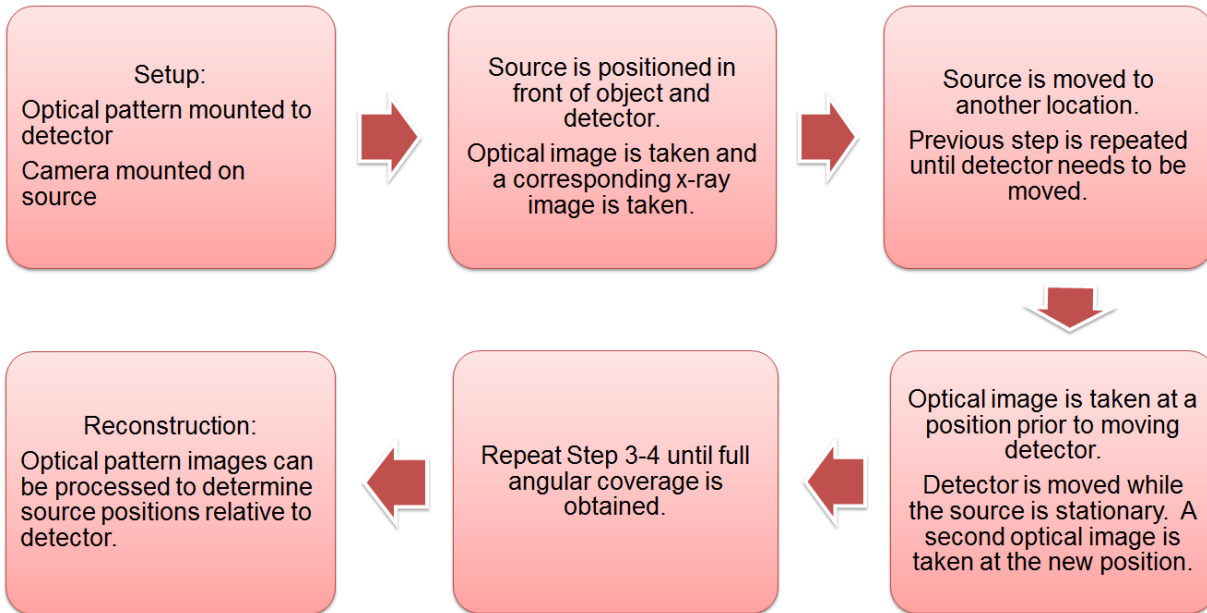


Figure 35. Flowchart showing the imaging cycle of the free form tomo imaging.

The DRX was used for the free form CT imaging. To make a true CT recon, we were aiming for a 180° acquisition angle which was possible to accomplish with the DRX's maneuverable head. Unlike the free form tomo, the object does not move with the detector and must be elevated. The best way we found to do that was using a low attenuating rod to hold the object above the detector and attached to the bed which is stationary. The source and detector are then free to move about the object. The CT was completed in three detector positions. This is shown in Figure 36 below. The detector is set up to cover 60° of motion from the source. At C, the last image is taken and the source is held stationary while the detector is repositioned to be flat. The imaging continues as with the normal free

form tomo method until the edge is again reached at D, when the detector motion process is repeated. The images that document to the move are noted and later added to the algorithm during reconstruction.

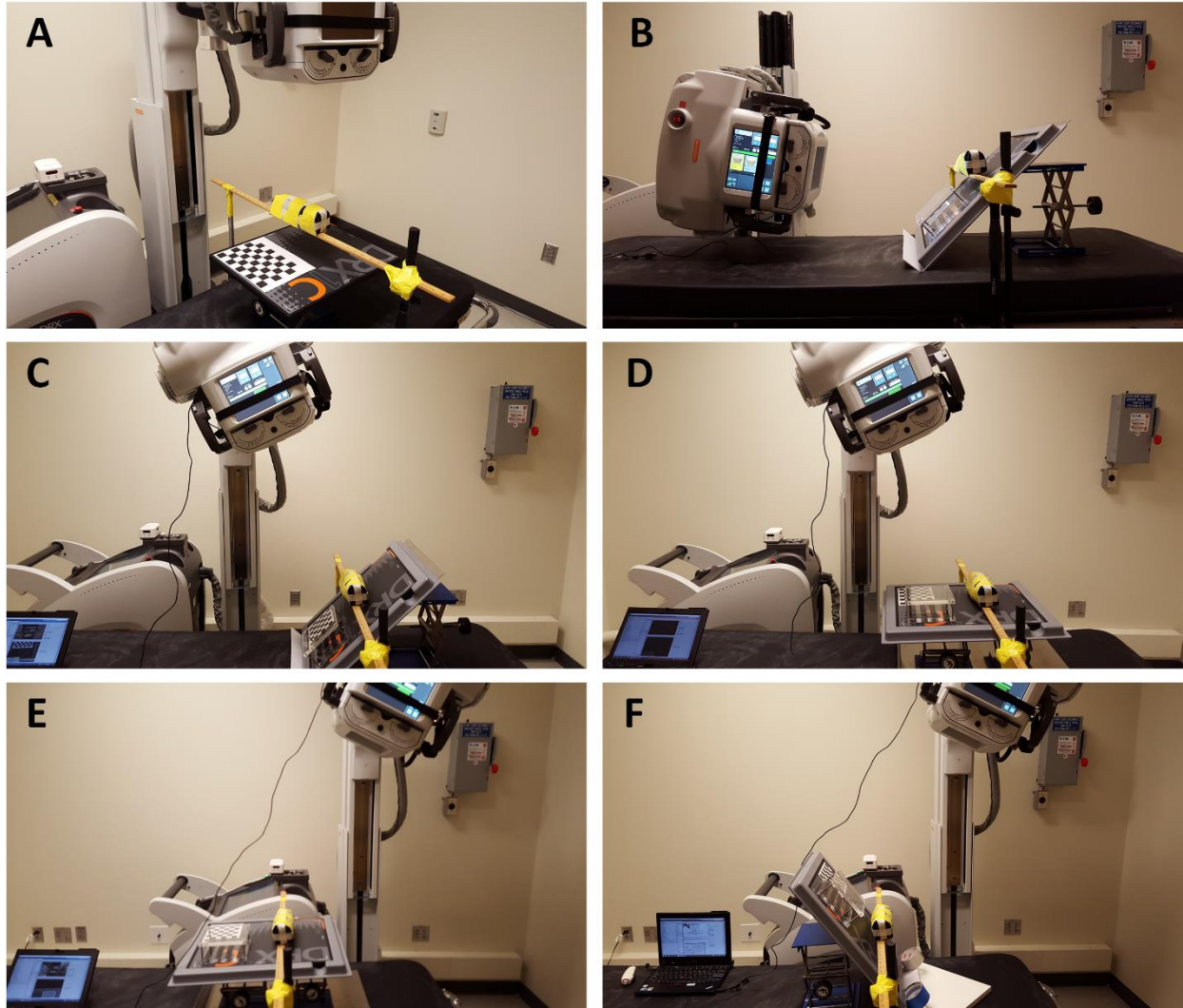


Figure 36. A) Free form CT imaging setup with the object rigidly attached to not move during the process to a low attenuating rod (meter stick). B) Imaging begins at the left side. C) Reaching the limit of this detector position. D) Source is stationary, the detector is moved to preserve the coordinate system. E) Imaging continues to the right-most side with the detector flat. F) Source is stationary, the detector is moved once again and the imaging can continue to the right side.

5.3 Matlab Implementation

The feasibility of the algorithm's ability to optically reconstruct the positions was first tested on a literal desktop method with a webcam and pattern. This allowed for a controlled movement of the camera and pattern to confirm the recon. This is shown later in Figure 37 with the maroon vector of the camera coordinate system being the Z axis – the axis perpendicular to the camera lens. The rectangles are the optical pattern positions.

The reconstruction is done using the files discussed in section 3.6 Matlab Implementation with some slight modifications. For ease of use, here are the files again with the modifications noted:

- webcam.m: Found installed with the appropriate webcam drivers on the Applied Nanotechnology group laptop (C:\Users\User\Documents\MATLAB). If installing on another system, the line: `handles.vid = videoinput('winvideo', 2, 'RGB24_1920x1080');` should be changed to the appropriate input channel, usually 1 if no other camera drivers are installed (such as a laptop webcam). This opens a GUI that allows the operator to take the images, check to make sure they are of good quality with a zoom ROI feature, retake if necessary, and save into the appropriate folder. Make sure to add the “\” at the end of the folder name. The images are saved numerically. Take an image and save it before every X-ray projection. A screenshot of the GUI is shown in Figure 29.
- geometry.m: File that finds the source to detector geometry using the bead phantom. To speed up the acquisition, the calibration is performed using a subset of the actual data set. The bead geometry phantom is secured to the detector for all or part of the data collection for this reason and also to use as a comparison. Use the images with a good view of the bead phantom to get the geometry to use in the calibration

procedure. Returns geo.mat matrix that contains the course data. Check to make sure the values are not (0,0,0). If they are, that means not all of the points were found. Edit the thresholds on line: `imfindcircles(image(l:range,l:2560),[10 25], 'ObjectPolarity','dark','Sensitivity',0.8,'EdgeThreshold',0.03)`; OR edits the range parameters 'p' added there to help separate the geocal from the actual object. Images 1-10 the geocal is in a certain range but in 11, the object enters that range so from 11-something else, edit the new range to not include the object. Repeat as necessary.

- cameraCalibration DATA SET NAME.m: Partially auto-generated by cameraCalibrator app. Can be used as a reference to create new ones for each image set. The initial calibration file can be generated from the Camera Calibrator App in Matlab. A screenshot of it is shown below in Figure 30. I recommend creating a new file for each set to keep track of them easier and if necessary modify to fit new conditions, such as: `cameraCalibration_1_1_2015_XPhantom.m`. This file is the calibration script for the camera to the source and should, later on, be only used once, but since the camera is added for every new experiment and removed, the calibration must be run for every new data set. Use at least 20 images to get a good calibration – both of the camera intrinsic parameters and the geometry. The file consists of: `imageFileNames` – an array of the optical images ONLY used for the recon – not the entire set. `offX=183.48-355.84/2`; `offY=24.05-427.01/2`; are the pattern offsets relative to the detector found using the beads as described and illustrated in Figure 20. The offset is determined by the position (in mm) of the point (in the example above 183.48mm in X and 24.05mm in Y and subtracted from the width and height of the detector. `[poss, poss2, trans, source]=showExtrinsicsDATA_SET_NAME_CALIB(cameraParams, rawX, rawY, rawZ, offX, offY, 'PatternCentric')`; calls the calibration file. `rawX/Y/Z` are arrays of the source

positions obtained from geo.met. The file calculates avgX/Y/Z which is the so called CS vector described in the math position in Chapter 2. This is the vector from the camera to the source in the camera coordinate system. Further transformation from CC to DC puts in back into the detector space. The rest of the files plots the data, the vectors, and shows the predicted vs “actual” values from the geo phantom. It is worth checking to make sure the error is low and there are no outliers ruining the calibration data.

- showExtrinsicsDATA SET NAME CALIB.m: File that calibrates the camera and detector. Takes in the parameters described above and returns: poss – camera position coordinates, poss2 – camera rotation matrix, trans – camera translation matrix, and source – the source positions relative to the detector.
- processDATA SET NAME.m: File similar to cameraCalibration.m with the imageFileNames array but without the calibration aspect. The file lists the offsets and the calculated avgX/Y/Z (or assumes that they are loaded into memory from the previous calibration calls. There is also a steps array which signifies the steps when the detector is moved. For example, if positions 2 and 3 and 8 and 10 are the same (detector was moved between 2 and 3 and 8 and 10 and the camera was stationary during those two in WC, the list is [2, 8]). Calls [poss, poss2, trans, source, sourcePositions, detectorCenters, detectorNormal]=showExtrinsics_DATA_SET_NAME(cameraParams, steps, width, height, avgX, avgY, avgZ, offX, offY, 'PatternCentric'); to process the full CT source positions.
- showExtrinsicsCT DATA SET NAME.m: Like the showExtrinsics files from FF tomo but also takes into account the detector motion. Returns (in addition to the original function) sourcePositions – 3 coordinate positions of the sources, detectorCenters – coordinates of the centers of the detectors, and detectorNormal –

normal vectors of the detectors. These 3 arrays are necessary for the free form CT reconstruction algorithm provided by Dr. Lalush.

- showExtrinsicsCT DATA SET NAME SetX.m: same as the `showExtrinsics_DATA_SET_NAME.m` file from free form tomo. Used to get tomo recons of each set of data from individual detector positions while waiting for CT recon to confirm viability of data. Called by `processDATA_SET_NAME_SETX.m`.
- tags.m: File that writes the dicom headers needed for RTT and adds the source position data. If not run from my computer, be sure to change the location of `dicomdict('set','C:\Users\PavelC\Documents\MATLAB\dicom-dict.txt');` This file should be in the same folder as the X-ray images. Some older versions of the file may have `for i=1:27` that counts the files in the folder. Change to the appropriate number of X-rays. The line `info_new.UNC_Source_Position = [procX(i),procY(i),procZ(i)];` is what adds the source positions in to each header. Make sure the source positions are in the `procX/Y/Z` arrays. Assuming the code from the previous file is correct this should not be an issue.
- DitkaSettings.txt: This MUST be in the folder of the X-ray images that are loaded into RTT. Any folder with recon images will have this file. Do not change anything about this file, just be sure it's included. If you ever get an error from RTT, the first thing to do is check if this file is present.

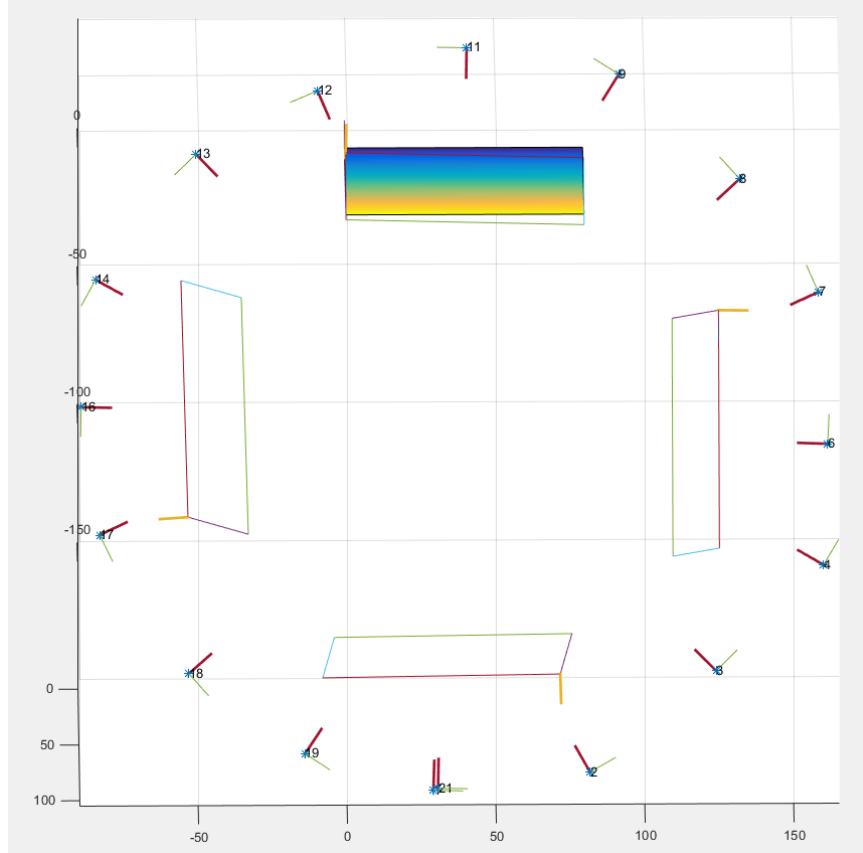


Figure 37. Reconstructed patterns and camera coordinate systems of a desktop proof of concept to show the program working. The rainbow colored rectangle is the starting pattern position.

5.4 Experimental Validation

The experiment to show the proof of concept of the large angle tomosynthesis with a moving detector was done using the same DRX imaging setup as with the previous free-form tomo. A security phantom consisting of a circuit board, pocket knife, water bottle, and two pens inside of a bag was used as the object. The bag was hoisted and taped in place above the imaging bed as shown in Figure 36 and the detector was rotated below it with the source head moving about it in a circular path. The images were taken as with the previous experiment and the detector motion images while keeping the source/camera stationary were taken and their numbers noted for the reconstruction.

The CT data set was performed with 4 detector positions. Only three were needed but in the middle of the last set, the battery needed to be recharged so the detector was moved and placed back in the same orientation but as seen from the recon in Figure 38, the difference is noticeable and needed to be recorded. The free form CT algorithm was then used to put the four tomo sets in the same coordinate system. The setup with the four detector positions and the camera and source positions is shown in Figure 38 below. The sets total to a little over 180° angular coverages and include 130 projection images.

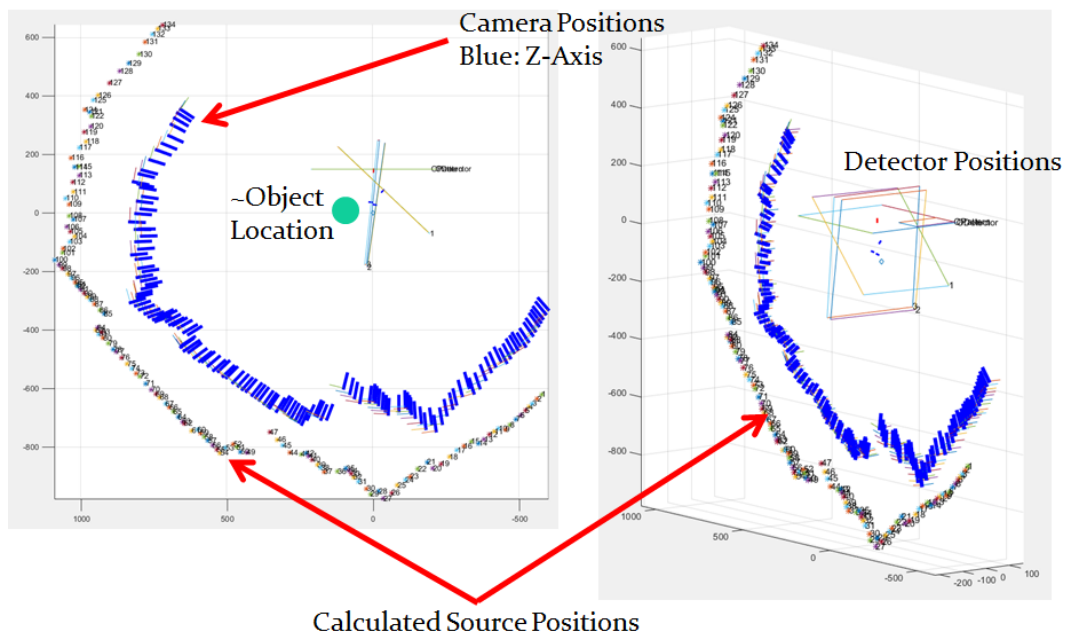


Figure 38. Reconstructed camera and source positions on a CT data set. The dark blue lines are the z-axes of the camera (pointing directly out perpendicular to the lens) and the asterisks are the calculated source positions.

At the time of writing this, there is no working CT reconstruction algorithm so the analysis will be performed on the separate tomo data sets for each detector position. Figure 39 shows the top and the side projection views of the security phantom. The positioning of the items can be seen, with the circuit board and the knife on its side on the bottom, the bottle on top, one of the pens on the side of the bottle, and the other on top.

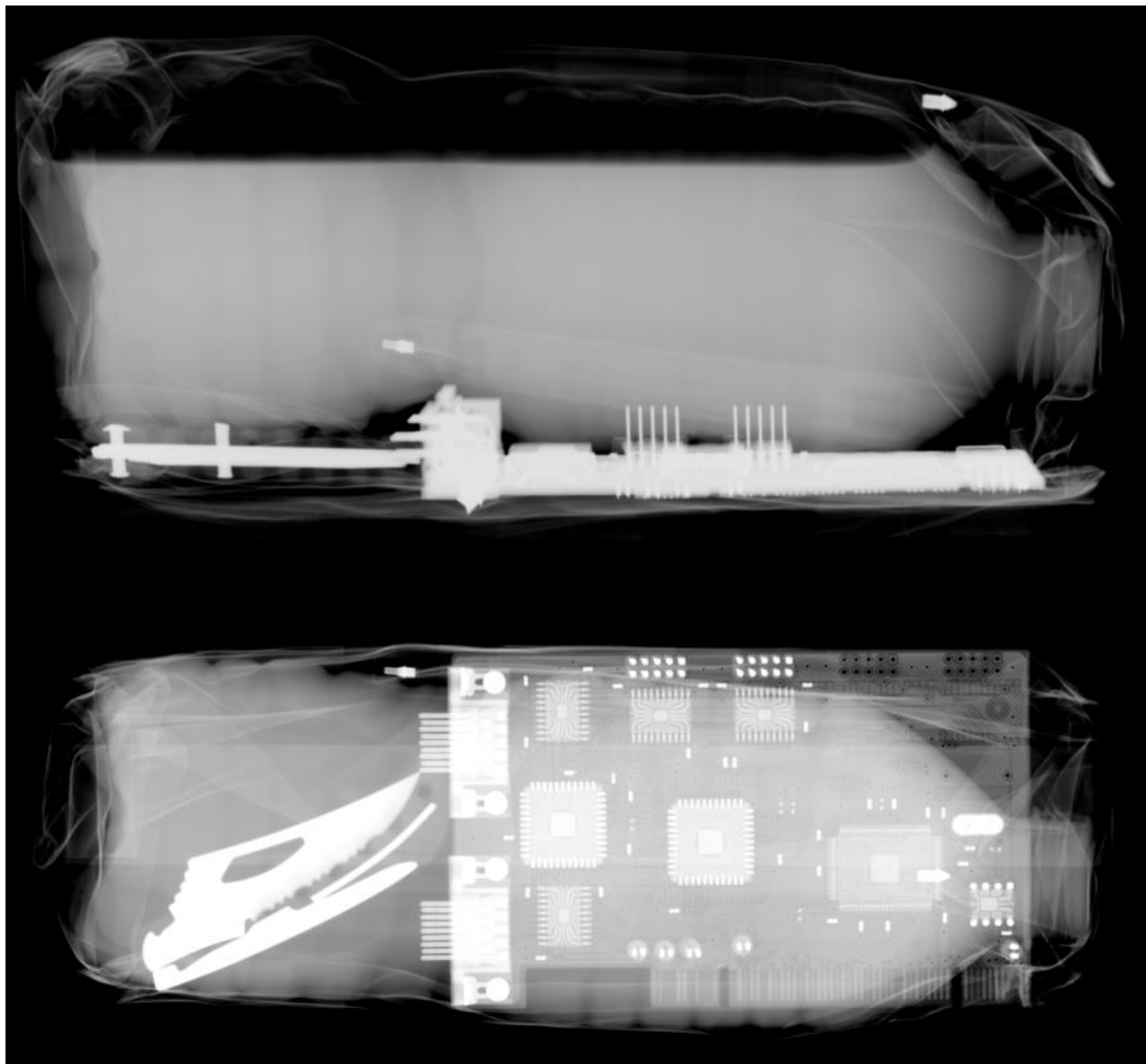


Figure 39. Side and top projection views of the security phantom.

The reconstructions should in theory provide this 3D information through the slices. Looking at one of the projection images in Figure 40, the serial pins are compacted together with no information in the out-of-page direction.

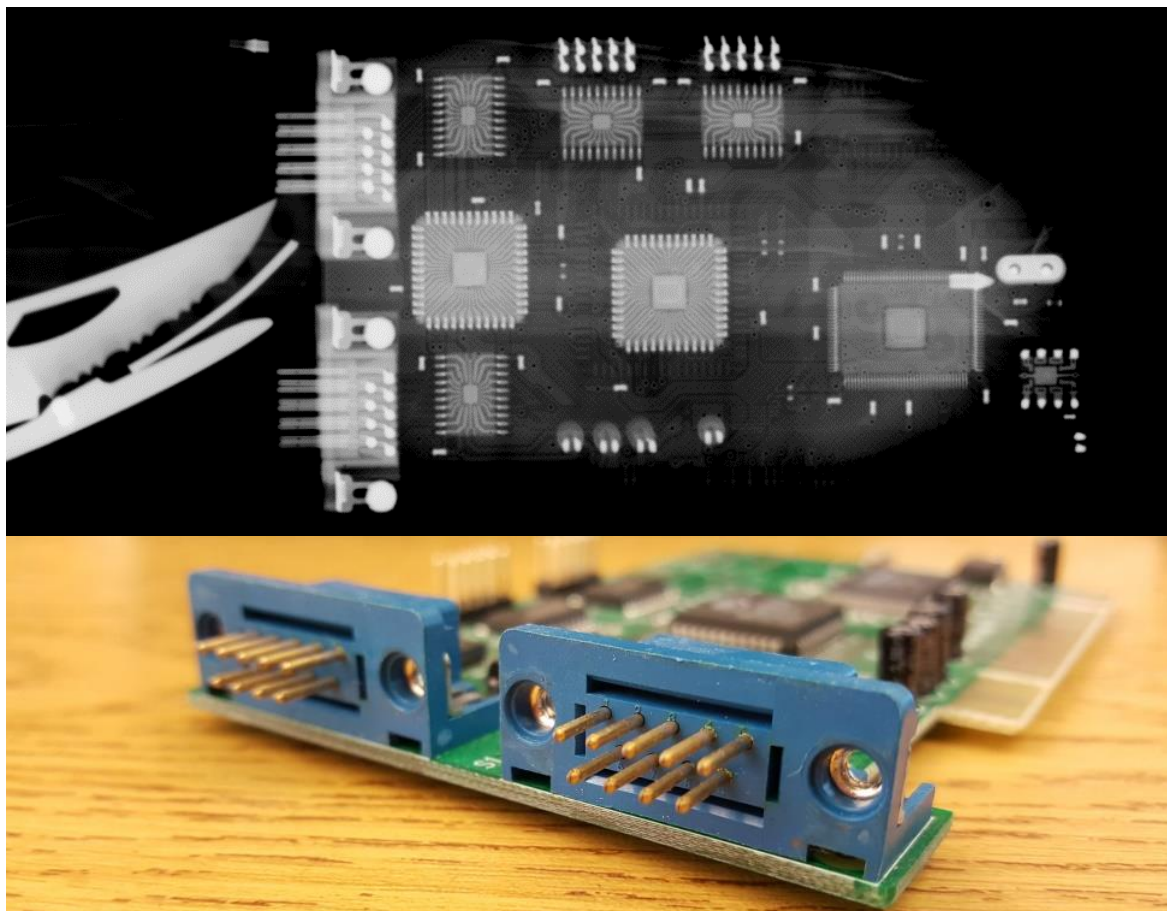


Figure 40. Top: Projection image of the circuit board showing no depth information regarding the serial pins on the left. Bottom: Photo of the serial pins.

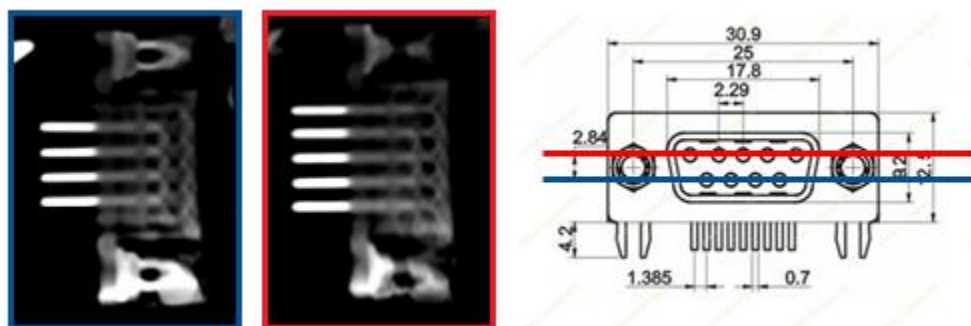
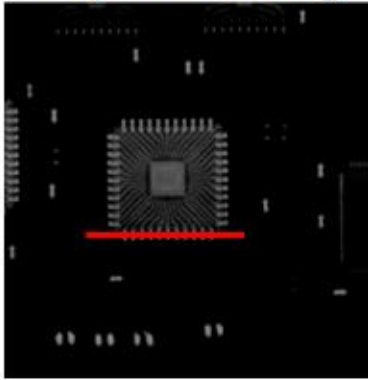


Figure 41. Slices 3 and 17 (at 0.2mm slice thickness) focusing on the top and bottom pins of the serial connection. The slice separation is 2.8mm (at the 0.2mm resolution) indicating the same separation between the top and bottom rows. The datasheet on the right shows the actual distance to be 2.84mm.

Figure 41 shows two slices of the reconstruction (3 and 17 at 0.2mm slice thickness) focusing on the top and bottom pins of the serial connection. The slice separation is 2.8mm (at the 0.2mm resolution) indicating the same separation between the top and bottom rows. The datasheet on the right shows the actual distance to be 2.84mm. A line profile analysis was also done on the chip pins, shown in Figure 42. The profile through the tomo reconstructed image has a much larger contrast, as expected, compared to the projection image. This is due to the removal of the attenuating layers above and below the chip pins, in the tomo layer, that reduce the contrast in the projection image.

Projection Image



Tomo Recon Slice

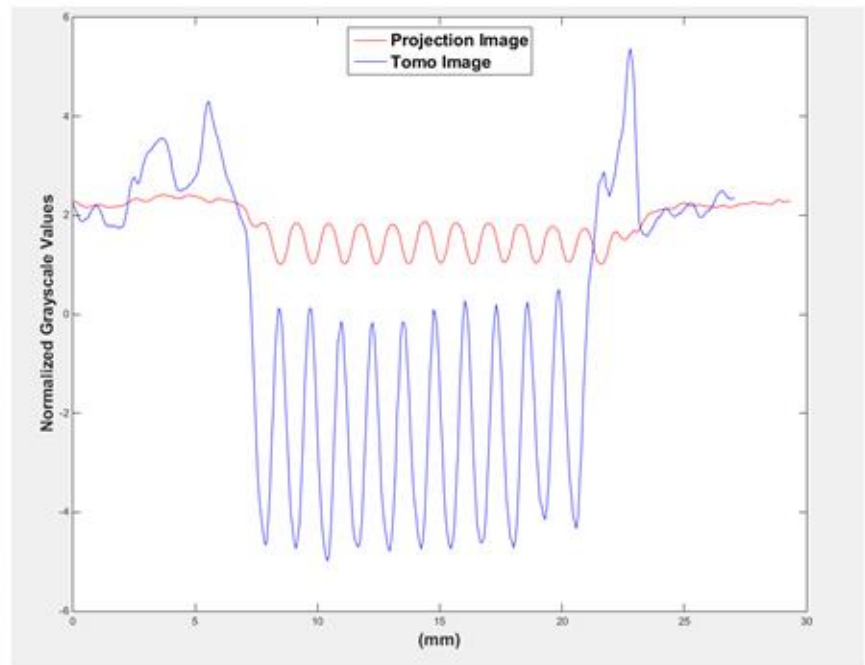
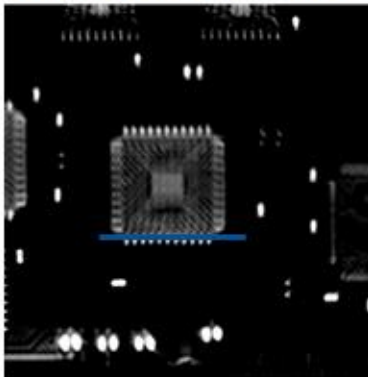


Figure 42. Line profile of the chip pins showing the expected increase in contrast in the tomo slice due to the removal of attenuating layers above and below in the projection image.

CHAPTER 6: CONCLUSION AND DISCUSSION

This study successfully showed the feasibility of a free form tomosynthesis system that is unrestricted by a physically connected detector and source. This opens the doors to portable 3D imaging using hand-held devices, the imaging of vastly different sized objects and immovable or dangerous containers. The error of the imaging system itself is very small – sub millimeter accuracy is easily obtained. The results are shown to be within a 3.5% deviation as the geometry phantom that we currently use in our tomosynthesis studies.

The largest error that we saw was due to the error inherent to the geometry calibration phantom. A better method to determine the location of the camera focal spot to the optical camera's focal spot is needed. This was our limiting factor but in a future study, the camera will be permanently mounted in a designated and well defined location that would decrease the uncertainty of the source to camera position. Without redesigning, however, this method also allows for any current X-ray system, using the calibration procedure, to become a free form tomography imaging system.

Some of the limitations of the current setup that need to be addressed are regarding the camera we used. We opted for an inexpensive webcam for the proof of concept but an improvement would be to use one with a smaller FOV which would allow for a smaller optical pattern and still fill in the minimum required 20% of the image. A better lens with a zoom feature would also improve the imaging conditions and accuracy.

This free form tomo has the ability to be used in a variety of previously impossible scenarios. The first is in a stationary intra-oral tomosynthesis system, which would obtain 3D images of the teeth using a stationary source array. In areas of the body that are less likely to move during imaging, such as extremities or the spine, our free form tomo device can provide 3D information of injuries ranging from military use out in the field to imaging in sport stadiums without moving the patient if a spinal injury is suspected. It would also allow for the imaging device to come to patients that are hard or impossible to move, such as burn victims.

The security phantom experiment and successful reconstruction shows the feasibility of the free form CT. The image set included 79 projections which were enough to produce a CT but more are necessary to reduce artifacts. The concern with the large number of projections is the feasibility of performing the imaging manually in a reasonable timeframe in a clinical or security setting. Reducing the number of projections can be accomplished by using a source array for each projection, such as the ones used in our stationary tomosynthesis scanners using array of X-ray sources spatially distributed in a fixed pattern. An array of 5 sources, for example, would still be portable but reduce the number of projections to just 16.

The future of free form tomosynthesis and CT has a lot of possible directions. As portable 2D imaging systems are readily available, the optical camera and pattern can be applied to upgrading these existing systems to perform 3D imaging – both for medical and security applications. As shown in Figure 18, portable and hand-held X-ray equipment is already a reality on the market. Some have even been attached to rovers for technician safety, such as the XSR from the First Responders Group in DC, shown in Figure 43.



Figure 43. X-ray Scanning Robot from the First Responders Group in DC.
<http://www.firstresponder.gov/TechnologyImages/X-Ray%20Scanning%20Rover/x%20ray%20rover.jpg>

The next steps would be to work on modifying these existing systems to support 3D imaging and also creating new 3D imaging systems that incorporate this optical image calibration technology.

APPENDIX 1: INTRODUCTION TO MICROBEAM RADIATION THERAPY

1.1 Glioblastoma Multiforme

Glioblastoma multiforme is the most common malignant tumor of the central nervous system and one of the most deadly cancers. Current treatments of surgery, chemotherapy, and radiation therapy only increase the median survival time from 12.1 to 14.6 months¹² and only 2.2% of patients survive past 3 years¹³. One of the main drugs for GBM is Temozolomide (TMZ), which was approved for second-line therapy. TMZ therapy has its pitfalls, however, with reduced tolerability and lowered blood count.

There are several reasons why treatment is so difficult. The tumor cells are very resistant to conventional radiation therapy methods and often occur deep in the brain tissue. The brain is also vulnerable to damage caused by the therapy, specifically RT. Modern imaging methods can resolve the tissues down to micron lengths but the conformed radiation area will still damage the surrounding tissue. Chemotherapy has the problem of drugs not being able to cross the blood brain barrier¹⁴. Alongside that, a study in 1992 found no dose response to GBM during RT¹⁵.

The first step in the treatment is generally surgical resection. Fluorescence guided imaging has been especially helpful in locating the tumor boundaries. After surgery, the standard practice is chemoradiotherapy. The radiation portion uses a high dose volume and delivers 50 to 60 Gy in fractions of 1.8 to 2.0 Gy¹². Older patients can receive higher fraction doses to reduce the treatment duration from the above 6-week schedule to 40 Gy in 15 fractions over 3 weeks.

According to Anton 2012, there has not been shown to be a significant difference between conventional external beam radiotherapy (EBRT), stereotactic radiotherapy (SRS),

or brachytherapy. Alongside that, a study involving 203 patients has shown that post-op SRS followed by EBRT did not improve the outcome or quality of life when compared to the treatment not involving SRS¹², which is supposed to control healthy tissue doing by dropping the radiation dose at the borders of the tumor.

One of the problems with RT is that it can lead to delayed radiation necrosis which can act as contrast enhancement in an MRI. This makes it difficult to determine if the enhancing lesion is due to the recurrence of the GBM or from radiation necrosis¹⁶.

GBMs are also hypoxic, which makes them especially resistant to ionizing radiation. It is thought that the rapid growth of the tumor strips the vascular supply and creates hypoxic regions inside that send proangiogenic signals¹⁷. It has been shown in a variety of cancers that low oxygen tension is correlated with localized recurrences and metastases. Spontaneous necrosis has been frequently noted in GBM and it is hypothesized to occur from diffusion-limited hypoxia. The existence of hypoxic regions in GBMs came from a study that used polarographic electrodes to show that in 10 patients, 9.5-68.5% of the probed locations in each tumor had oxygen partial pressures of less than 2.5 mm Hg¹⁸.

This radio-resistance can be overcome by restoring tumor oxygenation and adding a radiosensitizer. One option of oxygenation would be to reverse any anemia, a common condition in cancer patients. Though the correlation only exists between low hemoglobin levels and radiation and chemotherapy resistance, it is believed that fixing one may fix the other. This has only been shown to be successful in animal models¹⁷.

Another option is increasing the oxygen supply during respiration. High pressure oxygen has been shown to improve the effectiveness of radiation therapy and to accomplish

this without the delivery of hyperbaric oxygen during treatment, hyperoxic gas carbogen (95% O₂+5% CO₂) is used in feasibility studies.

Aside from oxygen, two radiosensitizers for brain tumor irradiation present as possible successes: motexafin gadolinium (MGd) and efaproxiral. MGd concentrates in tumors over normal tissue and acts as a contrast agent in an MRI. In an irradiation study, the median time to neurological progression was improved by 5 months in those receiving MGd with their normal radiation therapy treatment. Efaproxiral binds to hemoglobin and reduces oxygen binding, leading to greater oxygen release to the tissues, though it has yet to be studied in GBM¹⁷.

1.2 Radiation Therapy

Radiation therapy is the main treatment modality for diseases like lung cancer¹⁹ and is used in over half of cancer patients as part of their treatment. The goal of RT is to have a therapeutic ratio – the ratio of cancer tissue vs healthy tissue damaged by the radiation. It has been shown that a higher dose results in an improved local control of the tumor¹⁹ but the higher dose increases toxicity to the healthy tissue surrounding it. This brought on the idea of 3D conformal radiation therapy which targets the tumor by using multiple entrance angles of radiation to ensure that the tumor receives the maximal dose and greatly dropping the dose after crossing the boundary to the surrounding tissue. The hypothesis behind this technique was that conformal radiation would allow for a higher local dose which would translate into an improvement in local control.

The next step up from 3D-CRT is intensity modulated RT (IMRT), which divides each large CRT beam into numerous small ‘beamlets’, and adjusts the intensity of each one

individually to achieve complex dose distributions that further conform to the tumor shape. IMRT requires a larger amount of beams, generally 5 to 9, for each fraction²⁰.

IMRT makes it possible to increase the dose gradient at the tumor boundary. The strategy is to treat the tumor region with increase dose volumes but also to “carve out” dose-limiting regions around sensitive structures where there is little chance of tumor expansion²¹. This was not possible with other modalities because of the difficulty of producing specific treatment volumes with uniform irradiation fields. Examples of conformation avoidance include sparing uninvolved parotid glands, auditory apparatus, mucosa and larynx in head and neck radiotherapy²¹.

There are several drawbacks to IMRT. The first is that the treatment plans are more complex and take longer to deliver. Alongside that, the accuracy without any image guidance or patient immobilization, physiological motion ruins the dose distribution. To account for motion and uncertainty, an increased integral dose is delivered. The lengthy treatment may also cause an increased tumor cell repair during the radiation delivery²⁰. Lastly, IMRT increases the monitor units— amount of radiation produced by the linac which are associated with an increase in scatter radiation, which would increase the total-body dose²².

The development of image guided therapy and hypofractionation improved upon the problems of fixed field radiation treatment. IGRT ensured that the treatment was delivered to the correct location after positioning the patient. This also lead to the decrease of the ‘safety margin’ which was set around the tumor to account for positioning errors²⁰. An issue that arouse was the increased total treatment time as a result of this added imaging benefit. Hypofractionation is the delivery of much larger daily doses than the

standard 2Gy per day. An example would be for stereotactic lung radiotherapy, where three fractions of 20 Gy are delivered with excellent local control results. Fixed field delivery, however, increases the radiation time greatly as well.

To counter these problems, arc therapy became a treatment option. Arc therapy rotates the radiation beam while it is on, treating the patient from all angles. The idea behind its improvement over IMRT is that it not only covers all angles and provides a better conformal shape, but also it being on while moving speeds up the treatment process. While the selection of the 5-9 beam angles is difficult and time consuming for IMRT, arc therapy removes the necessity of that calculation.

There are two types of arc therapy: tomotherapy and volumetric modulate arc therapy. Tomotherapy is the RT version of CT imaging where a thin radiation beam treats axial slices of the patient by rotating around them as they moves through the machine longitudinally. In order to avoid 'hot' or 'cold' spots between the slices, some system move the beam helically around the patient. This geometry also allows for CT imaging prior to treatment and an accurate dose distribution to be made from knowing the exit dose. Tomotherapy has been implemented in many tumor regions and in a study of effectiveness between it and 3D-CRT in 60 patients, it was found that tomotherapy plans were equivalent or superior to 3D-CRT in 95% of cases²⁰. Compared to IMRT, tomotherapy was shown to provide an equivalent or slightly improved dose distribution but no treatment time comparisons have been reported.

In 2007, a new form of arc therapy called volumetric modulated arc therapy was introduced. In this RT modality, the dose rate, beam shape, and rotation speed are altered as the on beam is rotated. It differs from tomotherapy in that it can treat the entire tumor

at once in one rotation, making the treatment time independent on the tumor size²⁰.

Compared to IMRT, VMAT produced similar or improved dose distributions along with a reduced treatment time of 1.5-3 mins. It also showed a reduction in monitor units by about 50%²⁰. An extension to this system would be to use multiple arcs to improve dose distributions.

With these advancements in ionizing radiation therapy, another treatment method that is becoming more common and gaining a lot of popularity in research is proton and heavy ion therapy. The premise of proton therapy is the Bragg peak which creates a favorable depth-dose distribution for tumor treatment. Since the Bragg peak for particles of a single energy is very narrow, a combination of beams of varying energies can be superimposed to produce a spread-out Bragg peak that conforms to the tumor shape, which looks very favorable to tumors with proximity of critical dose-limiting normal tissue. The Bragg curve characteristics indicate that proton therapy can rival with the most advanced X-ray methods, including IMRT²³.

There are twenty centers in the world that use protons therapy, and three use ¹²C ions. About 5,000 patients have been treated with ¹²C ions and 50,000 with protons²³. Proton therapy has been used to treat a wide variety of areas, including the head and neck, liver, brain, upper abdomen, pelvis, lung cancer, and in the vicinity of the spinal cord. It is particularly a favorable option for pediatric tumors where more complications are expected from stray radiation due to the increased inherent tissue sensitivity²³.

Due to the lack of phase III clinical trials, it is hard to firmly compare the success of proton therapy, C-ion therapy, IMRT and conventional conformal. There are simply not enough centers and patients to state the clinical effectiveness of particle-based therapy.

However, Durante 2009 claims that there is enough evidence to conclude that proton or C-ion therapies are superior to IMRT for the “most favorable tumor sites and subtypes, in particular ocular melanoma, adenoid cystic carcinoma and chordomas or chondrosarcomas of the base of the skull”²³.

1.3 Treatment Planning

New innovations in radiation therapy (RT) all push towards achieving a high therapeutic ratio – the ratio of the cancer tissue to normal tissue damage. Therapy modalities such as 3D conformal radiation therapy (CRT) and intensity modulated radiation therapy (IMRT) are based on conforming the radiation beam to the tumor by drastically reducing the dose at the tumor boundary. To make these modalities work, an imaging step is required. Standard 2D images do not provide the necessary tumor shape and results in higher planning target volumes (PTV) to compensate for patient motion and tumor location variability.

A planning CT is taken prior to treatment to obtain anatomical data and electron density information. This is necessary for target definition, normal tissue delineation, an overall anatomic model of the body, and dose calculations. This information is then used to segment the different organs and tissue, along with the tumor region, to determine the PTV. Whole organ contouring is especially important for accurate dose calculations during treatment. Contrast is often used to visualize distinctions between soft tissues but this can also make accurate dose calculations difficult as it distorts the apparent electron density of the tissue. The anatomical data will also later be used in either image registration if another imaging modality is used or during patient positioning. CT imaging has the advantages over other modalities in that it is high resolution, geometrically accurate, and is quickly obtained²⁴.

CT is not necessarily the best imaging modality on its own, however. A lot of imaging systems are moving towards multi-modality integration to get better resolution and contrast for different types of tissues. A PET/CT is an example of one type of such integration that combines the benefit of CT's anatomical structure information and PET's biological processes imaging. In a study comparing the two systems, the gross tumor volume was (correctly) changed by 10–50% by doctors using PET/CT planning vs just CT. Another important finding was the increase in the consistency of tumor volume definition between doctors²⁵.

Another imaging modality used alone or together with CT is MRI. MRI is the choice for brain imaging because of increased conspicuity of lesions, better tumor grading, and a better visualization of the extent of the disease as compared to CT. Sinus and nasopharynx imaging is also preferred to be done with MRI because of the tendency of these tumor types to spread along the cranial nerves and by deep tissue infiltration into the pharyngobasilar fascia, cartilaginous eustachian tube, and palatine muscles. These areas are better seen with MRI than with CT²⁴.

In the case of mice imaging for MRT treatment, both MRI and CT have their advantages and disadvantages. An MRI is great as resolving the tumor location. It provides the necessary bone features to be able to register a sagittal slice to the planar X-ray and connect the tumor location to the mouse bed location, and thus the beam position. The downside of MRI is the (current) inability of MRT integration, so the mouse must be placed in a different bed and be imaged at an outside location before being positioned for therapy. This poses a lot of positioning errors and registration problems. The CT removes this problem as it is integrated with our therapy unit and no repositioning errors exist. The downside of CT imaging is the ability of actually seeing the tumor. Given

enough contrast agent, a contrast CT will provide an acceptable tumor outline but that adds an additional variable into our therapy (a radiosensitizer).

The perfect combination would be an MRI planning image combined with a contrast CT pretreatment image after specimen immobilization. The 3D data from both modalities would greatly improve our current manual registration method using only 2 slices from what we guess are the same plane.

APPENDIX 2: BACKGROUND ON FIELD EMISSION

2.1 Carbon Nanotube Field Emission

Our X-ray systems use carbon nanotube cathodes rather than the traditional filament cathodes. The concept is based on an electrophoretic process that fabricates composite CNT film cathode structures. The cathodes have enhanced macroscopic field emission current density and were shown to have a stable emission for 300 hours²⁶.

Every field emission source utilizes field enhancement from sharp tips. Spindt tip emitters have a cone shaped protrusions with an extraction electrode a few microns away, allowing for very low voltages to produce electrons²⁷. Examples include an emitter with a 200 V turn-on voltage that produces up to 300 mA of emission current at $\sim 40 \text{ A/cm}^2$ ²⁸ which is substantially higher than CNT emitters²⁶. The downside to Spindt tips is their high manufacturing cost and low lifetime. Tip failure is most often caused by ion bombardment from residual gases. In Schwoebel et al, out of 200 tested cathodes, about 100 failed with ~ 50 suffering catastrophic failure. The times to failure ranged from less than 10 minutes to greater than 50 hours of operational time. Nanostructured diamond was another field emitter tested but was found to be unstable for long periods of time at higher current densities.

CNTs have a combination of properties that make them a better field emitter: high electrical and thermal conductivity, nanometer-size diameter, better structural integrity, and chemical stability²⁶.

The work function of the material in part determines its emission properties. The current density from field emission is governed by the Fowler-Nordheim Equation:

$$J = AE^2 \exp\left(\frac{-b\phi^{\frac{3}{2}}}{\beta E}\right)$$

where J is the current density of emission from the material, ϕ is the work function of the material, β is the field enhancement factor, E is the applied electric field, and A and b are constants. From the equation, we can see that a drop in the work function increases the current density. The SWNT work function has been measured to be 4.8 eV, very close to the value of graphite. It was experimentally shown that the work function could be reduced to 2.5 eV by Cs doping. The downside is that the doped CNTs are air sensitive and easily de-intercalate with a high emission current²⁶.

The equation also shows the relationship between the work function of the material and the field enhancement factor. The sharpness of the CNT tips results in a very large field enhancement factor which counteracts the lower work function of other materials, making CNTs the better field emitters.

On the micro scale, a single CNT can emit a very large current. Single MWNTs have been shown to stably emit $\sim 2\mu\text{A}$ for over 100 hours without catastrophic failure, which was only observed at currents over 0.2mA. This corresponds to be current density of $10^8\text{A}/\text{cm}^2$. On the macro scale, even though the current densities are not as high as for the Spindt tips, stable emission currents of over $1.5\text{ A}/\text{cm}^2$ were achieved. An emission lifetime measurement of a 0.50 mm x 2.35 mm cathode showed constant 3 mA current for 90 hours and a comparable current level for over 300 hours at 100% duty cycle was also attained²⁹.

Carbon nanotube emitters have a limited lifetime because of degradation during use. Local heating vaporizes the tubes and ionized gas from emission cause oxidative ablation at

the roots. Other damage can be caused by a strong electric field, which pulls the CNTs off the substrate, resulting in arcing and current decay²⁶.

The CNT orientation affects the emitter lifetime. Aligned CNTs with larger spacing to reduce electrical screening and increase emission. This reduction in CNT density reduces their lifetime. Randomly oriented CNTs emit from the small percentage of tubes oriented towards the anode and the other from those aligned by the electric field. This larger number of CNTs increases the cathode lifetime.

Another related factor is the emission uniformity and CNT type. In a substrate with randomly aligned CNTs, only portions of it emit at a given time. The low current density regions contribute to a shorter lifetime. SWNTs have smaller diameters and better field alignment, leading them to have higher current densities and longer lifetimes.²⁶

A non-uniform electric field caused by an even gate over the substrate will induce higher current emission from a specific region and accelerate the CNT degradation. If the field is high enough from a major deformation in the gate, the loss of adhesion described above will further damage the cathode. Operation under increased pressure in a poor vacuum also leads to cathode degradation and arcing.

2.2 Carbon Nanotube Field Emission X-ray Tubes

The tube power is measured by the equation: $P = I_{cathode} * V_{anode} * T$, where T is the transmission rate. In a thermionic emission tube with no gate/focusing structures, the transmission would be 100% so the average power is simply $P_{avg} = I_{cathode} * V_{anode}$. As the voltage is pulsed, it is generally given as a RMS value, so the peak power is given by $P_{peak} = I_{cathode} * \sqrt{2}V_{anode}$ ³⁰.

In a CNT field emission tube, V_{anode} is the voltage between the anode and the cathode, which, in a grounded cathode setup, would just be the anode voltage. In a grounded gate setup, the V_{anode} would be the anode voltage plus the absolute value of the cathode voltage (potential difference between them).

In a fixed anode field emission microfocus tube, the maximum power is

$$P_{peak} \approx 1.4(X_{f,FWHM})^{0.88}$$

where $X_{f,FWHM}$ is the focal spot size in microns. The determination of the average power is based on how high the field emission current can reach for a specific focal spot size. The tube current is affected by the CNT length, placement density, cathode-gate mesh distance, and cathode voltage. The longer the CNTs, the better alignment they have with the electric field and thus have a higher current output. The more densely packed the CNTs are, the higher the current density produced. The larger the cathode-gate mesh distance, the greater the transmission rate, however this would require a higher cathode-gate voltage.

The X-ray vacuum chamber consists of the cathode assembly and the anode. The cathode assembly has the CNT filaments, a gate mesh above it, and a focusing structure above that. For a stable emission, it was experimentally determined to the gate mesh to ground and the CNT filaments to the negative cathode voltage, as shown in Figure 44. The electric field created between the cathode and the gate pulls the electrons from the CNTs and the resulting electron beam is then focused to a small focal spot and bombarded against the anode.

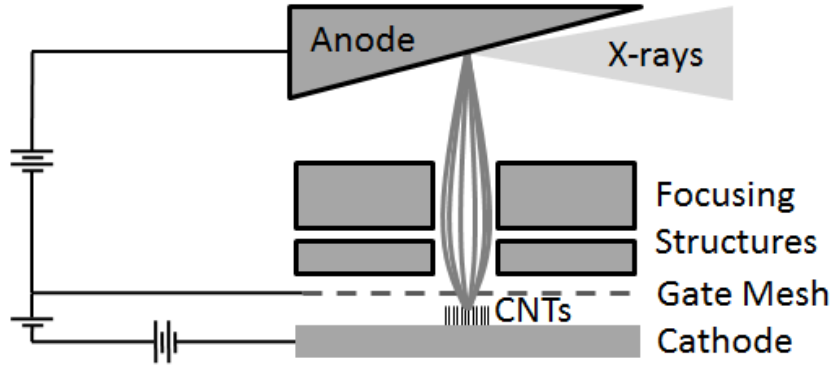


Figure 44. Schematic of a CNT field emission X-ray source.

The anode angle determines the effective focal spot size by linearly scaling the elliptical axis of the emission surface along with the beam intensity profile. The focal spot scaling is determined by the projection of the long axis of the elliptical actual focus spot on the anode, so, for example, to create an isotropic effective focal spot from a 2.35mm x 0.5mm cathode, a $\sin^{-1}\left(\frac{0.5}{2.35}\right) = 12.3^\circ$ anode tilt is required.

The beam intensity profile is determined by the Bremsstrahlung radiation from the electron beam hitting the anode, which is anisotropic. The anisotropy comes from the attenuation of the X-rays at a steeper takeoff angle. As X-ray production occurs at varying depths, the smaller angle requires the photons to pass through more of the anode material and creates a non-homogenous beam profile known as the Heel Effect. The spacial distribution of X-rays around a thin target is shown below in Figure 45³⁰. As we use reflection anodes and not transmission anodes at low energies, only the left side pertains to this. From the chart we can see that at 100 kV, the maximum X-ray flux is at around 40 °.

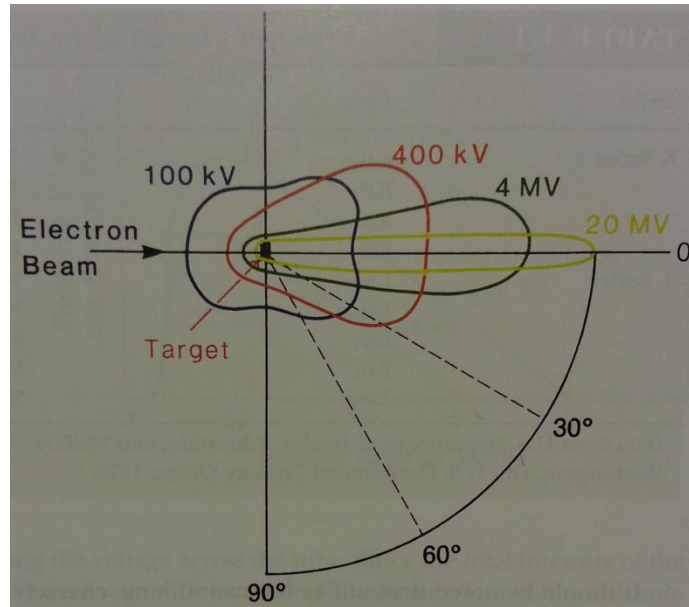


Figure 45. Spatial distribution of X-rays around a thin target.

F. Khan, "Total body irradiation," *The physics of radiation therapy*. 3rd ed. Philadelphia: Lippincott Williams & Wilkins, 455-463 (2003).

2.3 Microbeam Radiation Therapy

Microbeam radiation therapy (MRT) is an experimental therapy method that uses arrays of thin, microplanar X-ray radiation for the treatment of various radio-resistant and deep seated tumors³¹. It was experimentally discovered at the Brookhaven National Laboratory³² decades ago and was soon after studied at the European Synchrotron Radiation Facilities^{33,34}. MRT was shown to have the ability to eradicate tumors while simultaneously sparing the surrounding healthy tissue³⁵. The absorbed dose threshold for tissue damage using these microbeams was on the order of 10^3 Gy, orders of magnitude higher than that for broad beam radiation³⁴⁻³⁷. Synchrotron microbeams are generally 25-75 μm in width and spaced 100-200 μm center to center³⁶ though it has been shown that beams of sizes up to ~ 700 μm have the same tissue sparing effects³⁸ as long as the valley doses are kept under the threshold values. An experimental irradiation of the spinal cords, using 680 μm wide beams at 400 Gy, showed that 3 of the 4 rats tested had no paralysis or

behavioral changes³⁸. Both in vitro and in vivo studies have shown evidence of tumor death and lifespan increase from MRT treatments^{39,40}.

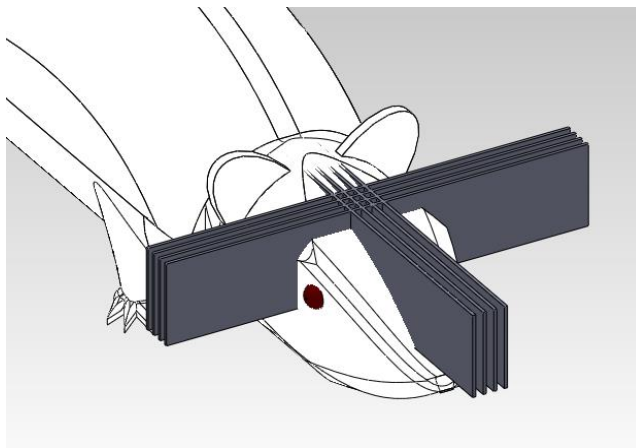


Figure 46. MRT beam visualization using a crosshatched irradiation pattern

One of the major factors determining the effectiveness of MRT is what is known as the valley dose – the dose between the microbeams. This is portrayed through a variable known as the peak-to-valley dose ratio (PVDR). The PVDR in synchrotron experiments ranges from orders of 10 to 100, depending on the procedure. Though the actual biology behind the treatment is not fully understood, a possible explanation is the increased vascular damage from loss of endothelial cells in the tumor versus healthy tissue after MRT beam exposure⁴¹. Another theory is simply keeping the valley dose in the healthy tissue below the threshold dose^{38,42}. Others have postulated bystander effects and cellular communication mechanisms resulting in the tumor cell death from MRT treatment.

Although the concept has been around for over half a century⁴³, it has only been successfully implemented at a few synchrotron light sources around the world^{44,45}. The ultra-high dose rates (>100 Gy/s) allow for the instantaneous delivery of the high dose in

tens of milliseconds, thus maintaining the microbeam profile despite the physiological motion which is on the order of hundreds of microns and the time scale of 100s of milliseconds.

MRT, though very promising, has a lot of setbacks that keep it from moving into the clinical side. The first begin from the synchrotron end. Due to the incredibly high dose rates, the MRT treatment is performed on the order of milliseconds, meaning that a mechanical shutter is necessary to turn the beam on and off. A mechanical shutter has a chance of failure, being a moving part, and a slight offset in timing or a full failure altogether would result in the patient receiving a deadly dose of thousands to tens of thousands of Gy of radiation. From that standpoint alone, FDA approval of clinical use of the system would be very difficult, if not impossible. Another issue is that there are only a handful of synchrotron light sources in the US, slowing down clinical research.

Moving MRT to the laboratory setting poses a new set of problems. The first is the inability to use megavoltage X-rays. The beam energy required to keep the microbeam dose distribution is up to a few hundred keV. After that point, the secondary electron scatter would drastically increase the dose deposition in the valley.⁴⁶ Most of the above conventional sources have radiation in the mega-voltage range. This is because at that energy, all the Compton scatter is in the forward direction and all the dose is deposited in the forward direction, making the penetration depth high and causing a partial skin sparring effect due to a buildup effect⁴⁷. This is a setback because no commercial tube can be modified to perform MRT.

The microbeam geometry is also something that is difficult to reproduce. Conventional sources use a focal spot and a divergent beam geometry that cannot be

collimated into parallel microplanar beams. Each beam would need its own focal spot/line and would have to be collimated to not change the PVDR through the tumor, which is impossible to do. There might be a minimum divergence, however, that would allow for this.

Another issue is the dose rate, which would be much smaller than the one at the synchrotron, thus increasing the treatment time. As the treatment is usually on the order of milliseconds, physiological motion was never an issue. With the decrease in dose rate by many orders of magnitude, respiratory, cardiac, and mass motion create the same problem as with megavoltage beams – microbeam smearing. As the entire premise of MRT working is based on a high PVDR, any motion would damage the procedure's success rate.

2.4 Compact Image Guided MRT System for Small Animal Treatment

Using carbon nanotube (CNT) X-ray source array technology^{26,48} our group has demonstrated the feasibility of a compact image-guided MRT system for the treatment of small animal tumor models^{49,50}. Our device uses a custom-made CNT X-ray source array of individual units with long and narrow focal tracks to deliver the radiation from the focal line, instead of a single point⁴⁹. An external collimator is used to collimate the radiation into a quasi-planar microbeam. The tube delivers a higher dose rate as compared to a conventional micro-focus tube by distributing the electron energy over the long focal tracks with increased heat capacity. The microbeam irradiator is equipped with a micro-CT for image guidance capabilities. A peak dose rate of 2 Gy/s and average dose rate of 1.4 Gy/min are measured in the first generation CNT microbeam irradiator⁴⁹. The average dose rate is expected to be increased to 20 Gy/min in the second generation device, currently under construction, with improved anode thermal management⁵¹. Accurate targeted delivery of

microbeams to the brain tumor regions has been shown using a combined MRI and on-board X-ray projection imaging procedure⁵².

2.5 Desktop MRT System

The tube assembly and cut-a-way view is shown in

Figure 47. The CNT microbeam irradiator is integrated with a homemade micro-CT scanner^{53,54}, a precision mouse-positioning device, a gas anesthesia unit, and physiological monitoring capability. To increase the throughput, two mice can be irradiated at the same time with independent anesthesia and physiological monitoring capacity.

The specially designed linear CNT X-ray source array, as described in previous publications⁴⁹, consists of a linear CNT cathode which emits electrons under a bias extraction field, a gating electrode, an electrostatic focusing lens to focus the electron beam, and an opposing stationary tungsten anode. The electron beam is focused down to a narrow 0.145 mm by 160 mm focal track on the anode. The X-ray source array is operated at 160 kVp anode voltage and a tube current of 30 mA. The mean energy is 60 keV and the HVL was determined to be 7.5mm Al⁴⁹. The intrinsically divergent radiation is collimated into microbeam using a motorized microbeam collimator placed between the X-ray window and the object, 65.2mm below the focal spot on the anode. In the present system, parallel planes of microbeams are delivered by translating the object in the direction perpendicular to the microbeam plane in a step and shoot fashion. A peak-valley-dose-ratio (PVDR) of 16 was obtained at 4:1 pitch/width ratio and 280 mm beam width, measured 124mm below the focal spot or 58.8mm below the collimator. The beam spread angle was calculated to be 0.15°. ⁵²

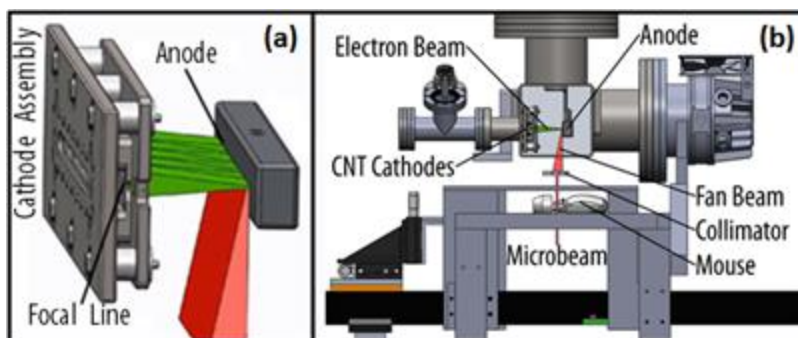


Figure 47. a) Isolated view of the cathode assembly showing the 5 cathodes producing a focal line on the anode. b) Side cutaway view of the MRT tube showing the electron beam from the cathodes hitting the anode and producing the fan beam which is then collimated

2.6 Fluorescence Imaging

2.6.1 Abstract

Microbeam radiation therapy (MRT) uses an array of high-dose, narrow ($\sim 100 \mu\text{m}$) beams separated by a fraction of a millimeter to treat various radio-resistant, deep-seated tumors. MRT has been shown to spare normal tissue up to 1000 Gy of entrance dose while still being highly tumoricidal. The current method of tumor localization for our desktop MRT treatments require MRI and X-ray imaging with subject motion and image registration that contribute to the measurement error. The purpose of this study is to develop a novel form of imaging to quickly and accurately assist in high resolution target positioning for MRT treatments using X-ray fluorescence (XRF).

Our X-ray sources use CNT field emission cathodes and the tube runs at 160kVp anode voltage. Our desktop MRT system uses 5 collimated line sources and delivers a dose of 1.4 Gy/min in therapy mode. The key behind our high accuracy image registration method is using the microbeam to both treat and image, using filtration to lower the dose rate during the latter. High Z contrast media is injected into the phantom or blood pool of

the subject prior to imaging. Using a collimated spectrum analyzer, the region of interest is scanned through the MRT beam and the fluorescence signal is recorded for each slice. The signal can be processed to show vascular differences in the tissue and isolate tumor regions. Using the radiation therapy source as the imaging source, repositioning and registration errors are eliminated. The imaging method was tested on a phantom with iodine-filled capsules and on a non-tumor bearing mouse.

A phantom study showed that a spatial resolution of a fraction of microbeam width can be achieved by precision translation of the mouse stage. Preliminary results from an animal study showed accurate iodine perfusion, confirmed by CT.

A 15 mm brain can be scanned in 13 minutes with sub 200 μ m error. A higher resolution of 100 μ m can be obtained by using a smaller collimator and step size. With a search algorithm, we can image the brain and find high-vasculature regions indicating tumors in under 50 scans, or less than 17 minutes. This is a big improvement on the current procedure that takes over an hour with a larger error. The proposed image guidance method, using XRF to locate tumors, can be used as a fast and accurate MRT treatment planning system.

2.6.2 Motivation

As stated before, accurate targeted delivery of microbeams to the brain tumor regions has been shown using a combined MRI and on-board X-ray projection imaging procedure. Since our dose rate is orders of magnitude lower than the synchrotrons that deliver their total dose in milliseconds, we need to take patient motion into account. Physiological motion is on the order of the beam width and blurs the microbeam lines, destroying the PVDR. The benefit of CNT cathodes versus traditional thermionic X-ray

sources is that field emission X-rays can be modulated electronically by an arbitrary signal such as respiration and cardiac signals^{27,55}. We have successfully shown that our desktop MRT can be physiologically gated to a respiratory cycle⁵⁶.

Another challenge for successfully implementing this system is image guidance. Synchrotron MRTs have little to no guidance due to their incredibly high dose rates and ability to irradiate a large number of beams simultaneously, which lets them irradiate a larger area encompassing the tumor and increasing the likelihood of hitting the tumor. We currently have an image-guidance protocol for targeted delivery of microbeam radiation using an integrated micro-CT⁵⁷ shown in

Figure 47. Accurate tumor targeting is essential to the success of MRT treatments but is quite difficult due to its location deep in the brain and its size of less than 2mm wide. In order to align a 280 μ m beam to this very small target, we implement a hybrid MRI/X-ray image guidance method that registers the MRI image of the head and tumor to the X-ray image from the micro-CT. This method provides an average targeting accuracy of 454 μ m⁵⁷.

The goal of this paper is to develop a new way of faster and more accurate tumor targeting for MRT treatment on our Desktop MRT system. The main contributors to targeting error are errors in the MRI to X-ray registration and repositioning errors during the 2 imaging sessions at different facilities⁵⁷. The method described in this paper uses the therapy beam as the imaging radiation source, to quickly and accurately assist in high resolution target positioning for MRT treatments using X-ray fluorescence. This eliminates the need for multiple imaging modalities and image registration, which contribute to targeting error.

2.6.3 X-ray Fluorescence

The principle behind this imaging modality is the phenomenon of X-ray fluorescence, illustrated in Figure 48. When incoming radiation ionizes an atom, it causes a higher energy electron to fill the hole left by the ejected electron. The energy released by this second electron as it drops into the lower energy level is emitted as a fluorescent photon. Every element has a unique fluorescent photon energy and by using a spectrum analyzer to resolve the photons in that energy range, the element can be determined. The amount of photons released is also directly correlated to the element's concentration, which provides the basis of this research.

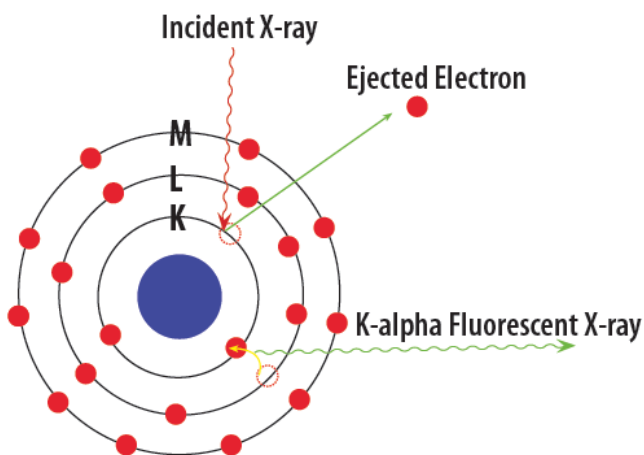


Figure 48. X-ray fluorescence illustration

Sampling different regions using an identical geometry and acquisition time to account for the anisotropic signal can generate a concentration plot of the region. The height of the peak corresponds to the photon counts received by the detector which can be compared to signals from other locations to obtain a relative concentration profile. The goal is to use contrast agents such as iodine to identify the tumor region by sampling slices across the body. Tumors have increased blood flow and thus have a higher uptake of the contrast agent as compared to the surrounding tissue⁵⁸. Though these concentrations are too low to be seen by a contrast CT, a spectrum analyzer can be used to collect X-ray

fluorescence data about the region of interest (ROI) and get relative contraction data that can be used to determine the tumor location.

2.6.4 Methods

2.6.4.1 X-ray Fluorescence Imaging Feasibility Study

MRT requires beam positioning only in one dimension – the longitudinal axis of the mouse – due to its planar beam geometry, allowing a complicated imaging protocol to be condensed into a simple one dimensional step-and-shoot scan. The method is as follows. The animal is injected with a heavy metal contrast agent, such as Iohexol iodine solution, which is allowed to diffuse. Using a slit collimated spectrum analyzer (Amptek XR-100T), the region of interest is slowly scanned through a filtered and hardened MRT beam and the fluorescence signal is recorded for each slice. The different signal strengths can be used to determine leaky vasculature within tumor regions in the brain and other organs. By using the radiation source as the imaging source we eliminate repositioning and registration errors and optimize efficiency.

The best filtration was determined to be ¼” copper. This hardens the beam and pushes the Compton peak far enough towards the higher energy to clear the Iodine region (28.6 keV) of most of the scatter. The filtered beam is then lined up with a copper slit collimator, as shown in

Figure 49, to prevent scatter rays from hitting the active area of the detector but passing all the 90 ° fluorescence X-rays from the slice.

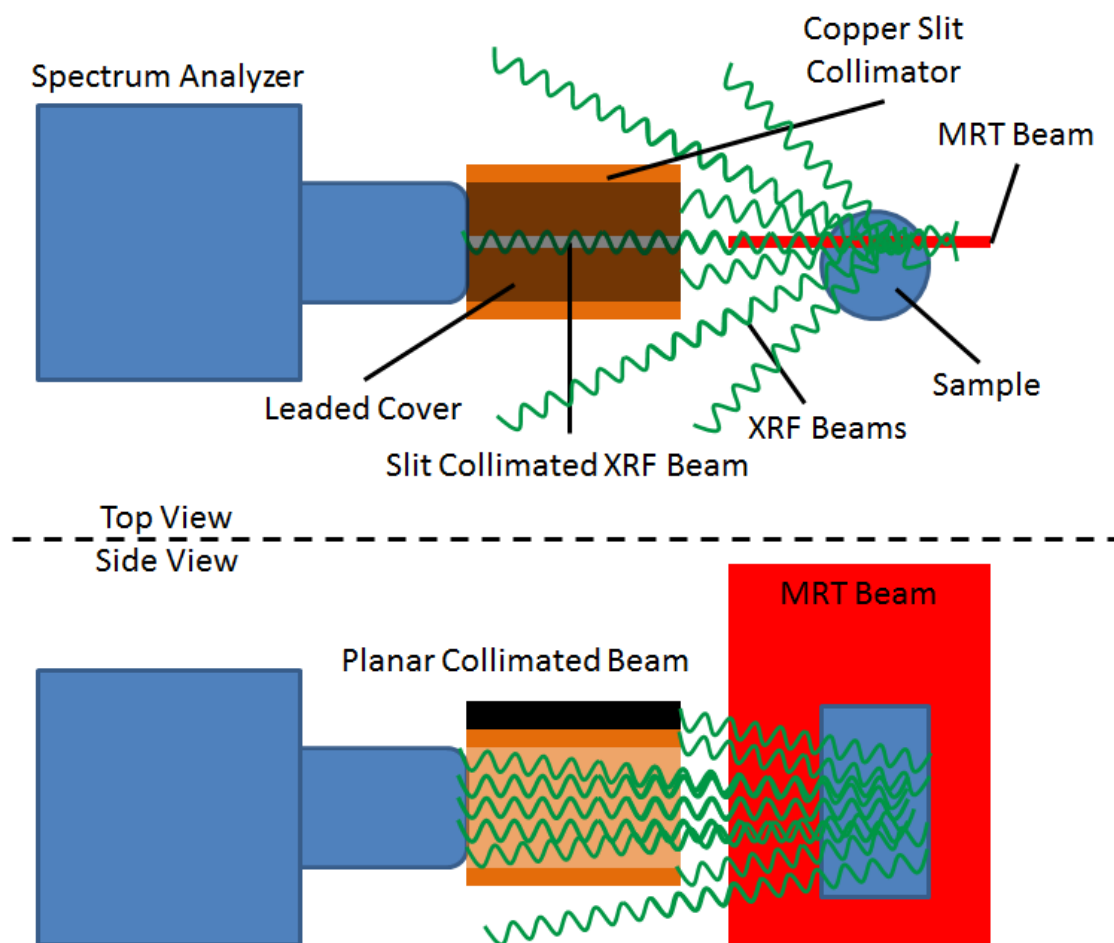


Figure 49. X-ray fluorescence setup with the Amptek spectrum analyzer, the slit collimator, MRT beam positioned directly through the collimator slit, and the sample.

A 3.175 mm wide cylindrical phantom was used to test the feasibility and error as a function of scan time and step size. Literature cites ~22 mg/mL iodine accumulation in tumor at its peak vs ~2 mg/mL in surrounding tissue⁵⁸. The minimum detectable concentration of iodine in our system is around 1 mg/mL, so an 11 mg/mL concentration was used in the phantom. The phantom was scanned at a variety of step sizes and acquisition times ranging from 100-600 μm and 10-20 seconds respectively. The error was recorded as the difference between the full width at half maximum (FWHM) of the resulting signal and the original 3.175 mm width of the cylinder.

2.6.4.2 Mouse Model and Handling

For the in-vivo MRT studies, adult male athymic mice are used. The mouse is placed in a mouse holder 3D printed using fused deposition modeling. The mouse is first sedated in a small chamber and quickly moved onto the mouse stage. The stage holds an anesthesia tube that pumps 1.5-2% isoflurane and oxygen mixture directly to the mouse's face. For body irradiations, the mouse is positioned prone and secured with medical tape to immobilize it. Experimental procedures carried out in this study were approved by the Institutional Animal Care and Use Committee at our institution.

2.6.4.3 X-ray Fluorescence Image Guided MRT

Several infusion studies were performed with non-tumor bearing mice. They show one and ten minute perfusion times respectively. The latter is approximately the time required for the iodine to reach the kidneys. The procedure for the in vivo study is as follows. The mouse is sedated and positioned in the specially designed mouse holder. 10 mL of 300 mg/mL of Iohexol iodine solution is injected into the tail vein. The beam position is located using EBT-2 Gafchromic dosimetry film and a sagittal X-ray is taken of the region of interest (ROI). This step is only necessary for confirmation and error measurement and will not need to be done during real image guided MRT procedures. The region is then slowly scanned across the MRT beam and the fluorescence spectrum is recorded for each slice. This spectrum is then processed to isolate the iodine photon counts and determine a concentration vs beam position plot. This data is then registered to the sagittal X-ray to confirm the location of the tumor. An illustration of the procedure is shown below in Figure 50.

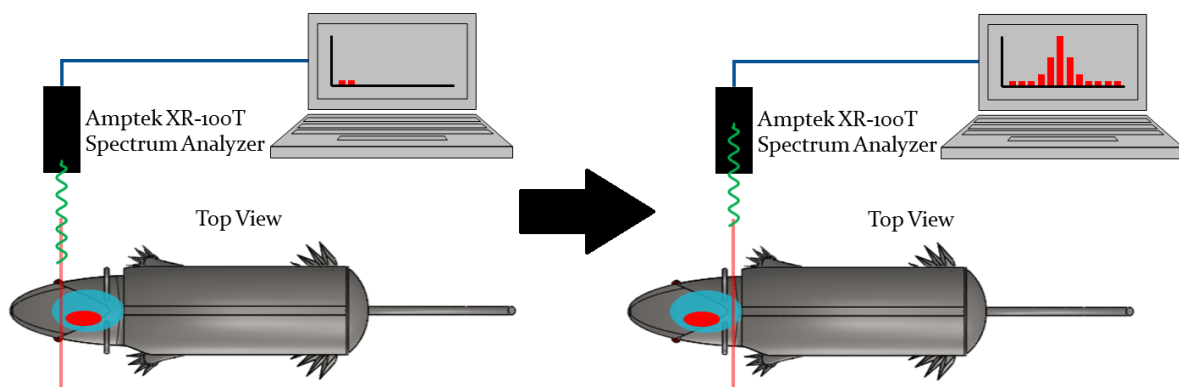


Figure 50. Illustration of the MRT XRF imaging system. The subject is slowly scanned through the MRT beam and the fluorescent signal from the iodine in that slice is recorded and processed. The output is an iodine concentration vs position graph corresponding to the tumor location.

2.6.5 Results

Figure 51 show a sample iodine fluorescence spectrum peak of one of the samples. The signal is calculated by comparing the signal to the background spectrum. Table 1 summarizes the phantom study results and how the step size and acquisition time affect the average error determined from the FWHM calculations. Figure 52 shows a sample processed fluorescent signal vs distance plot. The concentration ratio is obtained from the photon count and gives a relative iodine concentration across the scan.

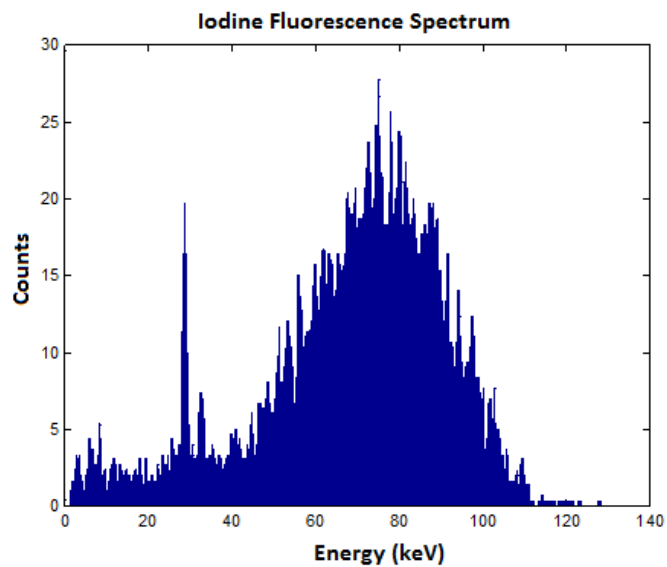


Figure 51. Iodine fluorescence spectrum showing the k alpha peak at 28.6 keV

Table 1. 3.175 mm cylindrical phantom result summary

Step Size	Time/Step	Average Error
0.6 mm	10 seconds	320 um
0.6 mm	20 seconds	240 um
0.2 mm	10 seconds	200 um
0.2 mm	20 seconds	120 um
0.1 mm	10 seconds	40 um
0.1 mm	15 seconds	30 um

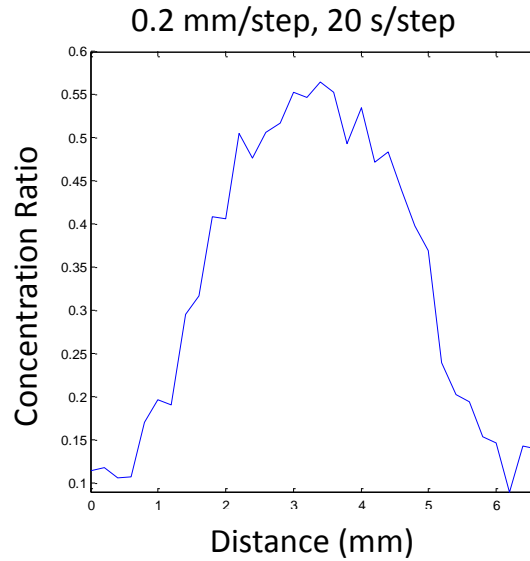


Figure 52. Fluorescent signal vs position of 0.2 mm/step, 20 s/step cylindrical phantom

The in vivo study provided results for a quick 1 minute and a 10 minute perfusion study. Figure 53 shows a side view of the mouse with the starting beam position. Figure 54 shows the relative iodine concentration plot on top of the sagittal X-ray of the short perfusion time mouse. The plot identifies organs with high iodine absorption including the thyroid, heart, liver, spleen, kidneys, and the tail vein, through which in the injection was given.



Figure 53. Mouse in holder with Gafchromic X-ray sensitive film showing the starting radiation beam location

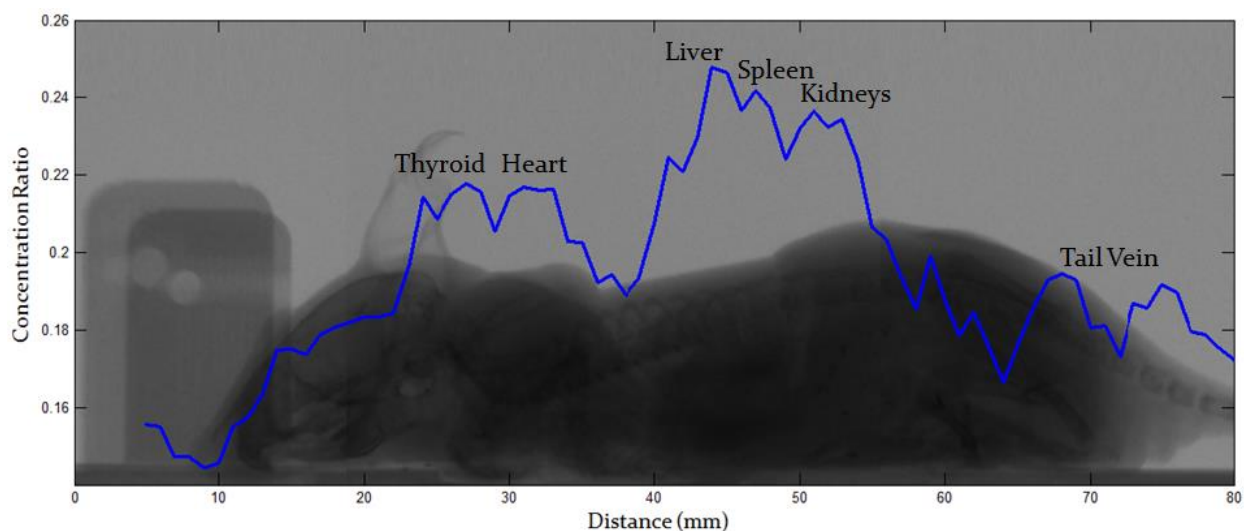


Figure 54. Fluorescent signal vs position graph overlaid on a sagittal projection X-ray. 1 minute perfusion; 1 mm/step, 20 s/step, 80mm total scan distance

The 10 minute perfusion mouse included a contrast CT to confirm the XRF data. The CT showed a large amount of iodine in the kidneys, especially in the central highly vascularized region. Figure 55 shows the concentration plot overlaid on a sagittal projection of the CT data. The heart, liver, and kidneys were segmented and colored. The bright white regions in and below the kidney indicates iodine presence as seen by the CT. The overlaid fluoresce plot (blue) shows how after time, the iodine moves to the kidneys as expected, with some left over in the heart, and none in the liver.

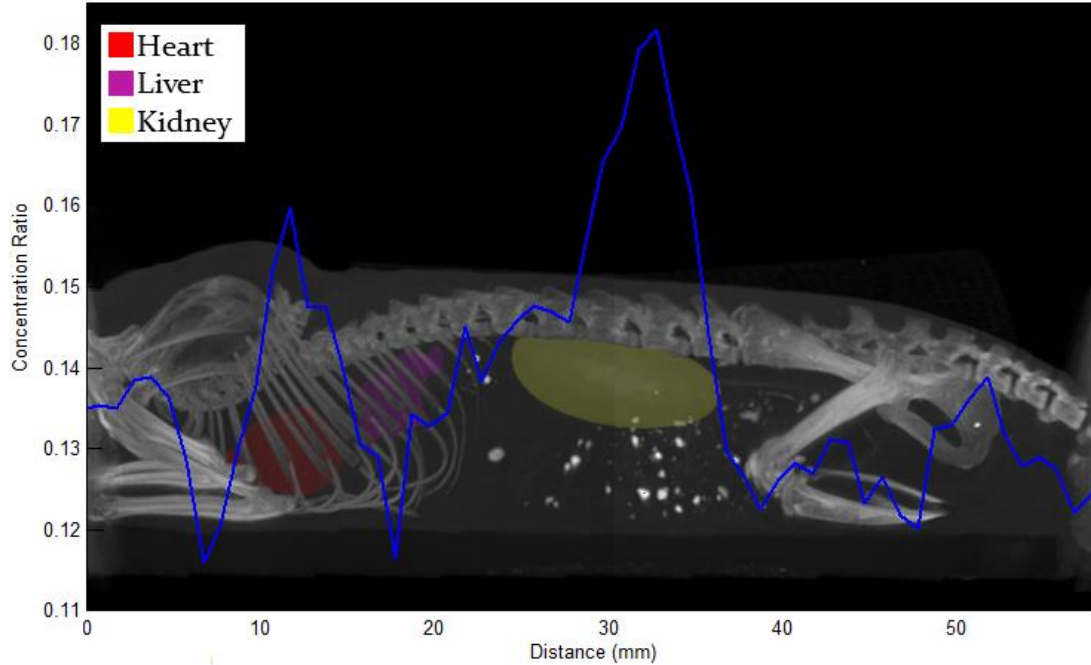


Figure 55. Fluorescent signal vs position graph overlaid on a CT sagittal projection with color marked organs. 10 minute perfusion; 1mm/step, 20 s/step, 90 mm total scan distance

The particle size dictates how the agent is filtered through the body. Smaller particles are processed through the kidneys, while larger particles are filtered through the liver and spleen. This agent is small, and in the short term case it is seen in the hepatic veins and the blood pool in equal measure, but it is not processed by the liver and thus does not dwell there, so in the long term case, it is only present in the kidney vasculature.

2.6.5 Conclusions

The technique presented here showed a proof-of-concept method of XRF MRT guidance. The current procedure for imaging using MRI and CT for targeting takes over an hour with about a 480 μm average error. The proposed tumor targeting method using the radiation source as the imaging source to locate and ablate tumors is fast (a 15 mm brain can be scanned in 13 minutes) and can achieve sub 200 μm error. The speed is the result of reducing the imaging to only one dimension which poses no problem as the therapy beam is

microplanar and extends completely through the body in the transverse plane. Only the location of the tumor in relation to the cranial-caudal axis is needed for therapy guidance.

An additional MRT geometry is interlacing the beams to achieve conformal radiation. This is done by rotating the region and irradiation microplanar beams from different angles, overlapping in the tumor. This imaging method will work for this therapy as well by simply scanning in the same one dimension after rotating the body. This allows for conformal radiation treatment while still using the simple and fast 1D XRF imaging method.

As we use a copper filter to harden the beam and filter out the unnecessary lower energies, the method is also low dose (~ 11.8 mSv mathematically determined). The filter is later removed for treatment. This novel imaging method can make MRT treatment planning on our desktop CNT irradiator practical and efficient. All imaging and therapy can be accomplished on one system, removing any repositioning and registration errors.

2.6.6 Discussion

The fluorescent imaging system for our desktop MRT works by measuring infused iodine concentration ratios between different tissues. The major differences between it and other fluorescence imaging system is that it uses the therapy beam to image the patient and that, since the beam lies in a micro-plane, the imaging can be limited to only one dimension. The basic setup is as follows: a spectrum analyzer is equipped with a slit collimator collimating 8° from the vertical, which is in line with the collimated MRT beam. The mouse is moved in steps equaling the collimator width to get a one dimensional projection of the contrast agent inside the mouse. The reason that this is sufficient is because this matches our current alignment protocol: taking a sagittal X-ray projection of

the mouse's head, registering it to the same MRI slice showing the tumor outline, and moving the mouse to a location such that the beam hits the center of the tumor. In this same way, the XRF system determines the tumor location by assuming higher concentration of iodine due to leaking in 1 dimension and aligning the beam to the center of it.

The spatial resolution is based on the size of the exit collimator and the thickness of the MRT beam. There are 2 cases: the first is where the beam thickness is smaller than the collimator width and the second where it is larger. In the first case, the slice thickness is determined by the width of the microbeam plane and the collimator simply exists to block scatter radiation. This is not the preferred case as the scatter will greatly decrease the percent of fluorescent photons reaching the detector. The second case is where the beam is greater and the collimator selects the slice to measure. This does not decrease the total scatter reaching the detector but increases the amount of 'useful' fluorescent photons. Also this allows us to increase our spatial resolution by decreasing the collimator width.

The limiting factor for spatial resolution is the imaging time. If we assume a 100 μ m step size, imaging a 3cm brain would take 300 steps. The flux is determined by the power of the tube and the filtration, which in turn also depends on the dose delivered during imaging. Let us assume that it takes approximately 10 seconds per slice, which is reasonable from previous experiments. This would mean that the scan would take 50 minutes to get a resolution of 100 microns. Physically our resolution depends on the collimator width but practically it is limited by the allowed imaging time.

The contrast resolution is controlled by the iodine concentration in the tumor. This is dependent on several factors: iodine concentration of the solution, molecular size of the

solution, tumor stage, and diffusion time. The standard iodine contrast agent we use is Iohexol at a concentration of 300 mg/mL. This molecule has 3 iodine atoms and has a molecular mass of 821 g/mol. Higher concentrations of 350 and 400 mg/mL are also available. Literature cites ~22 mg/mL iodine accumulation in a rat tumor at its peak vs ~2mg/mL in surrounding tissue after injection⁴. The MRT tube allows visualization of 1mg/mL iodine so the variation is theoretically possible to be seen. Using a higher flux micro-focus tube, we were able to reach a minimum detectable concentration of 80 ug/mL. This MDC was attained several minutes of imaging. A 10 second exposure was able to get an MDC of 100ug/mL. The molecular size of the contrast agent is also important due to its ability to cross the blood brain barrier and get into the tumor. Glucose molecules, that are much lighter, are being looked at to be carriers of iodine atoms to profuse easier into the brain. There are also shape changing molecules that alter their geometry after crossing the barrier to prevent them from diffusing out. The tumor stage also plays a role. A smaller tumor may not have enough of an increased vascularization to make a huge difference in the iodine concentration. This is why there is a great need for a high iodine atom concentration molecule. On the other hand, a large leaky tumor will have a large iodine uptake that can be measured by the XRF system. The diffusion time is the last factor. From literature, plots of iodine concentrations in tumors vs time show them peaking between 10 and 15 mins and then decreasing down to almost nothing after 30-45 minutes. This is another reason for faster imaging time. A way to go around that would be to continually inject iodine contrast agent over the entire course of the imaging.

Noise reduction of the signal is something that needs a lot of work on. From current data, only about a quarter of a percent of the photons are useful fluorescence photons. The yield of a k-alpha photon from iodine is around 1% and even though it is not an isotropic

emission, the 90 ° acquisition angle only gets $\frac{1}{4}$ of them. Factors reducing the noise include beam hardening past 28.3 keV, below which the photons do not have enough energy to fluoresce iodine and only contribute to unnecessary absorbed dose and scatter. The goal is to harden the beam enough to where the spectrum has essentially no photons below 40-50 keV. This would remove scatter photons in the useful photon range. The downside to that is that it greatly reduces the flux, increasing the acquisition time. An efficient median between these two needs to be found.

Assuming a pre-treating contrast CT exists and we treat at most the day after to ensure the tumor size and shape did not change, the XRF method could be altered to speed up the process and increase spatial resolution. The CT would provide an exact location of the tumor in the brain in relation to the skull, and thus to the mouse bed. This would eliminate the need to scan across the entire head. Mouse bed repositioning error due to screws has been approximated to 150-200 microns. The larger error would be the head position using ear bars assuming the mouse was moved from the bed after planning CT. This could be as large as 1 mm. As we know that position of the beam in relation to the bed, and we would know the position of the tumor in relation to the bed from the CT, within an error of 1.2 mm we know the tumor position. All of the “errors” simply mean that that extra distance would need to be scanned to ensure full tumor coverage. Taking a reasonable tumor length of 2.5mm, this would drop the scanning distance to 3.7 mm, or 6.2 minutes at 100 μ m resolution – a big step up from the 50 minutes calculated above. As the beam imaging is the same beam delivering the therapy dose, there is no additional error added to the system from repositioning.

Some difficulties in this procedure include a retractable filter, detector alignment with the beam, and detector distance from the mouse. The filter is currently mounted on a

rotating axle that can swing out of the way when not in use and swing out over the beam when needed to harden it for imaging. This is still manually done but can be motor controlled in the future. Beam alignment is also a manual task made easier by mounting the entire imaging setup on a two axis translation stage. The alignment procedure includes marking the beam position on a radiosensitive film and measuring the offset from the collimator slit. As the beam is thicker than the slit, an accuracy of $\pm 140 \mu\text{m}$ is required which is achieved through many iterations of micrometer adjustments to the detector position. The distance from the mouse is controlled by a motorized translation stage that can push the detector in and out of the treatment area to image.

The absorption imaging would be done by dropping the kV of the beam, putting a detector below the mouse, and imaging using the fan beam. In this case, a contrast agent would also be needed to see the tumor and a multi-slice planar X-ray image would be developed. The procedure would be the same as with the XRF, adding in the extra step of aligning the detector below to account for the 8° tilt.

In summary, the most significant limitations for accurate targeting are iodine atom concentrations in the contrast agent, the fast infusion/diffusion time of the agent into the tumor, and the slow imaging time due to scatter radiation and lowering of the flux during beam hardening. A downside to this imaging system is that the detector would need to be removing during the MRT side b/c the primary and scatter radiation would damage the detector. Another issue with this type of imaging is the mouse holder, which is on a translation stage that cannot be imaged through. Major modifications would need to be made to the setup to be able to image using the MRT beam.

2.7 Physiologically Gated Microbeam Radiation

2.7.1 Abstract

Microbeam radiation therapy (MRT) uses narrow planes of high dose radiation beams to treat cancerous tumors. This experimental therapy method based on synchrotron radiation has been shown to spare normal tissue at up to 1000Gy of peak entrance dose while still being effective in tumor eradication and extending the lifetime of tumor-bearing small animal models. Motion during treatment can lead to significant movement of microbeam positions resulting in broader beam width and lower peak to valley dose ratio (PVDR), which reduces the effectiveness of MRT. Recently we have demonstrated the feasibility of generating microbeam radiation for small animal treatment using a carbon nanotube (CNT) X-ray source array. The purpose of this study is to incorporate physiological gating to the CNT microbeam irradiator to minimize motion-induced microbeam blurring.

The CNT field emission X-ray source array with a narrow line focal track was operated at 160 kVp. The X-ray radiation was collimated to a single 280 μ m wide microbeam at entrance. The microbeam beam pattern was recorded using EBT2 Gafchromic© films. For the feasibility study, a strip of EBT2 film was attached to an oscillating mechanical phantom mimicking mouse chest respiratory motion. The servo arm was put against a pressure sensor to monitor the motion. The film was irradiated with 3 microbeams under gated and non-gated conditions and the full width at half maximums (FWHM) and PVDRs were compared. An in-vivo study was also performed with adult male athymic mice. The liver was chosen as the target organ for proof of concept due to its large motion during respiration compared to other organs. The mouse was immobilized in a specialized mouse bed and anesthetized using isoflurane. A pressure sensor was attached to a mouse's chest

to monitor its respiration. The output signal triggered the electron extraction voltage of the field emission source such that X-ray was generated only during a portion of the mouse respiratory cycle when there was minimum motion. Parallel planes of microbeams with 12.4 Gy/plane dose and 900 μ m pitch were delivered. The microbeam profiles with and without gating were analyzed using γ -H2Ax immunofluorescence staining.

The phantom study showed that the respiratory motion caused a 50% drop in PVDR from 11.5 when there is no motion to 5.4, whereas there was only a 5.5% decrease in PVDR for gated irradiation compared to the no motion case. In the in-vivo study, the histology result showed gating increased PVDR by a factor of 2.4 compared to the non-gated case, similar to the result from the phantom study. The full width at tenth maximum (FWTM) of the microbeam decreased by 40% with gating, close to the 38% decrease seen in the phantom study.

The CNT field emission X-ray source array can be synchronized to physiological signals for gated delivery of X-ray radiation to minimize motion-induced beam blurring. Gated MRT reduces valley dose between lines during long-time radiation of a moving object. The technique allows for more precise MRT treatments and makes the CNT MRT device practical for extended treatment.

2.7.2 Motivation

Using the compact microbeam irradiator with an inevitably lower dose rate compared to what is used in synchrotron MRT experiments, it is necessary to minimize physiological motion induced microbeam blurring. MRT research so far is mainly focused on the brain tumors. The largest intracranial motion in humans occurs in the optic chiasm with peak displacement of 240 μ m, with the brain stem, midbrain, and medulla displaced by 200 μ m⁵⁹.

Brain movement is correlated with the cardiac cycle⁵⁹. This motion during the exposure time will broaden the width of the radiation track and potentially reduce the effectiveness of the microbeam radiation. Motion blur will become more prevalent in the abdomen due to breathing. Unlike traditional thermionic X-ray sources and, in this matter, the synchrotron sources, field emission X-ray scan be readily modulated electronically by an arbitrary signal such as respiration and cardiac signals^{27,55}. Respiration and cardiac gating has already been applied in-vivo with small animal CT imaging with better than 100 μm accuracy^{55,60}.

The goal of the study is to implement physiological gating of our CNT X-ray source array based MRT system to minimize motion blurring and to increase the PVDR by eliminating radiation during mouse motion. The effectiveness of gating was first evaluated using a mechanical phantom with simulated respiratory motion and then using a mouse model. For demonstration purpose, the liver was targeted due to its large size, motion correlated with breathing, and ease of $\gamma\text{-H2Ax}$ staining to determine the irradiation pattern.

2.7.3 Physiological Motion Monitoring

A physiological monitoring and triggering system (BioVet©, Spin Systems, South Brisbane, Australia) is used to monitor the respiratory motion. The respiration signal is obtained from a sensor pad placed on the surface of the animal under the abdomen to monitor chest cavity motion^{54,55,60}. The respiration sensor is a foam pad encased in a rubber shell attached to thin tubing running into the sensor processor. The signal measures the pressure change in the tubing caused by the compression of the foam.

2.7.4 Mechanical phantom

We designed a phantom to simulate mouse chest respiratory motion using a servo motor. A 50 mm long plastic arm attached to the servo was equipped with a Gafchromic film strip and set in contact with a pressure sensor. The arm was set to rotate 1° with a period of 800 ms and a 25% duty cycle, equating to a motion of about 1 mm which mimics actual mouse breathing motion of the abdomen⁶¹. The setup is shown in Figure 56.

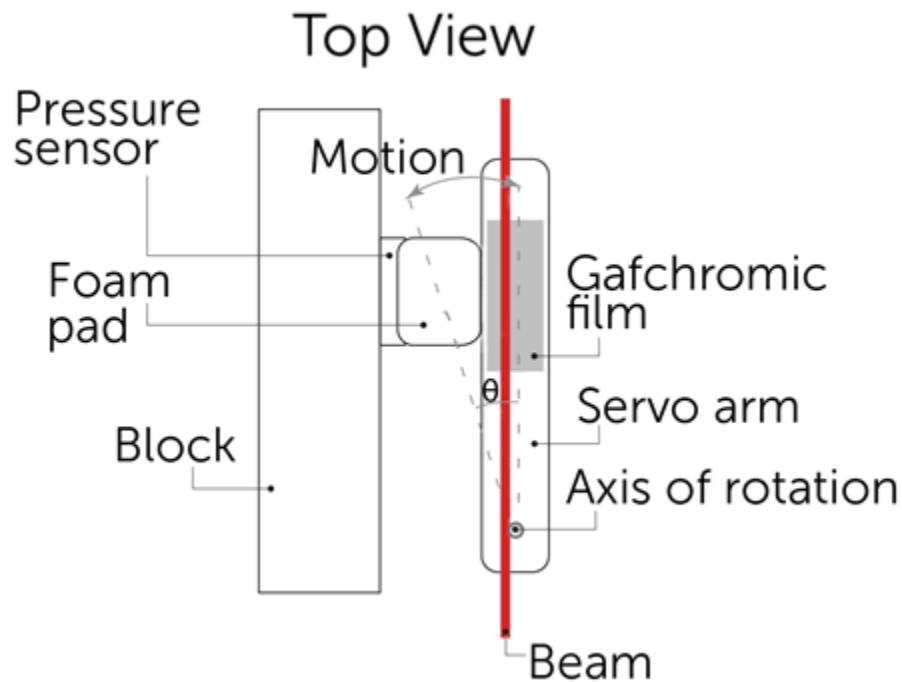


Figure 56. Schematic of phantom using servo motor arm simulating mouse abdominal motion during breathing. The arm is always in contact with the foam pad and the pressure sensor and oscillates in the direction shown.

Previous gating experiments⁵⁵ have shown that the respiration signal is non-sinusoidal and has mass motion 25% of the time and a relaxed period between breaths 75% of the time. A sample respiratory signal is shown in Figure 57. The vertical axis is a differential pressure measurement which is correlated to the chest displacement. The

angular displacement of the servo is shown as a function of time and closely matches an actual respiration signal.

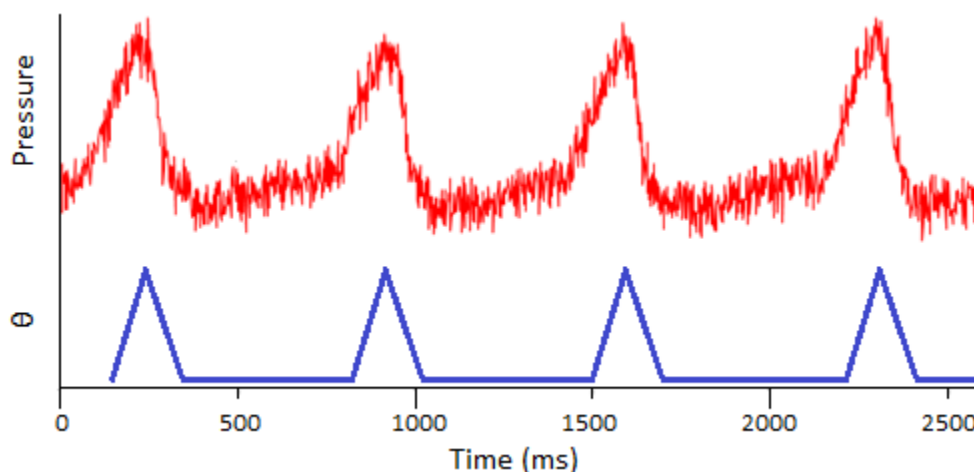


Figure 57. BioVet© differential pressure measurement, correlated to chest displacement, compared to the phantom angular displacement.

2.7.5 Mouse Model and Handling

For the in-vivo MRT studies, adult male athymic mice are used. The mouse is placed in a mouse holder 3D printed using fused deposition modeling. The mouse is first sedated in an induction chamber and quickly moved onto the mouse stage. The stage holds an anesthesia tube that pumps 1.5-2% isoflurane and oxygen mixture directly to the mouse's nose. For body irradiations, the mouse is positioned on its side and taped down with medical tape to immobilize it. Experimental procedures carried out in this study were approved by the Institutional Animal Care and Use Committee at our institution.

2.7.6 Respiratory Gated Irradiation

Figure 3 shows a typical respiratory signal from anesthetized mouse. As it is shown here, there is a periodically short period of time between two inhalations where the chest

is not moving as much. Using this respiratory signal, the constant radiation can be broken up into pulses to irradiate only triggered at the end of the inhalation and last during these “motionless” states. The gating program on the MRT control system runs as follows. The settings are based on individual mice and after the mouse is positioned, the operator waits for its breathing to stabilize while adjusting the anesthesia dose as necessary. During this time, the program reads in several breaths to help the operator get a general idea of the signal. A minimum threshold is set such that the ‘motionless’ baseline is completely underneath it, shown in Figure 58, which sets up the triggers. The operator then determines the ‘on’ time of irradiation by setting a 10% and 20% of the period buffer at the beginning and end of the pulses respectively. In the sample respiratory waveform from Figure 57, the ‘motionless’ state is 500ms long. This requires a 50ms delay buffer at the beginning and a 100ms buffer at the end, making the ‘on’ time 350ms. The pulse diagram is summarized in Figure 58.

The operator then sets a minimum period allowed, generally within 10% of the current period, which shuts off the pulses if crossed and indicates that the mouse is breathing faster and waking up. Because it is normal for the mouse to involuntarily twitch at times and breathe faster for a few breaths, the program reads in and averages the last 6 triggers to determine whether or not to turn off the irradiation. After the mouse is stabilized, the program can be turned back on to resume the treatment.

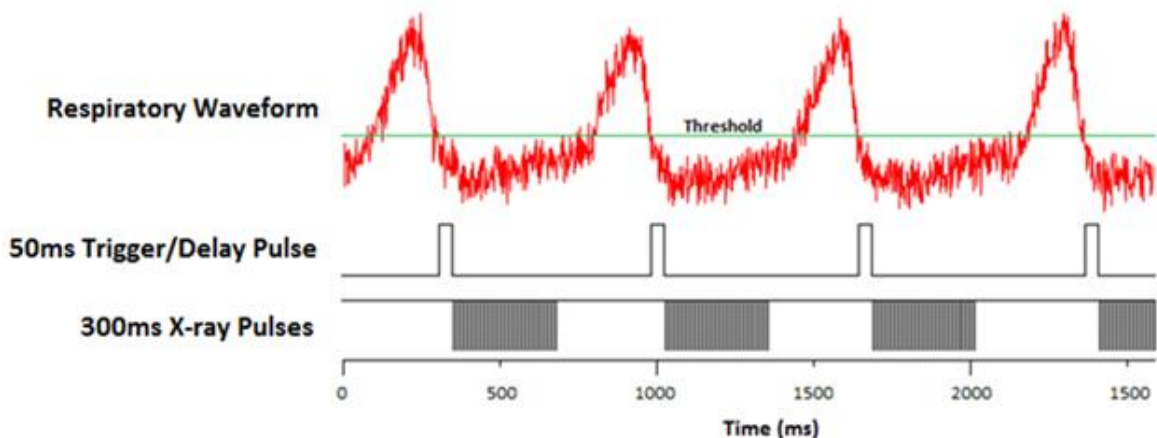


Figure 58. X-ray exposure pulse diagram. The top is the BioVet© output of the respiratory motion from the pressure sensor attached to the mouse. The green line is the threshold set by the operator at as low as possible but still having the ‘motionless’ state below it. The second pulse sequence shows the delay pulses that start the irradiation on a high-to-low trigger. The last sequence shows the cathode pulses that generate the X-rays. The cathodes are negatively pulsed at 500 μ s pulse widths with an 8% duty cycle.

2.7.7 Irradiation Protocols

2.7.7.1 Mechanical Phantom

Two types of experiments were run. The first was a single line irradiation at 160 kVp delivering 1.4 Gy/min for 5 minutes. The second was a three line irradiation, separated by 900 μ m with the same irradiation conditions for each line. We recorded the dose profile by irradiating EBT2 Gafchromic© dosimetry film and scanning and processing the resulting lines.

2.7.7.2 Mouse Study

We ran an in-vivo gated irradiation experiment with 3 microbeam lines. The liver was chosen as the target organ for a proof of concept study due to its large motion during respiration compared to other organs. The liver location was confirmed through a single 2D projection X-ray using the integrated micro-CT imaging system. The beams are marked in

relation to the location of the liver. Each line was separated by 900 μm center-to-center and was delivered 12.4 Gy, which was calculated to be 106,600 pulses.

$$1.4 \frac{\text{Gy}}{\text{min}} \times \frac{1 \text{ min}}{60 \text{ s}} \times \frac{1 \text{ s}}{160 \text{ periods}} = 145.8 \frac{\mu\text{Gy}}{\text{period}}$$

$$12.4 \text{ Gy} = 53.3 \text{ s irradiation on time}$$

$$\frac{53.3 \text{ s}}{500 \mu\text{s/pulse}} = 106,600 \text{ pulses}$$

The first two lines were delivered without gating as a control and the third line was gated to the respiration motion. The irradiation times for each line were 11 mins, 11 mins, and 33 mins respectively.

2.7.8 Histology

To confirm the beam placement, $\gamma\text{-H2AX}$ immunofluorescence staining is used as a quantitative biomarker of radiation-induced DNA double-strand breaks⁶². The mouse was euthanized 1 hour after treatment and its body was fixed in formalin to preserve the liver orientation. The tissue was then embedded in paraffin and sectioned into 5 μm slices in the plane perpendicular to and following the microbeams, shown in Figure 59.

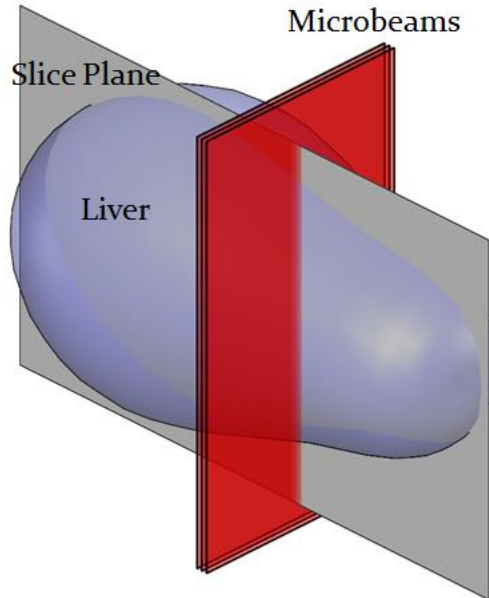


Figure 59. Diagram of histology section plane

The staining protocol was as follows: The tissue slice was hydrated and underwent antigen retrieval process by incubated with citrate buffer. The sample was then incubated with the primary antibody (Phosphohistone H2AX Rabbit anti-mouse antibody, Cell Signaling Technology Inc.) for 60min, followed by incubation with secondary antibody with Cy5 Tyramide and DAPI counter-staining on the nuclei. The section was then scanned using a fluorescence slide scanner system (Scanscope FL scanner, Aperio Inc., Vista, CA) to obtain γ -H2Ax stained images.

2.7.9 Results

2.7.9.1 Film Results from Phantom Study

In the single beam case, the film was scanned and analyzed using Film QA Pro© from Ashland Advanced Material Group. The program determines the shape of the dose pattern along with the dose delivered. Figure 60 shows an example of dose profiles for a single microbeam in three cases: no motion, motion without gating, motion with gating.

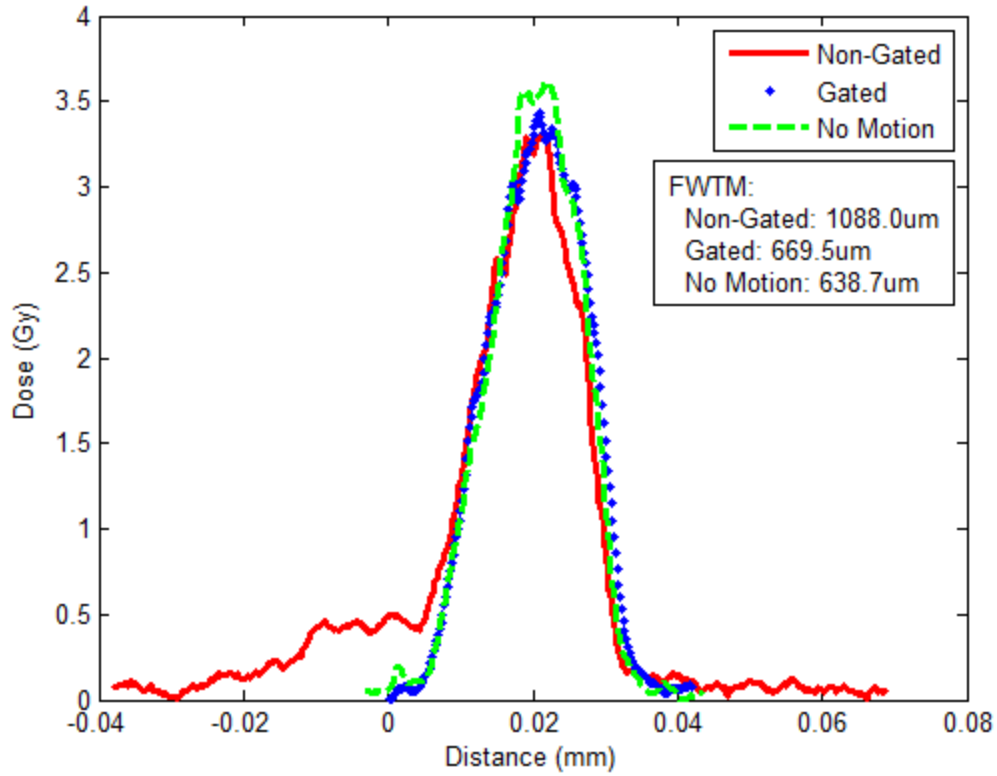


Figure 60. Single beam dose curves for three 5 minute irradiations at 160 kVp

A more important quantity for the effectiveness of the MRT is the PVDR for the multiple line case. Figure 61 shows the beam profiles for three-line irradiations. Here we see how that shelf in the single line affects the PVDR of the multi-line set. The motion causes a 50% drop in PVDR from 11.5 to 5.4 but by effective gating, one can almost recover the PVDR value. There is only 5.5% decrease in PVDR in the case of motion with gating compared to the no motion case. There is also small drop in the peak dose from 3.4 Gy to 3.2 Gy.

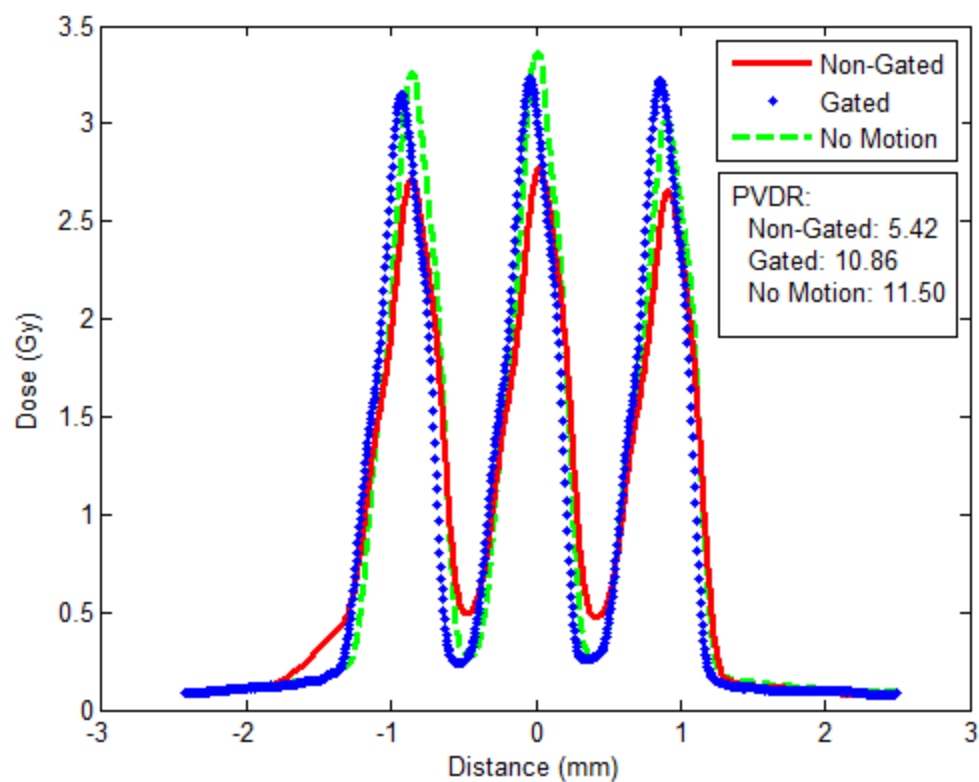


Figure 61. Three beam dose curves for three 5 minute/line irradiations at 160 kVp.

2.7.9.2 Histology Results from Mouse Study

Figure 62 shows the mouse post treatment with the beam lines shown on the Gafchromic film attached to the edge of the mouse bed.



Figure 62. Mouse in the mouse bed post-treatment with MRT beam lines shown on EBT2 Gafchromic© dosimetry film taped to bed.

Figure 63 below shows the γ -H2Ax stained liver sample that highlights double stranded breaks in the DNA from radiation damage to the tissue. The microbeams are clearly seen and their plot profiles are shown in Figure 64. The gated PVDR increased by a factor of 2.4 as compared to the non-gated lines. This is close to the 2.0 factor increase in the phantom study. The FWTM decreased by 40% by gating. This is also close to the 38% decrease seen in the phantom study.

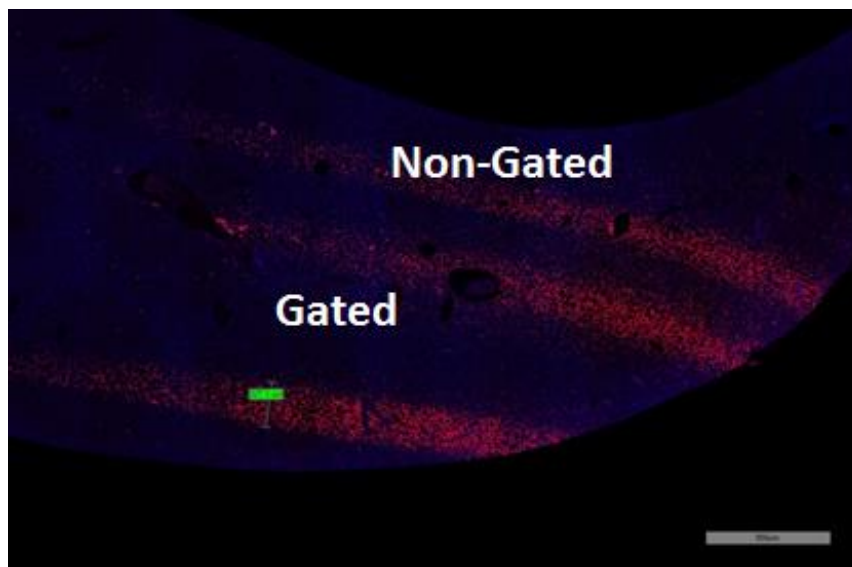


Figure 63. γ -H2Ax staining of a liver cross section showing gated and non-gated lines. The stained points show DNA double strand breaks which is proportional to the dose delivered.

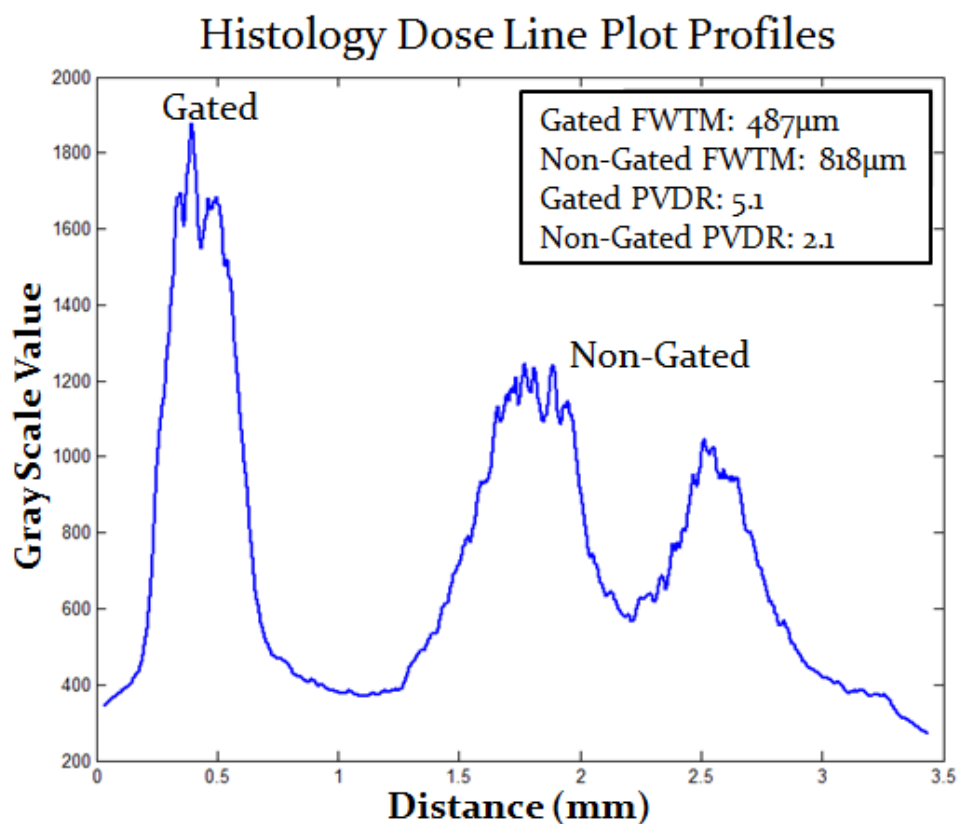


Figure 64. Plot profile of the γ -H2Ax stain in Figure 9.

2.7.10 Conclusions

In this paper, we have shown that physiologically gated MRT is possible using our CNT based field emission microbeam irradiator. We have demonstrated that motion gating reduced valley dose and enhanced PVDR between the lines during long-time irradiation.

From the phantom study, when there is no motion, the FWHM of the dose profile is approximately 440 μm , which is expected from geometrical consideration of the beam spread versus the height. The 280 μm beam width is obtained 1 cm below the collimator during mouse irradiations but as the phantom was much larger, it had to be placed about 13 cm below which broadened the beam to 440 μm . When the phantom motion is turned on, the broadening of the dose profile due to motion is clearly seen in the motion control as a side tail.

The FWHM of all curves is the same because the motion was not sinusoidal. Had it been, the peak would have truly 'broadened' but since the motion was driven by a 25% duty cycle pulse, the movement contribution is seen as the 0.5 Gy shelf to the left. A more accurate measurement would be to look at the full width at tenth maximum (FWTM). FWTM increases from 638 to 1088 μm when the motion is turned on. By applying gating the FWTM is reduced back to 669 μm , almost the same as that without motion.

The irradiation time during gating notably increased from 11 mins to 33 minutes to deliver the same dose. This is because of the off-time enforced during the respiratory motion of the animal. Our tube is run at an 8% duty cycle of 500 μs pulses to prevent over-heating, but during gating, the effective duty cycle was dropped to 2.7% due to the stops

($\frac{11 \text{ mins}}{33 \text{ mins}} \times 8\%$). Assuming the animal's breathing remains mostly constant during the

procedure, we can recover this extra treatment time simply by increasing the duty cycle of the pulses by the factor $\frac{\text{Treatment time with gating}}{\text{Treatment time with 8\% duty cycle}}$, or in our case $8\% \times \frac{33 \text{ mins}}{11 \text{ mins}} = 24\%$.

We further demonstrated its therapy capability of free-breathing mice under their natural position without forced ventilation. With free-breathing, there is no need to do intubation for forced ventilation, thus reducing any damage due to the intubation procedure. Free-breathing also eliminates possible ventilation problems due to changes of tidal volume during treatment, reducing anesthesia caused mortality in forced ventilation.

The technique presented here showed a proof-of-concept method of gated radiation treatment. The liver was chosen due to its increased motion during breathing and the ease of radiation detection using γ -H2AX staining. This technique can be expanded to other areas of the body and can be gated to other physiological signals, such as the cardiac cycle.

2.8 Microbeam Interaction Simulations

Part of the treatment planning of MRT is determining the geometry of the line positions across the ROI. These can be simple parallel beams to more complicated cross-hatching patterns to even further complicated 3D rotated planar combinations. Each of those can produce unique geometrical dose profiles that can be useful is accurate and efficient tumor targeting.

We start with a simulation of a simple rotated single beam line and the dose profiles around the perimeter at various radii. The single dose profile was experimentally derived using Gafchromic X-ray sensitive film. The profiles and the PVDRs are shown in Figure 65.

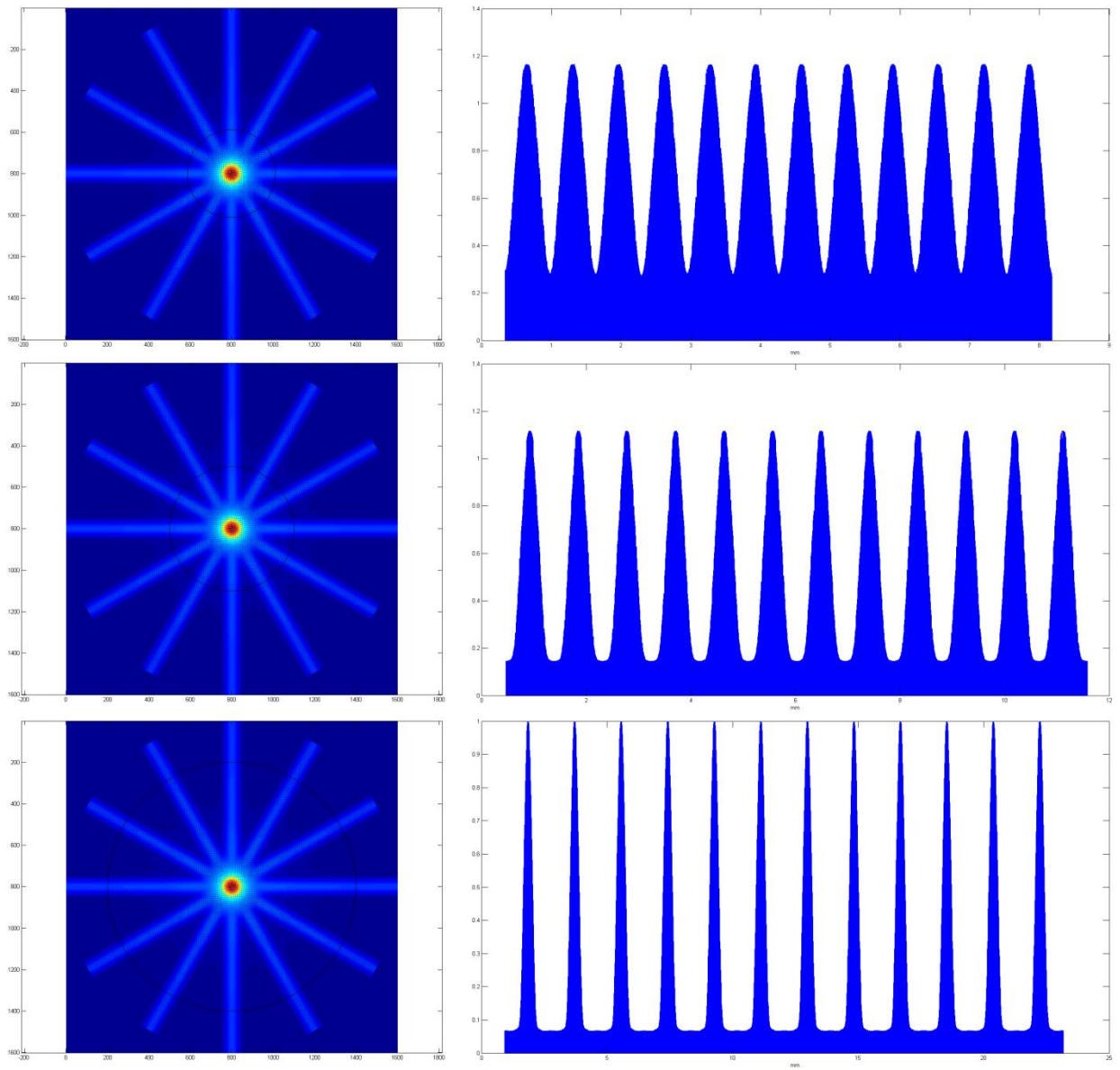


Figure 65. Beam profiles at 3 radii: 1.25mm, 1.77m, and 3.54mm. At the 1.25 radius: PVDR 4.2, 1.77mm radius: PVDR 7.3, 3.54mm radius: PVDR 16.7

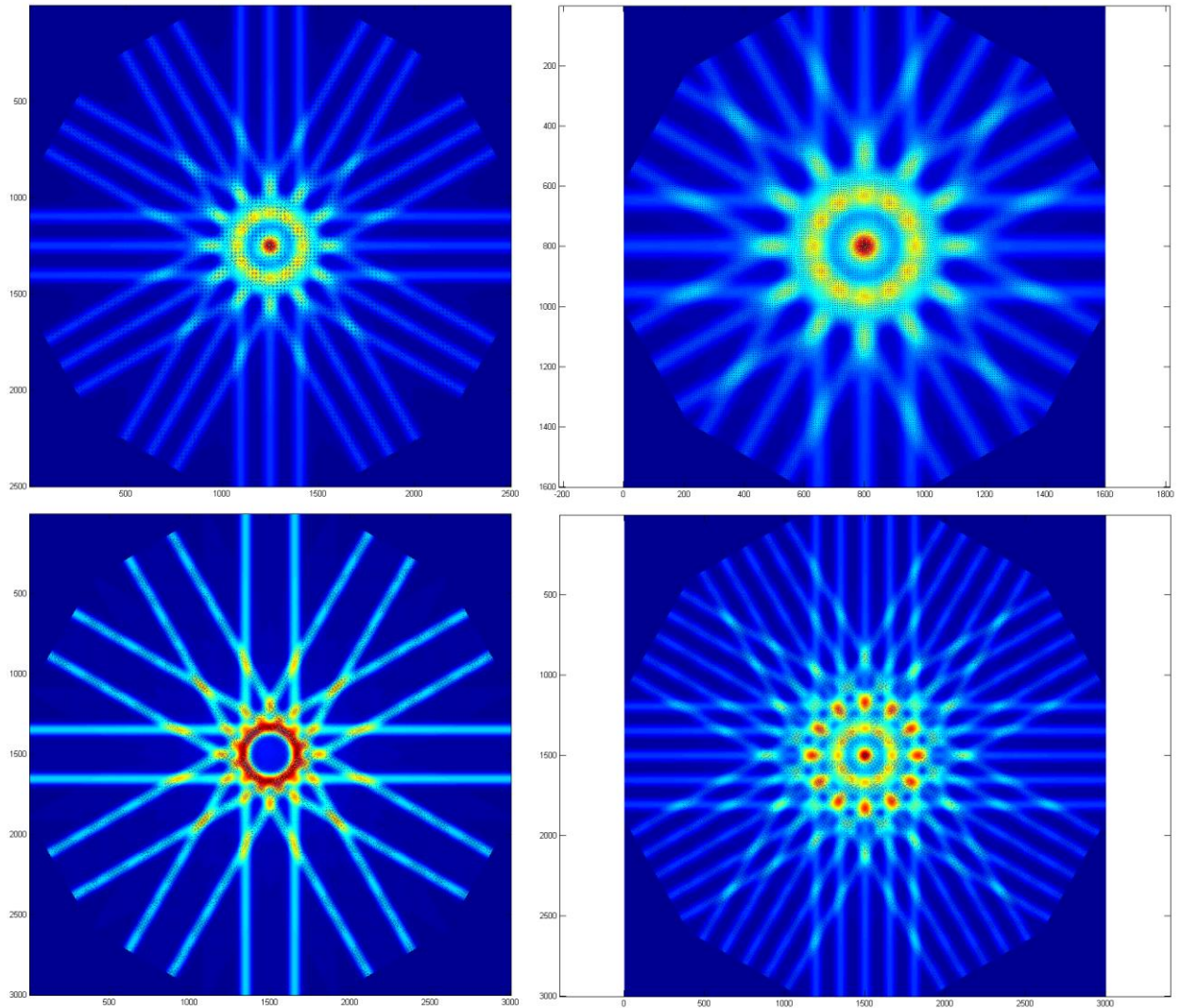


Figure 66. Other simulated line geometries

The simulated patterns in Figure 66 show how line spacing can create high dose rings and low dose regions. This can be further investigated using three dimensional rotations about the micoplanar beams and using even more complex beam line patterns and rotations to create customized treatment patterns.

To evaluate the accuracy of the simulation, a simple three line profile pattern with variable beam spacing was simulated in Figure 67 and the PVDR at 900 μ m was compared

to the actual experimental PVDR. The predicted value of 14.13 is in the range of the experimentally derived values of 14 ± 5 .

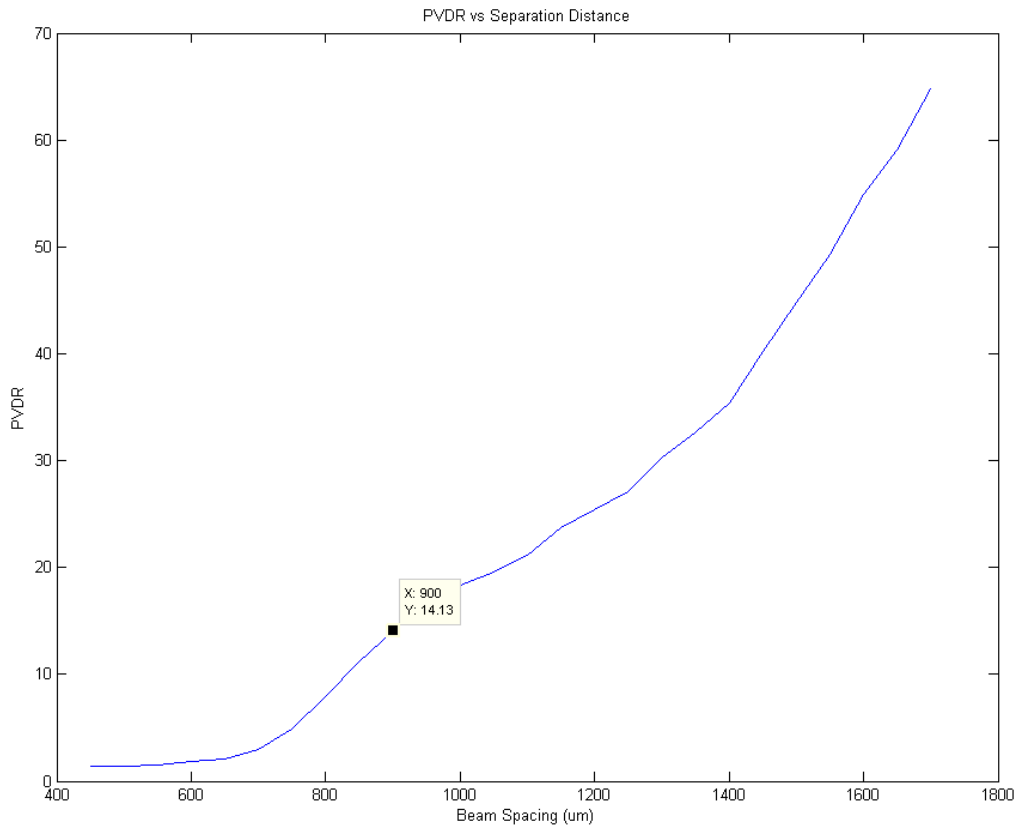


Figure 67. PVDR vs Beam Spacing graph with a point at 900 μ m showing a PVDR of 14.13

APPENDIX 3: SECOND GENERATION DESKTOP MRT (APOLLO II)

3.1 Motivation

The motivation for the second generation desktop MRT stemmed from the limitations of the current MRT tube. The first and most important of these is the dose rate. Current experiments are performed at total doses <100Gy line and at a dose rate of 1.4Gy/line, these experiments not only take hours, which causes stress on the mouse, but also the heating of the tube limits the total dose delivered to be around that 100Gy limit. The synchrotrons are delivering total doses of well in the 100s of Gy and in seconds. The goal of the second generation tube is to deliver the dose achieved at the synchrotrons within a time frame that is clinically feasible and also to deliver simultaneous beams to reduce translations during treatment.

3.2 Specifications

The main reason behind not being able to achieve a high dose rate was the anode heating that prevented continuous operation and the second is that the 160kV power supply is not able to achieve the necessary power output. The new device would therefore need some sort of heat sink on the anode to reduce the localized heating and a way to distribute the heating during the 'on' times to reduce on wasted time during the 'off' phase. To accomplish this, an actively cooled anode assembly was designed to continuously circulate oil across a brazed tube on the anode to pull the heat away during operation. The other requirement would be for an upgraded anode power supply, which we decided should be the Spellman 6kW that would allow 30mA of current at 225kV. A summary of the specifications can be seen in Table 2.

Table 2. Specifications for Apollo II

Characteristics	Apollo I	Apollo II
Anode Voltage	160 kVp	225 kVp
Avg Current	2.4 mA	27 mA
Dose Rate	1.2 Gy/min	25 Gy/min
Number of Lines	1	3
Time for 3 lines at 75Gy/line	3.1 hours	8.9 mins

3.3 Design

3.3.1 Tube

The tube was designed with 3 high voltage feedthroughs, shown in the cross-section in Figure 68. The middle is for the high voltage anode cable and works much like the Apollo I feedthroughs. The two on the side act as the oil intake and outtake valves and also as the high voltage grounds for the oil as it passes through the inside of the tube. The feedthroughs are the standard ceramic cone inputs that are welded onto two flanges. These are attached to the ends of the brazed copper tube on the anode.

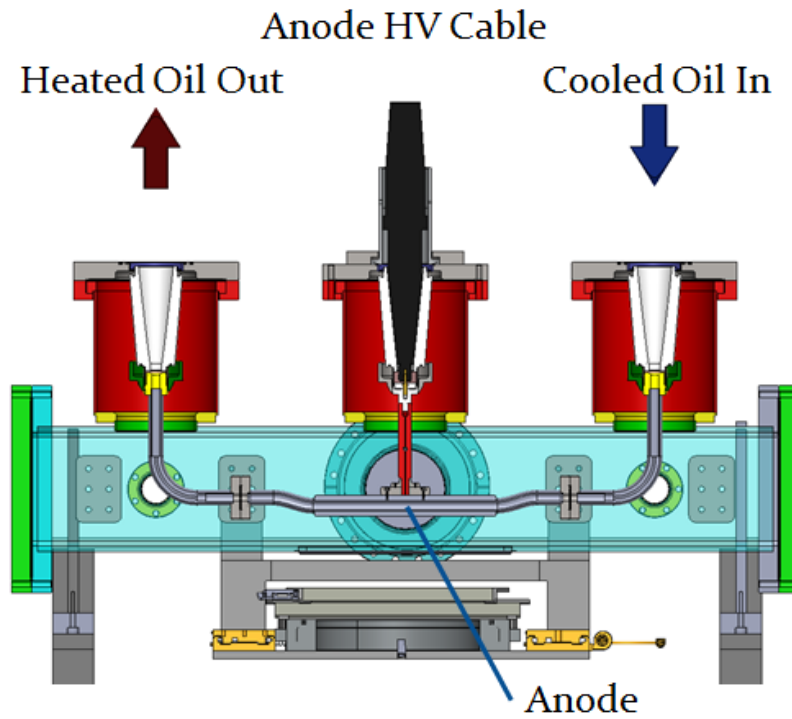


Figure 68. Cross section of Apollo II showing the high voltage feedthrough, anode, and brazed oil cooling feedthrough. Below the anode is the X-ray window and under it is the rotating, variable beam width, three beam collimator.

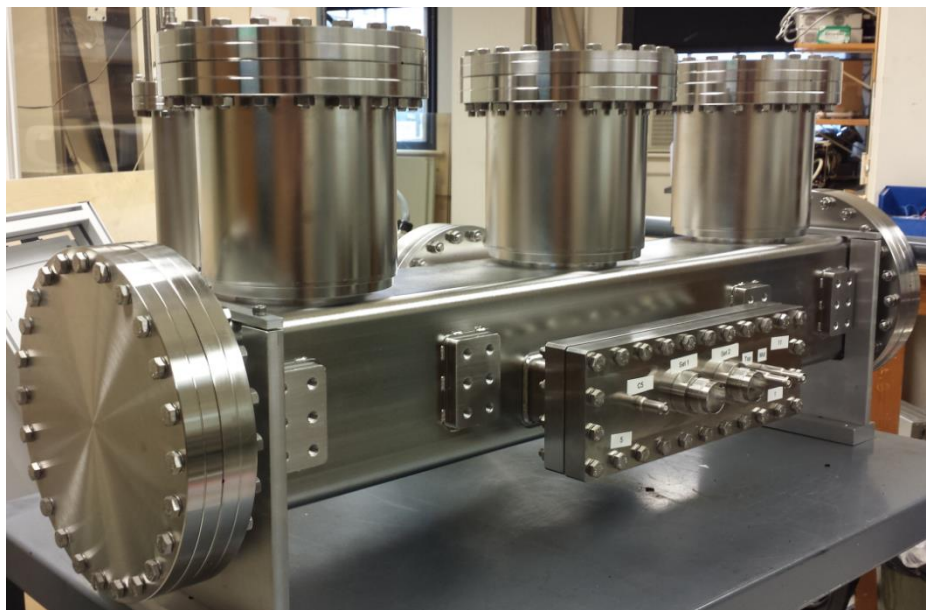


Figure 69. Photo of the Apollo II Tube housing without any electrical connections.

3.3.2 Anode

The anode is designed to withstand 24 times the amount of power of Apollo I. The heat generated by the three electron beams is dissipated through the brazed copper pipe shown below. The anode is attached to the feedthrough above by a screw and a set-screw on the side to prevent rotation during use.

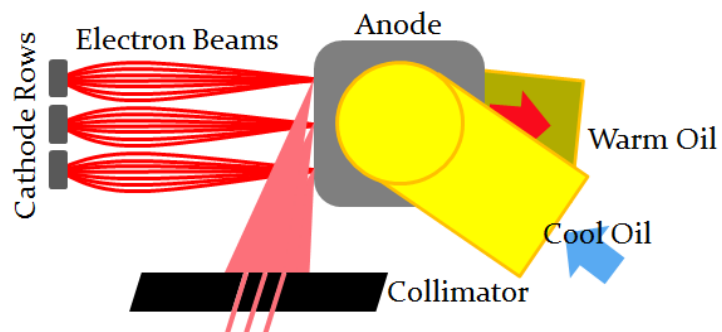


Figure 70. Anode operation showing the three electron beams hitting the 3 rows on the anode and being collimated into three microbeams along with the active oil cooling system

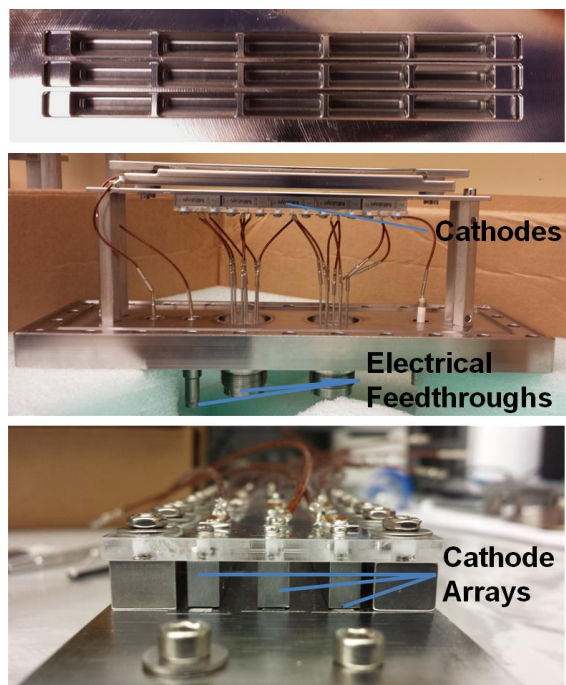
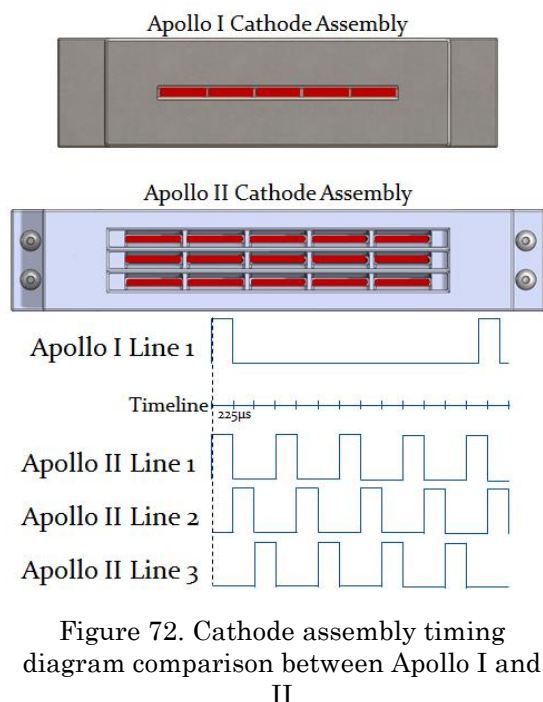


Figure 71. Anode with attached oil tubes seen through the side ports of the chamber.

Figure 71 shows the anode attached with the side flanges removed. Note the window that is covered by the sheet of acrylic to protect it during installation. The oil hoses were installed using a special tool to hold the flange in place to put the necessary torque on the screws. Great care must be taken in assembly and disassembly due to its precarious position above the window and attachment to the high voltage feedthrough above.

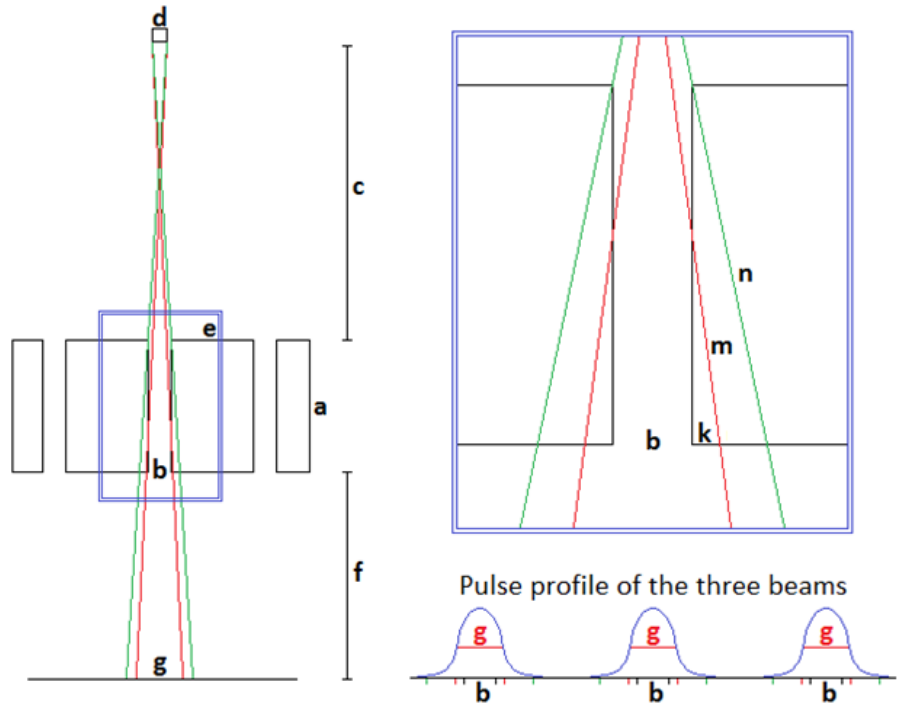
3.3.3 Cathode Assembly

The cathode assembly changed from one row of five cathodes to three rows. The operation is the same but the duty cycle changed from 8% to 99% with each row on 33% of the time and alternating between each row. The timing diagram is shown in Figure 72 and top and side view photos of the cathode assembly are shown in Figure 73.



3.3.4 Collimator

The collimator is designed to align to the 3 rows and provide 300µm beam widths. The design calculations are provided below. The collimator will take into account the beam spread as a function of the position of it in relation to the anode and the specimen and the material of the collimator due to the attenuation along the edges. The design will then be fitted with an external translation, tilt, and rotation stages to align the slits with the beams and also allow for variable beam width using a sliding apparatus.



The beam originates at the focal spot of diameter d and spreads. The collimator of thickness a is located a distance c below the focal spot and has 3 slits of width b cut into it separated by a distance e . The specimen is placed a distance f below the bottom of the collimator. The thickness of the collimator is controlled by the green ray that represents the tail and the valley dose contributor, which should be as low as possible. The full width half maximum of the pulse is controlled by the red ray that travels a distance m in the collimator which coincides with its half value layer. A reasonable n value is $10m$ (.999 attenuation). Solving for the collimator thickness as a function of b and n we get:

$$a = \cos \left(\tan^{-1} \left(\frac{d + \frac{b-d}{2}}{c} \right) \right) n$$

Looking at the other variables and solving the geometry leads to:

$$b = \frac{2\sqrt{a^2 c^2 n^2 - a^4 c^2 - a^2 d}}{a^2}$$

Using two collimator plates, the beams can be made adjustable using a sliding motion illustrated below. The top collimator plate is attached to a small translation stage and allows for 0-300μm bam thicknesses.

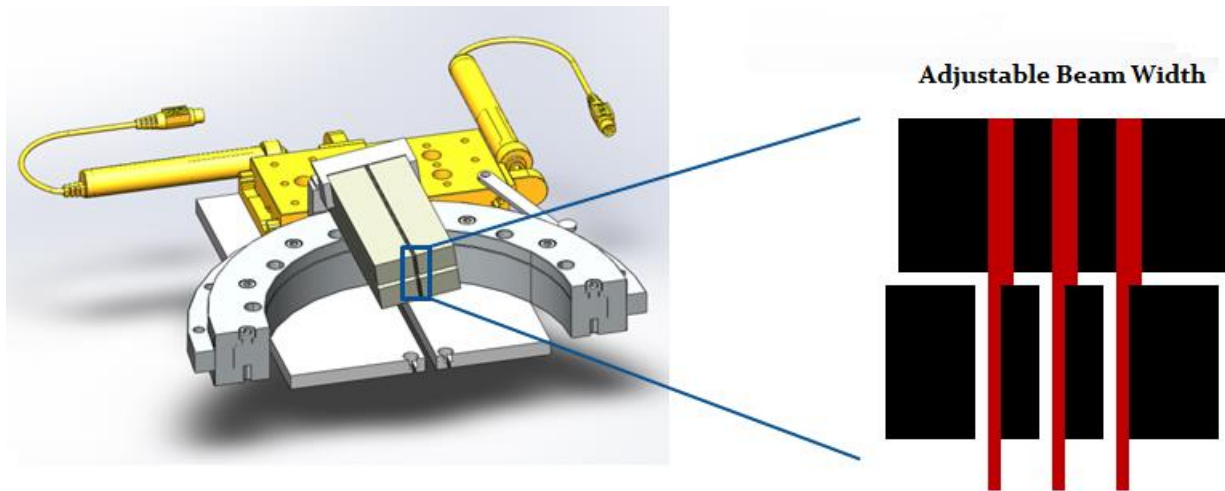


Figure 74. Adjustable multi-slit collimator design.

3.3.5 Enclosure

The enclosure was designed to hold 225kV X-rays in with 99.9% attenuation (10 HVL) and also to be able to hold its own weight and make it easy to get in an out during experimentation. After much discussion, a vertically sliding door design was agreed upon as shown in Figure 75. To make it easy to get into and to have the doors come all the way down to the level of the table, each door consists of two parts that slide next to each other and are connected with heavy chain. To get at most .5% deflection in the beams, 2" steel rods were selected for the frame to hold the approximately 9200 lbs of lead.

Winches were added to the top of the frame to slide the doors up and down, shown in the photos in Figure 76. Steel chain was bolted onto the aluminum backing of the lead walls to hold the sliding sheets. When closed, a set of two lips protruding from each door with holes at the top are used to bolt the doors to the frame. 1" steel rods attached to linear actuators push and pull the rods through the holes to hold the doors safely in place while raised.

The short side doors had the outer protruding shapes to allow for vacuum tubes and electrical wires to pass into the enclosure without damage. The anode and oil feedthroughs came in through the top ceiling. The approximately 1600lb ceiling was divided into 22 sections of roughly 70-75lbs to allow for easy installation/removal and maneuvering.

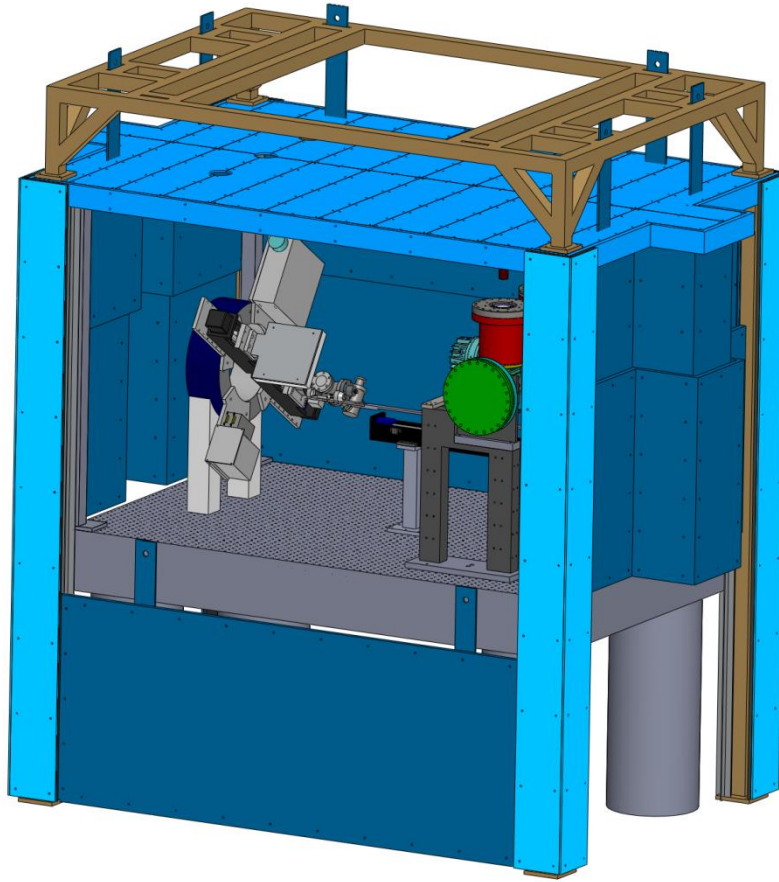


Figure 75. Solidworks model of the enclosure.



Figure 76. Photos of the construction of the enclosure starting with the 2"x2" steel frame, the walls, and the winches that lift them.

3.4 Current Status

After an arcing event that cracked the ceramic feedthrough and melted through the anode cable, the project was put on hold while replacement parts were ordered. Until that point, all 3 of the rows were conditioned to 160kV at 3-4mA.

REFERENCES

- 1 A. Tingberg, "X-ray tomosynthesis: a review of its use for breast and chest imaging," *Radiat. Prot. Dosimetry* **139**, 100-107 (2010).
- 2 T. Svahn, D. Chakraborty, D. Ikeda, S. Zackrisson, Y. Do, S. Mattsson, I. Andersson, "Breast tomosynthesis and digital mammography: a comparison of diagnostic accuracy," *Br. J. Radiol.* (2014).
- 3 J.T. Dobbins III and D.J. Godfrey, "Digital x-ray tomosynthesis: current state of the art and clinical potential," *Phys. Med. Biol.* **48**, R65 (2003).
- 4 X. Qian, A. Tucker, E. Gidcumb, J. Shan, G. Yang, X. Calderon-Colon, S. Sultana, J. Lu, O. Zhou, D. Spronk, "High resolution stationary digital breast tomosynthesis using distributed carbon nanotube x-ray source array," *Med. Phys.* **39**, 2090-2099 (2012).
- 5 J. Shan, P. Chtcheprov, A.W. Tucker, Y.Z. Lee, X. Wang, D. Foos, M.D. Heath, J. Lu, O. Zhou, "Stationary chest tomosynthesis using a CNT x-ray source array," presented at SPIE Medical Imaging.
- 6 H. Miao, X. Wu, H. Zhao, H. Liu, "A phantom-based calibration method for digital x-ray tomosynthesis," *J. Xray Sci. Technol.* **20**, 17-29 (2012).
- 7 J.L. Prince and J.M. Links, *Medical Imaging Signals and Systems* (Pearson Prentice Hall Upper Saddle River, NJ, 2006).
- 8 D.M. Gauntt and G.T. Barnes, "An automatic and accurate x-ray tube focal spot/grid alignment system for mobile radiography: System description and alignment accuracy," *Med. Phys.* **37**, 6402-6410 (2010).
- 9 X. Wang and M.K. Rogers, Alignment apparatus for imaging system (2008).
- 10 H. MacMahon, Optical grid alignment system for portable radiography and portable radiography apparatus incorporating same (1993).
- 11 J. Shan, A. Tucker, L. Gaalaas, G. Wu, E. Platin, A. Mol, J. Lu, O. Zhou, "Stationary intraoral digital tomosynthesis using a carbon nanotube X-ray source array," *Dentomaxillofacial Radiology* **44**, 20150098 (2015).
- 12 K. Anton, J.M. Baehring, T. Mayer, "Glioblastoma multiforme: overview of current treatment and future perspectives," *Hematol. Oncol. Clin. North Am.* **26**, 825-853 (2012).
- 13 N.R. Smoll, K. Schaller, O.P. Gautschi, "Long-term survival of patients with glioblastoma multiforme (GBM)," *Journal of Clinical Neuroscience* **20**, 670-675 (2013).
- 14 H.C. Lawson, P. Sampath, E. Bohan, M.C. Park, N. Hussain, A. Olivi, J. Weingart, L. Kleinberg, H. Brem, "Interstitial chemotherapy for malignant gliomas: the Johns Hopkins experience," *J. Neurooncol.* **83**, 61-70 (2007).

- 15 D. Fulton, R. Urtasun, I. Scott-Brown, E. Johnson, B. Mielke, B. Curry, D. Huyser-Wierenga, J. Hanson, M. Feldstein, "Increasing radiation dose intensity using hyperfractionation in patients with malignant glioma," *J. Neurooncol.* **14**, 63-72 (1992).
- 16 R.F. Barajas Jr, J.S. Chang, M.R. Segal, A.T. Parsa, M.W. McDermott, M.S. Berger, S. Cha, "Differentiation of recurrent glioblastoma multiforme from radiation necrosis after external beam radiation therapy with dynamic susceptibility-weighted contrast-enhanced perfusion MR imaging 1," *Radiology* **253**, 486-496 (2009).
- 17 J.P. Sheehan, M.E. Shaffrey, B. Gupta, J. Larnier, J.N. Rich, D.M. Park, "Improving the radiosensitivity of radioresistant and hypoxic glioblastoma," *Future oncology* **6**, 1591-1601 (2010).
- 18 A.M. Spence, M. Muzi, K.R. Swanson, F. O'Sullivan, J.K. Rockhill, J.G. Rajendran, T.C. Adamsen, J.M. Link, P.E. Swanson, K.J. Yagle, R.C. Rostomily, D.L. Silbergeld, K.A. Krohn, "Regional hypoxia in glioblastoma multiforme quantified with [18F]fluoromisonidazole positron emission tomography before radiotherapy: correlation with time to progression and survival," *Clin. Cancer Res.* **14**, 2623-2630 (2008).
- 19 J.A. Hayman, M.K. Martel, R.K. Ten Haken, D.P. Normolle, R.F. Todd 3rd, J.F. Littles, M.A. Sullivan, P.W. Possert, A.T. Turrisi, A.S. Lichter, "Dose escalation in non-small-cell lung cancer using three-dimensional conformal radiation therapy: update of a phase I trial," *J. Clin. Oncol.* **19**, 127-136 (2001).
- 20 D.A. Palma, W.F. Verbakel, K. Otto, S. Senan, "New developments in arc radiation therapy: a review," *Cancer Treat. Rev.* **36**, 393-399 (2010).
- 21 T.R. Mackie, "Advanced image-guided external beam radiotherapy," in *Radiation Oncology Advances*, edited by Anonymous (Springer, 2008), pp. 7-39.
- 22 E.J. Hall, "Intensity-modulated radiation therapy, protons, and the risk of second cancers," *International Journal of Radiation Oncology* Biology* Physics* **65**, 1-7 (2006).
- 23 M. Durante and J.S. Loeffler, "Charged particles in radiation oncology," *Nature reviews Clinical oncology* **7**, 37-43 (2010).
- 24 L.L. Gunderson and J.E. Tepper, *Clinical Radiation Oncology* (Elsevier Health Sciences, 2007).
- 25 I.F. Ciernik, E. Dizendorf, B.G. Baumert, B. Reiner, C. Burger, J.B. Davis, U.M. Lütolf, H.C. Steinert, G.K. Von Schulthess, "Radiation treatment planning with an integrated positron emission and computer tomography (PET/CT): a feasibility study," *International Journal of Radiation Oncology* Biology* Physics* **57**, 853-863 (2003).
- 26 Y. Cheng and O. Zhou, "Electron field emission from carbon nanotubes," *Comptes Rendus Physique* **4**, 1021-1033 (2003).
- 27 J. Zhang, Y. Cheng, Y. Lee, B. Gao, Q. Qiu, W. Lin, D. Lalush, J. Lu, O. Zhou, "A nanotube-based field emission x-ray source for microcomputed tomography," *Rev. Sci. Instrum.* **76**, 094301 (2005).

- 28 P. Schwoebel, J.M. Boone, J. Shao, "Studies of a prototype linear stationary x-ray source for tomosynthesis imaging," *Phys. Med. Biol.* **59**, 2393 (2014).
- 29 X. Calderón-Colón, H. Geng, B. Gao, L. An, G. Cao, O. Zhou, "A carbon nanotube field emission cathode with high current density and long-term stability," *Nanotechnology* **20**, 325707 (2009).
- 30 F. Khan, "Total body irradiation," *The physics of radiation therapy*. 3rd ed. Philadelphia: Lippincott Williams & Wilkins, 455-463 (2003).
- 31 D. Slatkin, P. Spanne, F. Dilmanian, M. Sandborg, "Microbeam radiation therapy," *Med. Phys.* **19**, 1395-1400 (1992).
- 32 D.N. Slatkin, P. Spanne, F.A. Dilmanian, J.O. Gebbers, J.A. Laissue, "Subacute neuropathological effects of microplanar beams of x-rays from a synchrotron wiggler," *Proc. Natl. Acad. Sci. U. S. A.* **92**, 8783-8787 (1995).
- 33 W. Thomlinson, P. Berkvens, G. Berruyer, B. Bertrand, H. Blattmann, E. Brauer-Krisch, T. Brochard, A.M. Charvet, S. Corde, M. Dimichiel, H. Elleaume, F. Esteve, S. Fiedler, J.A. Laissue, J.E. Le Bas, G. Le Duc, N. Lyubimova, C. Nemoz, M. Renier, D.N. Slatkin, P. Spanne, P. Suortti, "Research at the European Synchrotron Radiation Facility medical beamline," *Cell. Mol. Biol. (Noisy-le-grand)* **46**, 1053-1063 (2000).
- 34 J.A. Laissue, N. Lyubimova, H. Wagner, D.W. Archer, D.N. Slatkin, M. Di Michiel, C. Nemoz, M. Renier, E. Brauer, P.O. Spanne, "Microbeam radiation therapy," presented at SPIE's International Symposium on Optical Science, Engineering, and Instrumentation.
- 35 R. Serduc, A. Bouchet, E. Bräuer-Krisch, J.A. Laissue, J. Spiga, S. Sarun, A. Bravin, C. Fonta, L. Renaud, J. Boutonnat, "Synchrotron microbeam radiation therapy for rat brain tumor palliation—influence of the microbeam width at constant valley dose," *Phys. Med. Biol.* **54**, 6711 (2009).
- 36 F.A. Dilmanian, G.M. Morris, N. Zhong, T. Bacarian, J.F. Hainfeld, J. Kalef-Ezra, L.J. Brewington, J. Tammam, E.M. Rosen, "Murine EMT-6 carcinoma: high therapeutic efficacy of microbeam radiation therapy," *Radiat. Res.* **159**, 632-641 (2003).
- 37 M. Miura, H. Blattmann, E. Bräuer-Krisch, A. Bravin, A. Hanson, M. Nawrocky, P. Micca, D. Slatkin, J. Laissue, "Radiosurgical palliation of aggressive murine SCCVII squamous cell carcinomas using synchrotron-generated X-ray microbeams," (2006).
- 38 F.A. Dilmanian, Z. Zhong, T. Bacarian, H. Benveniste, P. Romanelli, R. Wang, J. Welwart, T. Yuasa, E.M. Rosen, D.J. Anschel, "Interlaced x-ray microplanar beams: a radiosurgery approach with clinical potential," *Proc. Natl. Acad. Sci. U. S. A.* **103**, 9709-9714 (2006).
- 39 S. Gil, S. Sarun, A. Biete, Y. Prezado, M. Sabes, "Survival analysis of F98 glioma rat cells following minibeam or broad-beam synchrotron radiation therapy," *Radiat. Oncol.* **6**, 37-717X-6-37 (2011).

- 40 Y. Prezado, S. Sarun, S. Gil, P. Deman, A. Bouchet, G. Le Duc, "Increase of lifespan for glioma-bearing rats by using minibeam radiation therapy," *Journal of synchrotron radiation* **19**, 60-65 (2011).
- 41 A. Bouchet, B. Lemasson, G. Le Duc, C. Maisin, E. Bräuer-Krisch, E.A. Siegbahn, L. Renaud, E. Khalil, C. Rémy, C. Poillot, "Preferential effect of synchrotron microbeam radiation therapy on intracerebral 9L gliosarcoma vascular networks," *International Journal of Radiation Oncology* Biology* Physics* **78**, 1503-1512 (2010).
- 42 F. Dilmanian, Y. Qu, S. Liu, C. Cool, J. Gilbert, J. Hainfeld, C. Kruse, J. Laterra, D. Lenihan, M. Nawrocky, "X-ray microbeams: Tumor therapy and central nervous system research," *Nuclear Instruments and Methods in Physics Research Section A: Accelerators, Spectrometers, Detectors and Associated Equipment* **548**, 30-37 (2005).
- 43 W. Zeman, H. Curtis, C. Baker, "Histopathologic effect of high-energy-particle microbeams on the visual cortex of the mouse brain," *Radiat. Res.* **15**, 496-514 (1961).
- 44 M. Renier, T. Brochard, C. Nemoz, H. Requardt, E. Bräuer, F. Esteve, J. Balosso, P. Suortti, J. Baruchel, H. Elleaume, "The radiotherapy clinical trials projects at the ESRF: Technical aspects," *Eur. J. Radiol.* **68**, S147-S150 (2008).
- 45 Y. Ohno, M. Torikoshi, M. Suzuki, K. Umetani, Y. Imai, K. Uesugi, N. Yagi, "Dose distribution of a 125 keV mean energy microplanar x-ray beam for basic studies on microbeam radiotherapy," *Med. Phys.* **35**, 3252-3258 (2008).
- 46 J. Stepanek, H. Blattmann, J. Laissue, N. Lyubimova, M. Di Michiel, D. Slatkin, "Physics study of microbeam radiation therapy with PSI-version of Monte Carlo code GEANT as a new computational tool," *Med. Phys.* **27**, 1664-1675 (2000).
- 47 F. Khan, "Interactions of ionizing radiation," *The Physics of radiation therapy*. Philadelphia: Lippincott Williams & Wilkins, 59-61 (2003).
- 48 J. Zhang, G. Yang, Y. Cheng, B. Gao, Q. Qiu, Y. Lee, J. Lu, O. Zhou, "Stationary scanning x-ray source based on carbon nanotube field emitters," *Appl. Phys. Lett.* **86**, 184104 (2005).
- 49 M. Hadsell, J. Zhang, P. Laganis, F. Sprenger, J. Shan, L. Zhang, L. Burk, H. Yuan, S. Chang, J. Lu, "A first generation compact microbeam radiation therapy system based on carbon nanotube X-ray technology," *Appl. Phys. Lett.* **103**, 183505 (2013).
- 50 O.Z. Zhou and S.X. Chang, Compact microbeam radiation therapy systems and methods for cancer treatment and research **U.S. Patent No. 8,600,003**. (3 Dec. 2013.).
- 51 P. Chtcheprov, C. Inscoe, L. Zhang, J. Lu, O. Zhou, S. Chang, F. Sprenger, P. Laganis, "A High Power Nanotube X-Ray Microbeam Irradiator for Preclinical Brain Tumor Treatment," *Med. Phys.* **41**, 517-517 (2014).
- 52 L. Zhang, H. Yuan, L.M. Burk, C.R. Inscoe, M.J. Hadsell, P. Chtcheprov, Y.Z. Lee, J. Lu, S. Chang, O. Zhou, "Image-guided microbeam irradiation to brain tumour bearing mice using a carbon nanotube x-ray source array," *Phys. Med. Biol.* **59**, 1283 (2014).

- 53 Y.Z. Lee, L. Burk, K. Wang, G. Cao, J. Lu, O. Zhou, "Carbon nanotube based X-ray sources: Applications in pre-clinical and medical imaging," Nuclear Instruments and Methods in Physics Research Section A: Accelerators, Spectrometers, Detectors and Associated Equipment **648**, S281-S283 (2011).
- 54 G. Cao, Y. Lee, R. Peng, Z. Liu, R. Rajaram, X. Calderon-Colon, L. An, P. Wang, T. Phan, S. Sultana, "A dynamic micro-CT scanner based on a carbon nanotube field emission x-ray source," Phys. Med. Biol. **54**, 2323 (2009).
- 55 G. Cao, L.M. Burk, Y.Z. Lee, X. Calderon-Colon, S. Sultana, J. Lu, O. Zhou, "Prospective-gated cardiac micro-CT imaging of free-breathing mice using carbon nanotube field emission x-ray," Med. Phys. **37**, 5306-5312 (2010).
- 56 P. Chtcheprov, L. Burk, H. Yuan, C. Inscoe, R. Ger, M. Hadsell, J. Lu, L. Zhang, S. Chang, O. Zhou, "Physiologically gated microbeam radiation using a field emission x-ray source array," Med. Phys. **41**, 081705 (2014).
- 57 L. Zhang, H. Yuan, L.M. Burk, C.R. Inscoe, M.J. Hadsell, P. Chtcheprov, Y.Z. Lee, J. Lu, S. Chang, O. Zhou, "Image-guided microbeam irradiation to brain tumour bearing mice using a carbon nanotube x-ray source array," Phys. Med. Biol. **59**, 1283 (2014).
- 58 J. Adam, M. Biston, A. Joubert, A. Charvet, J. Le Bas, F. Estève, H. Elleaume, "Enhanced delivery of iodine for synchrotron stereotactic radiotherapy by means of intracarotid injection and blood-brain barrier disruption: Quantitative iodine biodistribution studies and associated dosimetry," International Journal of Radiation Oncology* Biology* Physics **61**, 1173-1182 (2005).
- 59 X. Zhong, C.H. Meyer, D.J. Schlesinger, J.P. Sheehan, F.H. Epstein, J.M. Larner, S.H. Benedict, P.W. Read, K. Sheng, J. Cai, "Tracking brain motion during the cardiac cycle using spiral cine-DENSE MRI," Med. Phys. **36**, 3413-3419 (2009).
- 60 Y.Z. Lee, L.M. Burk, K. Wang, G. Cao, J. Volmer, J. Lu, O. Zhou, "Prospective respiratory gated carbon nanotube micro computed tomography," Acad. Radiol. **18**, 588-593 (2011).
- 61 Y. Yang, S. Rendig, S. Siegel, D.F. Newport, S.R. Cherry, "Cardiac PET imaging in mice with simultaneous cardiac and respiratory gating," Phys. Med. Biol. **50**, 2979 (2005).
- 62 L.J. Kuo and L.X. Yang, "Gamma-H2AX - a novel biomarker for DNA double-strand breaks," In Vivo **22**, 305-309 (2008).